NASA Contractor Report 159093

ORIGINAL PAGE IS
OF POOR QUALITY

HIGH LIFT
SELECTED CONCEPTS

(NASA-CR-159093) HIGH LIFT SELECTED CONCEPTS Final Report, Aug. 1977 - Jul. 1978 (Boeing Commercial Airplane Co., Seattle) 108 p HC A06/MF A01 CSCL 01A
N82-15017
Unclas
G3/02 08740

ENERGY EFFICIENT
TRANSPORT PROGRAM

BOEING COMMERCIAL AIRPLANE COMPANY
P.O. BOX 3707, SEATTLE, WA 98124

CONTRACT NAS1-14742, TASK 4.3
AUGUST 1979

JAN 1982
RECEIVED
NASA STI FACILITY
ACCESS DEPT.

NASA
National Aeronautics and
Space Administration

Langley Research Center
Hampton, Virginia 23665

ORIGINAL PAGE IS
OF POOR QUALITY

FOREWORD

This document constitutes the final report for Task 4.3, High Lift Selected Concepts, one of the five major tasks described by the statement of work for contract NAS1-14742, Selected Advanced Aerodynamic and Active Control Concepts Development.

Task 4.3 encompasses three significant areas of investigation:

1. A preliminary study of high-lift system impact on energy efficient transport (EET) sizing
2. An exploration of high-lift technology gains available by designing to full-scale Reynolds numbers using the latest computational techniques
3. Evaluation of the impact of the best design on EET sizing and economics

This report discusses the work conducted from August 1977 through July 1978. The NASA technical monitor for all contract tasks was Mr. D. B. Middleton of the Energy Efficient Transport Project Office of the Langley Research Center.

The high-lift system design study and the engineering coordination for the task were conducted within the Aerodynamics Research Unit of the Boeing Commercial Airplane Company. The high-lift system impact study was conducted within the Preliminary Design department of the Vice President—Engineering organization of the Boeing Commercial Airplane Company.

Boeing personnel who participated and their areas of contribution are:

G. W. Hanks	Program manager
J. L. Lundry	Task manager, high-lift selected concepts
M. L. Henderson	Principal investigator
Roger Anderson	Aeroperformance
D. N. Ball	Airfoil design
Brindu Giridharadas	Weights
Wayne Holmquist	Low-speed aerodynamics
John Paulson	Low-speed aerodynamics
R. L. Sullivan	Aeroperformance
Max Taylor	Stability and control
John Vachal	Supervisor, preliminary design, aero

Although a large number of people contributed to the work of this task, Mr. Henderson and Mr. Sullivan were primarily responsible for writing the design applications and requirements definition elements, respectively, of this document. Mr. Henderson, as principal investigator, was responsible for final integration.

Principal measurements and calculations used during this study were in customary units.

CONTENTS

Page

1.0 SUMMARY 1

2.0 INTRODUCTION 9
  2.1 Design Application Studies 9
  2.2 Requirements Definition Studies 10
  2.3 Impact Study 11

3.0 SYMBOLS AND ABBREVIATIONS 13

4.0 STUDY RESULTS 17
  4.1 Design Application Studies 17
    4.1.1 Analysis of Baseline $C_{l_{max}}$ at Wind Tunnel Reynolds Number 17
    4.1.2 Analysis of Baseline Section at Flight Reynolds Number 23
    4.1.3 Design at Flight Reynolds Number for Best $C_{l_{max}}$ 25
    4.1.4 Design at Flight Reynolds Number for Simplification 40
  4.2 Requirements Definition Studies 49
    4.2.1 Baseline Sizing and Study Ground Rules 49
    4.2.2 Planform Trade Studies 52
    4.2.3 Flap Technology Trade Studies 60
    4.2.4 Climb and Descent Studies 63
    4.2.5 Augmented Stability Studies 67
  4.3 Impact of Best Selection 70

5.0 CONCLUSIONS AND RECOMMENDATIONS 75

6.0 REFERENCES 77

APPENDIX A: Description of the Baseline High-Lift System Geometry 79

APPENDIX B: Calculation of Lift and Pitching Moment When Separation Is Present 85

APPENDIX C: Inverse Boundary Layer Technique for Pressure Distribution Synthesis and Optimization, Program A427 89

APPENDIX D: Definition of Airfoil Geometry 97

EDING PAGE BLANK NOT FILMED

FIGURES

		Page
1.	Lift and Pitching Moment Characteristics of Baseline Four-Element Airfoil	2
2.	Theoretical Lift Curves of the $C_{l_{max}}$ Design and the Baseline Airfoil at Flight Reynolds Numbers	3
3.	Comparison of High-Lift System Geometry	3
4.	Lift Curves for NASA/EET Simplified Design	4
5.	Simplified and Baseline High-Lift System Geometries	5
6.	Baseline Airplane (Model 768-785B)	6
7.	Design Selection Chart for Reference Airplane, 768-785B	7
8.	Lift and Pitching Moment Characteristics of Baseline Four-Element Airfoil	18
9.	Comparison of Theoretical and Experimental Pressures on Baseline Airfoil--Angle of Attack = 4.4 deg	19
10.	Comparison of Theoretical and Experimental Pressure on Baseline Airfoil--Angle of Attack = 16.6 deg	20
11.	Potential Flow Pressure Distribution of Baseline Airfoil--Angle of Attack = 21.7 deg (A465 Analysis)	21
12.	Theoretical Pressure Distribution on Baseline Airfoil: Separation Modeled on Aft Flap Only--Angle of Attack = 21.7 deg (A465 Analysis)	22
13.	Theoretical Pressure Distribution on Baseline Airfoil: Separation Modeled on Aft and Main Flaps Only--Angle of Attack = 21.7 deg	23
14.	Theoretical Pressure Distribution on Baseline Airfoil: Separation Modeled on Main Airfoil and Main and Aft Flaps--Angle of Attack = 21.7 deg (A465 Analysis)	24
15.	Comparison of Theoretical and Experimental Pressures on Baseline Airfoil--Angle of Attack = 21.7 deg	25
16.	Theoretical Lift Curves of Baseline Airfoil at Wind Tunnel and Flight Reynolds Numbers	26
17.	Variation of $C_{l_{max}}$ With Reynolds Number	27
18.	Theoretical Pressure Distribution on the Baseline Airfoil at Flight Reynolds Number--Angle of Attack = 18.6 deg	28

-EDING PAGE BLANK NOT FILMED

Page

19. Theoretical Pressure Distribution on the Baseline Airfoil at Flight Reynolds Number--Angle of Attack = 21.7 deg 29

20. Theoretical Pressure Distribution on the Baseline Airfoil at Flight Reynolds Number--Angle of Attack = 24 deg 30

21. Theoretical Lift Curves of the $C_{l_{max}}$ Design and the Baseline Airfoil at Flight Reynolds Number 31

22. Comparison of High-Lift System Geometry 32

23. Comparison of Baseline and Redesigned Pressure Distributions and Geometry--Leading Edge Flap 33

24. Comparison of Baseline and Redesigned Pressure Distributions and Geometry--Main Wing 34

25. Comparison of Baseline and Redesigned Pressure Distributions and Geometry--Main Flap 35

26. Comparison of Baseline and Redesigned Pressure Distribution and Geometry--Aft Flap 36

27. Multielement Airfoil System Design Process 37

28. Design of an Airfoil Element 38

29. Simplified and Baseline High-Lift System Geometries 40

30. Lift Curves for NASA/EET Simplified Design 42

31. Simplified Trailing Edge Flap Pressure Distribution--Angle of Attack = 12 deg 44

32. Separated Flow Theory Analysis of the Simplified Design--Angle of Attack = 12 deg 45

33. Separated Flow Theory Analysis of the Simplified Design--Angle of Attack = 18 deg 46

34. Separated Flow Theory Analysis of the Simplified Design--Angle of Attack = 20 deg 47

35. Separated Flow Theory Analysis of the Simplified Design--Angle of Attack = 22 deg 48

36. Design Selection Chart for Reference Airplane, 768-785B 52

37. Baseline Airplane (Model 768-785B) 53

38. Cruise Mach/Wing Planform Trades 54

Page

39. Fuel/OEW Trade (Conventional Aluminum Structure) 55

40. Normalized Wing Weight Versus Aspect Ratio (Conventional Aluminum Structure) 56

41. Economic Comparison With DOC at 1852 km (1000 nmi) 57

42. Effect of Trailing Edge Flap Chord 58

43. Effect of Leading Edge Flap Chord 59

44. Effects of Varying Flap Chord on Low-Speed Sizing Constraints (Model 768-785) 61

45. Trailing Edge Flap Chord Trade (0.22c Versus 0.17c) 62

46. Baseline and Assumed Advanced Flap Envelopes 64

47. EET Baseline Design Selection Chart 65

48. Common Climb and Descent Speed Schedule 66

49. Enroute Drag 67

50. Effect of Trim CG Location 68

51. Effects of Aft CG Position on Low-Speed Sizing Constraints 69

52. "Simplified" Flap Envelope 71

53. Impact of "Simplified" Design on EET Sizing 72

54. EET High-Lift Technology Takeoff Performance Benefits 73

A1. Location of the Baseline Airfoil on the Wing Planform 80

A2. Leading- and Trailing-Edge Flaps 81

A3. Definition of Baseline Main Airfoil Element 82

A4. Definition of Main and Aft Flap Elements 83

A5. Definition of Baseline Leading Edge Flap 84

C1. Airfoil Design Process 90

C2. The Rooftop Pressure Distribution Architecture 92

C3. Four-Region Pressure Distribution Architecture 93

C4. Block Diagram of Interactive Pressure-Distribution Optimizer 94

TABLES

Page

1. Comparison of Configurations 1 through 5 43

2. Sized EET Airplane Performance and Characteristics (Model 768-785B) 51

3. Flap Chord Sizes 57

4. EET Twin Advanced Flap Study Size and Performance Comparison 66

D1. $C_{l_{max}}$ Design Ordinates 98

D2. Simplified Design Ordinates 99

EDING PAGE BLANK NOT FILMED

1.0 SUMMARY

The three engineering investigations covered by this report and their broad objectives are:

a. Design application studies: Determine the benefits to high-lift system maximum lift and, alternatively, to high-lift system complexity, of applying newly developed analytic design and analysis techniques to the design of high-lift sections for flight conditions. In this investigation, two new high-lift sections were designed to flight conditions.

b. Requirements definition studies: Clarify the influence of the high-lift system on the sizing and economics of a specific energy efficient transport (EET), using a computerized sizing technique and an existing advanced airplane design data base.

c. Impact study: Evaluate the impact of the best design resulting from the design application studies on EET sizing and economics.

The key results from each investigation are summarized below.

Design Application Studies

a. To gage the quality of the analytic design work, the theoretical lift curve of a representative high-lift system, predicted by a Boeing computer program using separated flow theory (ref. 1), was compared with existing wind tunnel data. In this comparison, Cl_{max} was predicted within 2%, and the angle of attack for Cl_{max} and C_l at low angles of attack were predicted correctly. Figure 1 displays these results. These analyses represented one of the most important products of the work since they represented a breakthrough in analytic capability. While the development of these programs was funded by Boeing IR&D money, the validation of their use in analyzing a representative transport high-lift section that was performed under this contract was invaluable in increasing confidence in the methods and will accelerate the application to both in-house problems and future contract work.

b. A four-element high-lift airfoil was redesigned at flight Reynolds number (17×10^6), using advanced analytical techniques. The redesign produced a 13% improvement in Cl_{max} when compared with the high Reynolds number analysis of a similar airfoil defined using conventional techniques for low Reynolds number (2×10^6). The theoretical lift curve of the redesigned airfoil is compared to the lift curve of the conventionally designed (baseline) airfoil in figure 2. The geometries of the two sections are compared in figure 3.

c. A three-element, simplified airfoil was designed at flight Reynolds number to produce the same Cl_{max} as the conventional four-element section. The theoretical lift curves and geometries of these two sections are compared in figures 4 and 5, respectively.

d. An important byproduct of these design tasks was the validation of a rational design method for the synthesis of multielement high-lift airfoils. Using analytic techniques, this methodology allows optimization of pressure distributions and airfoil shapes within the aerodynamic and structural restraints and greatly reduces trial and error in the design process. This methodology represents a significant improvement in high-lift system design techniques.

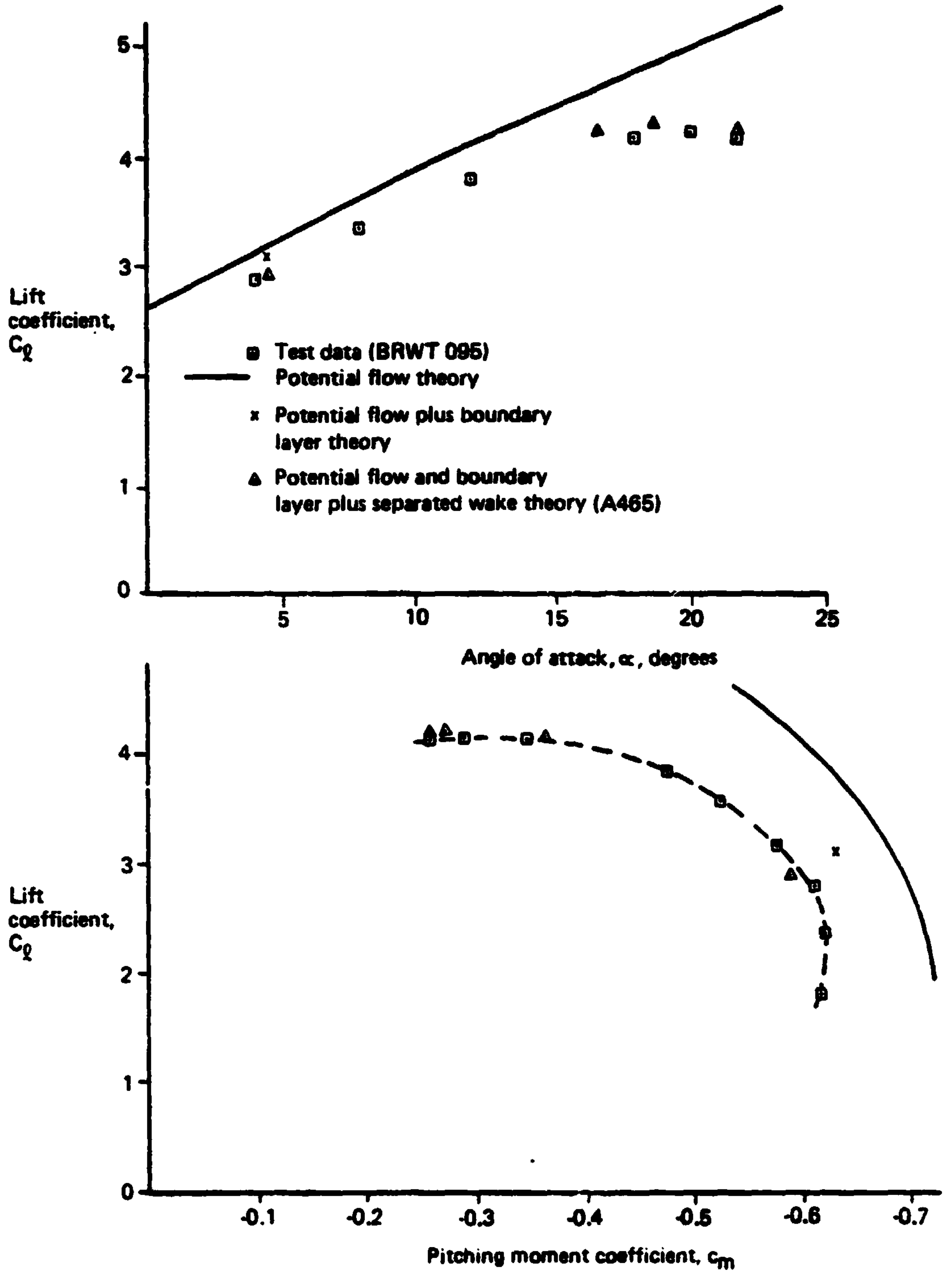

Figure 1. Lift and Pitching Moment Characteristics of Baseline Four-Element Airfoil

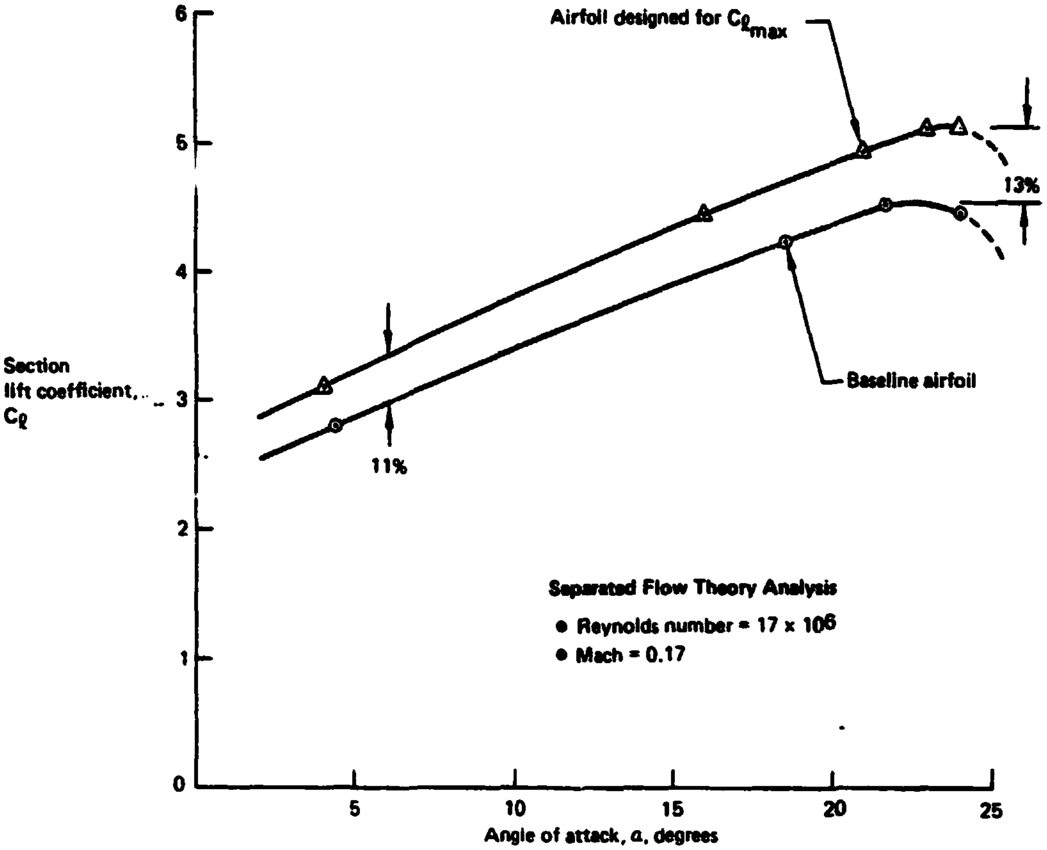

Figure 2. Theoretical Lift Curves of the $C_{\ell_{max}}$ Design and the Baseline Airfoil at Flight Reynolds Numbers

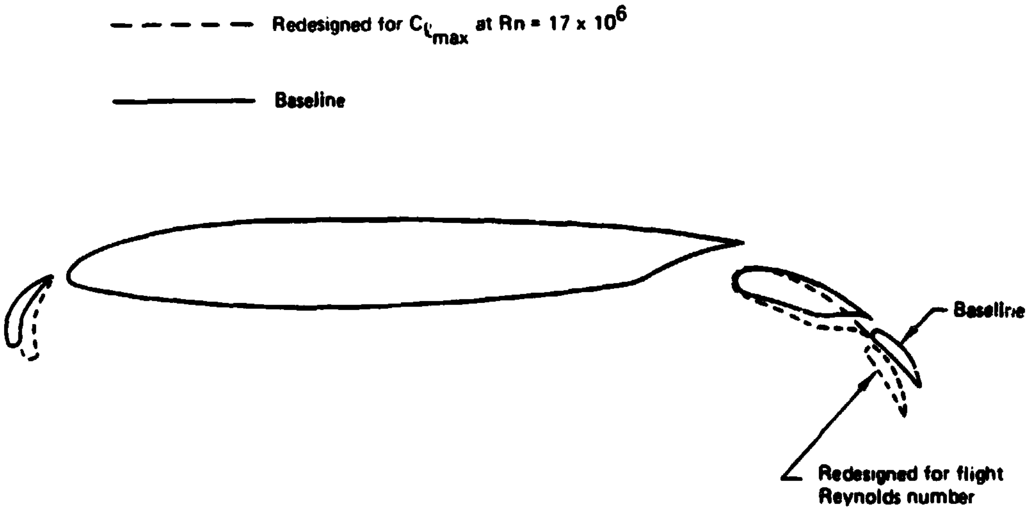

Redesigned for $C_{\ell_{max}}$ at Rn = 17 x 10^6
Baseline
Baseline
Redesigned for flight Reynolds number

Figure 3. Comparison of High Lift System Geometry

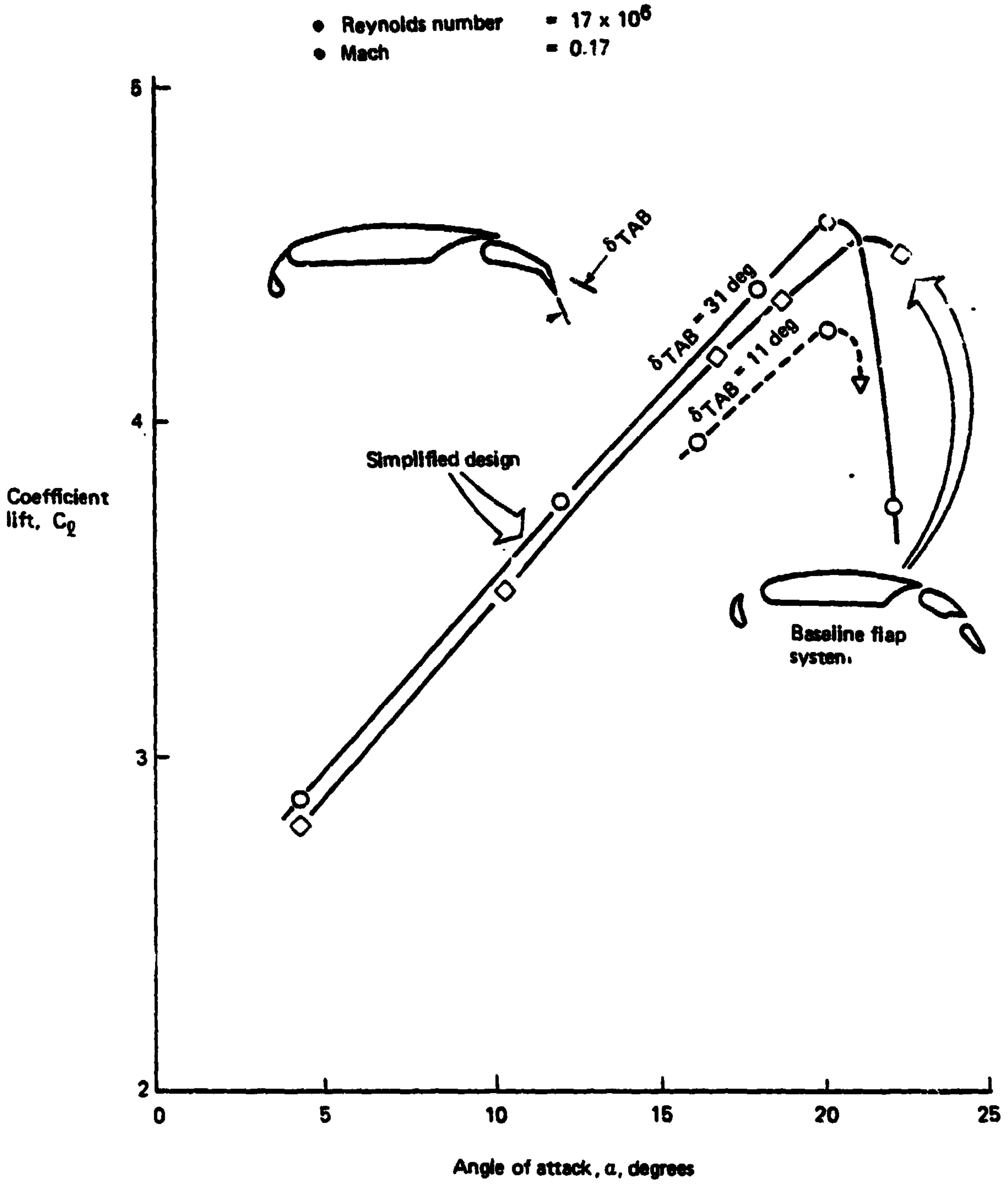

Figure 4. Lift Curves NASA/EET Simplified Design

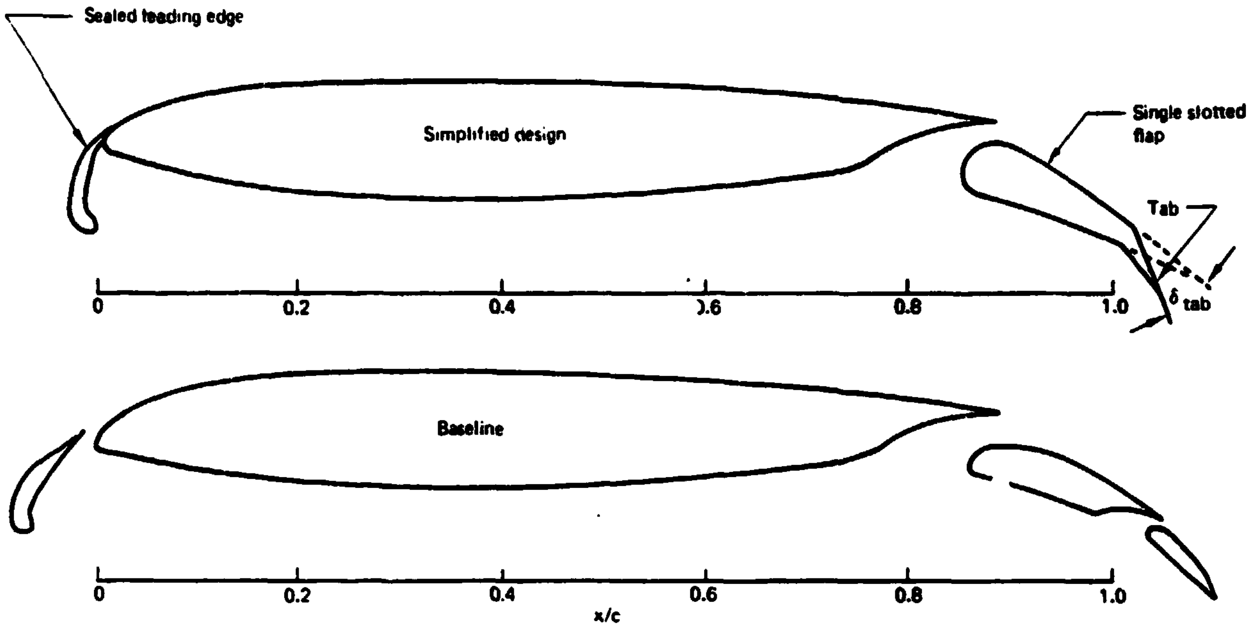

Figure 5. Simplified and Baseline High-Lift System Geometries

Requirement Definition Studies

a. An advanced-technology, twin-engine transport configuration was selected as the baseline for all the sizing trade studies. This configuration is illustrated in figure 6.

b. In fixed-mission sizing studies, the baseline airplane was found to be insensitive to landing $C_{l_{max}}$ improvements due to the low wing loading required to satis[illegible] level takeoff and enroute engine-out altitude requirements, while minimizing [illegible] fuel, TOGW, and DOC.

c. The baseline airplane performance was found to be most sensitive to improvements in takeoff lift-to-drag ratio (L/D), particularly at the low lift coefficient levels typical of takeoff out of high, hot airfields (e.g., Denver).

d. Selection of an airplane design for minimum energy consumption conflicts with selection for minimum takeoff gross weight, for the 196-passenger, 3704-km (2,000-nmi) mission requirements assumed in the trade studies. The trade studies showed the following:

   1. Disregarding restraints imposed by takeoff, landing, and engine-out altitude, selection of an airplane designed for minimum energy consumption produced an 8.5% increase in takeoff gross weight relative to the minimum gross weight design (fig. 7).

   2. Similarly, selection of an airplane design for minimum takeoff gross weight produced a 7% increase in energy consumption for the design mission relative to the minimum energy design (fig. 7).

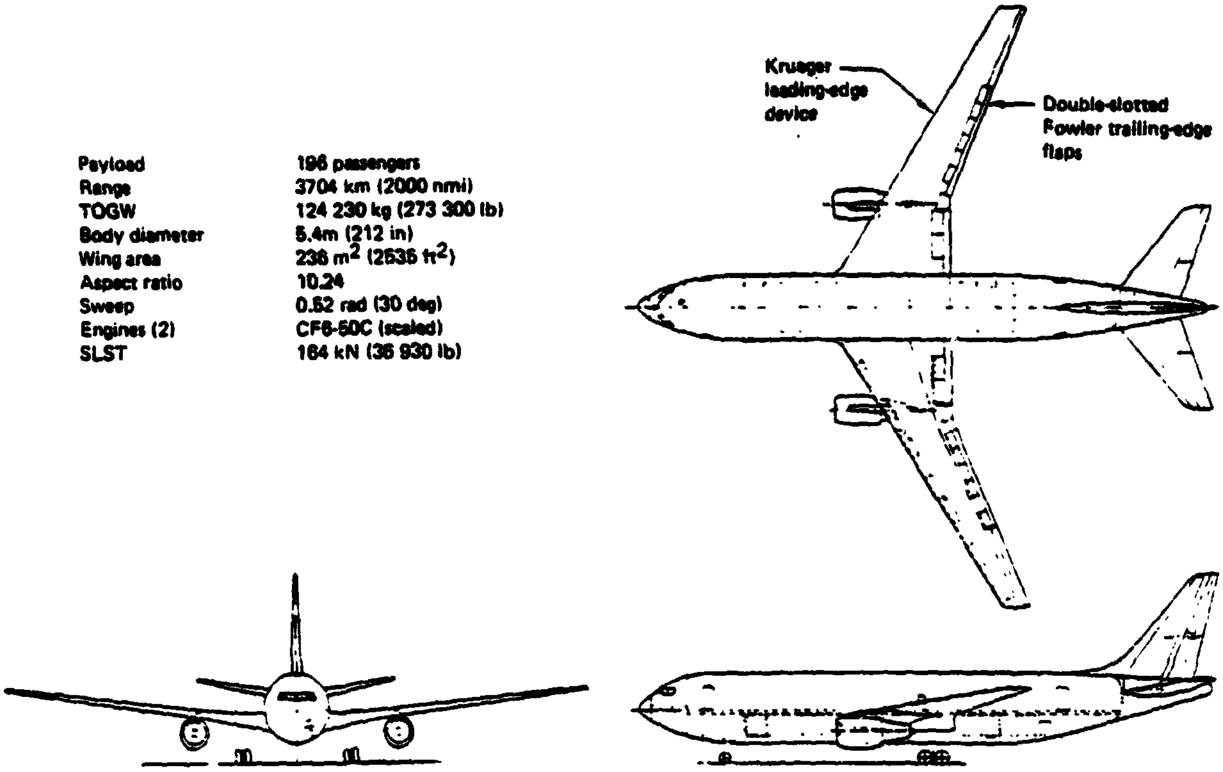
Krueger leading-edge device
Double-slotted Fowler trailing-edge flaps

Payload	196 passengers
Range	3704 km (2000 nmi)
TOGW	124 230 kg (273 300 lb)
Body diameter	5.4m (212 in)
Wing area	236 m^2 (2535 ft^2)
Aspect ratio	10.24
Sweep	0.52 rad (30 deg)
Engines (2)	CF6-50C (scaled)
SLST	164 kN (36 930 lb)

Figure 6. Baseline Airplane, Model 768-785B

3. The baseline airplane, which was selected to have minimum takeoff weight and to just satisfy the 2290-m (7,500-ft) sea-level takeoff requirements, has a 0.5% increase in energy consumption and a 3.5% increase in takeoff weight relative to the two design mimima (fig. 7).

Impact Study

a. The "simplified" high-lift section produced in the design application studies most closely matched the requirements of the baseline configuration since, in this design effort, Cl_{max} was not increased and the improved design techniques were directed toward simplifying the section and increasing L/D. Applying this device to the baseline configuration resulted in a 13% (26-passenger) increase in payload out of Denver relative to the baseline configuration. The improvement in L/D (5.6% at sea-level takeoff lift levels) achieved by this device did not result in wing resizing or a reduction in airplane size, because the engine-out altitude requirement of 3660m (12,000 ft) would be violated at the higher wing loadings.

b. If the wing were sized for minimum direct operating cost (DOC) for the high-altitude, hot-day mission, then use of the "simplified" flap would result in a 0.6% reduction in DOC relative to the resized baseline.

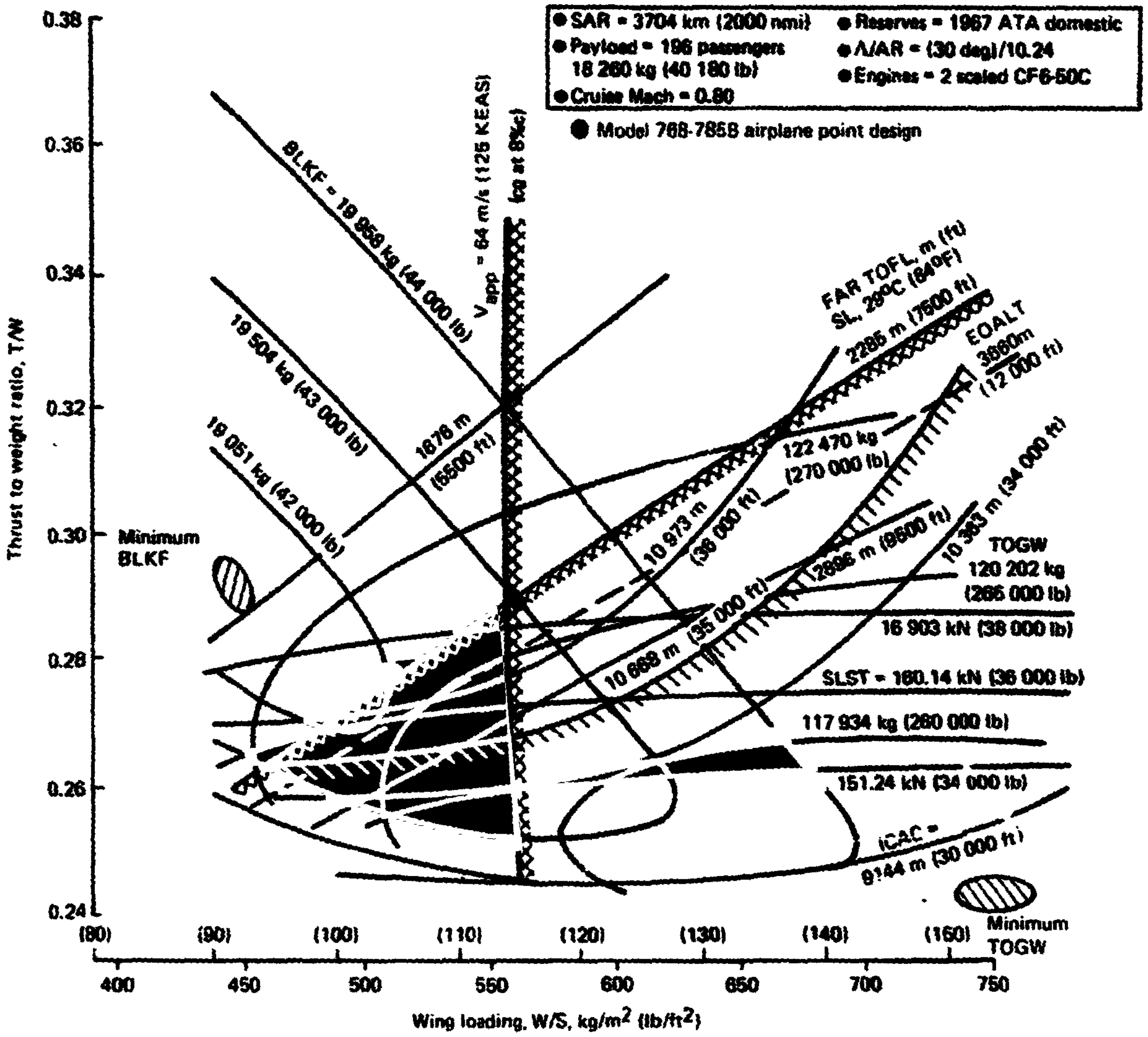

Figure 7. Design Selection Chart for Reference Airplane, 768-785B

Recommendations

Because the requirement studies and the design studies were done concurrently, rather than sequentially, the high-lift sections designed under this contract did not address specifically the performance requirements of the baseline configuration. Follow-on contract work should concentrate on the design of a high-lift section that would improve L/D performance at low-lift levels typical of the Denver takeoff.

It is recommended that a section designed for takeoff L/D and a section designed during this study for improved $C_{l_{max}}$ be tested at the NASA-Langley Research Center Low-Turbulence Pressure Tunnel.

2.0 INTRODUCTION

The high-lift system is an important factor in the design of a new airplane. Typically, the wing for a new design is sized to satisfy cruise considerations (initial cruise altitude, buffet margin, etc.) and low-speed, high-lift considerations such as approach speed and takeoff field length. The impact of high-lift design is fairly well established for conventional transport configurations; however, the effects on the airplane as it evolves toward a high-aspect-ratio energy-efficient configuration are only now beginning to be addressed. The future emphasis on fuel efficiency will produce trends toward higher aspect ratios and different wing loading and thrust loading matches, forcing different compromises in high-lift device design and size than are typical of conventionally sized transports.

To address the total high-lift design problem, the work was divided into three studies: (1) a design application study, to determine what improvements in high-lift system technology might be available using improved design and analysis techniques; (2) a requirements study, to determine the role a high-lift system will play in the sizing of an energy efficient transport (EET); and (3) an impact study, to assess the impact of any improved technology uncovered in the design study.

Because of schedule constraints, the requirements definition study and high-lift system design application studies were performed concurrently.

This scheduling effectively decoupled the results of the two studies so that the design work could not directly address the high-lift requirements exposed in the requirements definition study. Consequently, the two studies are treated separately in this document.

In the future, the high-lift airplane design problem should be approached first by assessing how the high-lift system, in terms of device type, size, and technology, affects the airplane sizing and fuel efficiency and then by exploring areas of advanced high-lift system design technology that would have high leverage in improving the airplane configuration. This type of two-phase study would produce maximum benefit from advanced high-lift technology design work by focusing the design work on performance areas crucial to the airplane sizing.

2.1 DESIGN APPLICATION STUDIES

The purpose of this subtask was to investigate high-lift technology gains in terms of Cl_{max} available or, alternatively, the flap simplifications possible when a high-lift system was designed to full-scale operating Reynolds numbers.

Recent Boeing development of computerized analytical techniques (refs. 1 and 2) has made possible the analysis and design of airfoil sections over a wide range of Reynolds numbers. These computer programs account for the effects on section forces of both attached boundary layer and boundary layer separations that may occur on any or all elements in a multielement airfoil section. In the design mode, the programs may be used first to design a pressure distribution to specific boundary layer parameters and then to design an airfoil contour to produce the desired pressure distribution.

PRECEDING PAGE BLANK NOT FILMED

Contractor-developed computational tools were used in this subtask to design and analyze two-dimensional flap systems for predicting and improving the high-lift technology available for an energy-efficient transport.

The first endeavor of the design subtask was to establish the effectiveness of computational techniques in predicting lift performance of a representative high-lift system. This was accomplished by analyzing a four-element high-lift system for which high-quality two-dimensional Boeing wind tunnel data were available for comparison.

This four-element high-lift system was adopted as the baseline configuration for the remaining design subtask because of the excellent wind tunnel data base and because it was representative of conventionally defined high-lift systems. However, the cruise section used in this baseline high-lift system is known to be inferior in cruise performance to modern sections presently in use by the Contractor and other investigators. This cruise section does not represent the transonic technology level of the wings in the Requirements Definition study.

Subsequent analysis of the baseline high-lift system was performed at full-scale Reynolds number (17 x 10^6). This analysis was to be used as the performance basis for the design tasks to follow.

In the first design exercise, the computational techniques validated in the previous subtask were used to design an alternative flap system for improved $C_{l_{max}}$ at full-scale Reynolds number. The geometric constraints imposed on the baseline flap system were also applied to the new design. The objective of this design was to demonstrate the technology gains available, in terms of $C_{l_{max}}$, by designing to full-scale Reynolds number.

In the second design task, the computational techniques were applied to the design of a simplified high-lift section at full-scale Reynolds number. The objective of this endeavor was to provide the simplest flap design that would produce the same $C_{l_{max}}$ as the baseline flap system (at full-scale Reynolds number) and improved lift-to-drag ratio.

2.2 REQUIREMENTS DEFINITION STUDIES

The approach taken in this subtask was to: (1) select a baseline configuration (referred to as model 768-785B); (2) select fixed-mission sizing criteria in terms of payload, range, cruise speed, initial cruise altitude, cruise lift coefficient, takeoff field length, and approach speed; and (3) perform selected airplane sizing studies. These studies were undertaken to evaluate the effects of flap system area, flap type, and flap technology on the baseline configuration.

In addition to the flap size and technology studies, other investigations were performed to determine the effects of wing aspect ratio and augmented stability on airplane sizing and high-lift system requirements and to determine if the high-lift system might be employed to reduce fuel burned during climb and descent.

The primary tool for evaluation of the effects of planform and flap technology was the Boeing Thumbprint program. This program is a general airplane sizing method that integrates aerodynamic, propulsion, and weight information to produce sizing charts, which allow the choice of wing and thrust loading to be made while best fulfilling the established design criteria.

2.3 IMPACT STUDY

This section presents the impact on the baseline EET sizing and economics of: (1) the two high-lift systems defined in the design subtask, (2) modified climb and descent schedules, and (3) augmented stability (as it influences landing and takeoff only). The same techniques were used in this study as in the requirements studies.

3.0 SYMBOLS AND ABBREVIATIONS

AR	Aspect ratio
BLKF	Block fuel
CG	Center of gravity
$\bar{c}$	Mean aerodynamic chord
C/4	Quarter chord
C_d	Section drag coefficient
C_D	Airplane drag coefficient
C_{DMIN}	Minimum airplane drag coefficient
c_f/c	Flap chord to wing chord ratio
c_{flap}	Flap chord
C_l	Section lift coefficient
C_{lmax}	Maximum section lift coefficient
C_L	Airplane lift coefficient
C_{LAPP}	Approach lift coefficient
C_{LR}	Lift coefficient at rotation
C_{Ltrim}	Trimmed lift coefficient
C_{LV2}	Second segment climb lift coefficient
C_{LE}/C	Leading-edge flap chord to wing chord ratio
C_M	Section pitching moment coefficient
C_p	Pressure coefficient
c_{ref}	Reference chord
C_{wing}	Wing chord
DOC	Direct operating cost
EOALT	Engine out altitude

PRECEDING PAGE BLANK NOT FILMED

FAR	Federal Air Regulations
G	Gap
H	Boundary layer form parameter (δ^*/θ)
ICAC	Initial cruise altitude capability
MAC	Mean aerodynamic chord
OEW	Operating empty weight
P/L	Payload
R	Reynolds number based on momentum thickness ($\rho V\theta/\mu$)
SAR	Still air range
s/c	Surface arc length normalized by section chord
SL	Sea level
SLST	Sea level static thrust
t/c	Normalized thickness
TOFL	Takeoff field length
TOGW	Takeoff gross weight
T/W	Thrust loading; i.e., thrust/weight
u/u_∞	Ratio of local velocity (at edge of boundary layer) to freestream velocity
VCK	Variable camber Krueger
V_S	Stall speed
WDP	Wing design plane
W/S	Wing loading; i.e., weight/wing area
V_{APP}	Approach speed
X/C, Y/C	Normalized airfoil coordinates
θ/C	Normalized boundary layer momentum thickness
δ^*/c	Normalized boundary layer displacement thickness
τ_0	Surface shear stress

ρ	Density of air
Λ	Wing sweep
ΔFB	Change in fuel burn
ΔX	Overlap
$\alpha_{V_{MU}}$	Angle of attack at minimum unstick speed

PRECEDING PAGE BLANK NOT FILMED

4.0 STUDY RESULTS

4.1 DESIGN APPLICATION STUDIES

The results of four investigations are presented in this section. They are:

4.1.1 Analysis of the baseline high-lift system at wind tunnel Reynolds number
4.1.2 Analysis of the baseline high-lift system at flight Reynolds number
4.1.3 Design to increase $C_{l_{max}}$
4.1.4 Design to simplify system

4.1.1 Analysis of Baseline Section $C_{l_{max}}$ at Wind Tunnel Reynolds Number

A representative high-lift system was analyzed for lift curve slope and for $C_{l_{max}}$, using the computational techniques of reference 1, and the results were compared with wind tunnel data. This task was motivated by the fact that prediction of $C_{l_{max}}$ is crucial to high-lift system design, and the use of analytical computational tools to predict the effects of large separations on the lift curve, through $C_{l_{max}}$, of the multielement airfoil sections was, at the time, unprecedented.

The purpose of the analysis was to provide a validation of the analytical techniques with which to gage the accuracy of the remaining analyses and designs in this study.

The choice of a baseline high-lift system was based on the existence of the Contractor's extensive experimental data base resulting from a two-dimensional test of a representative high-technology, high-lift section. This section was chosen as the basis for calibration and, as discussed in later sections, as the baseline for advanced high-lift designs. The cruise characteristics of the section are not representative of current transonic airfoil technology and the airfoil was not used in the Requirements Definition studies of Section 4.2. Nevertheless, this airfoil includes the general transonic characteristics that are important when its high-lift system is defined. A complete description of the baseline high-lift system is given in the figures of appendix A.

Results

Theoretical airfoil section characteristics are compared with test data in figure 8. Sectional lift and pitching moment properties are well predicted even when separations exist on all elements of the high-lift system. Maximum lift coefficient is predicted within 2% of the test data, and the angle of attack for stall is predicted correctly.

The aft flap is partially separated at all angles of attack. Even at 4-deg angle of attack, lift loss predicted by modeling the boundary layer without accounting for separation (method of ref. 3) is only a third of the total lift difference between the potential flow analysis and the wind tunnel data. Modeling of the separation accounts for the remainder of the difference, as shown in figures 8 and 9.

The computed and experimental pressure distributions (figs. 9, 10, and 11) also indicate excellent agreement, and suggest that the Contractor's technique of modeling separations may be applied with confidence to multielement high-lift sections. These results were considered unique at the time they were generated and were presented in reference 1.

'NG PAGE BLANK NOT FILMED

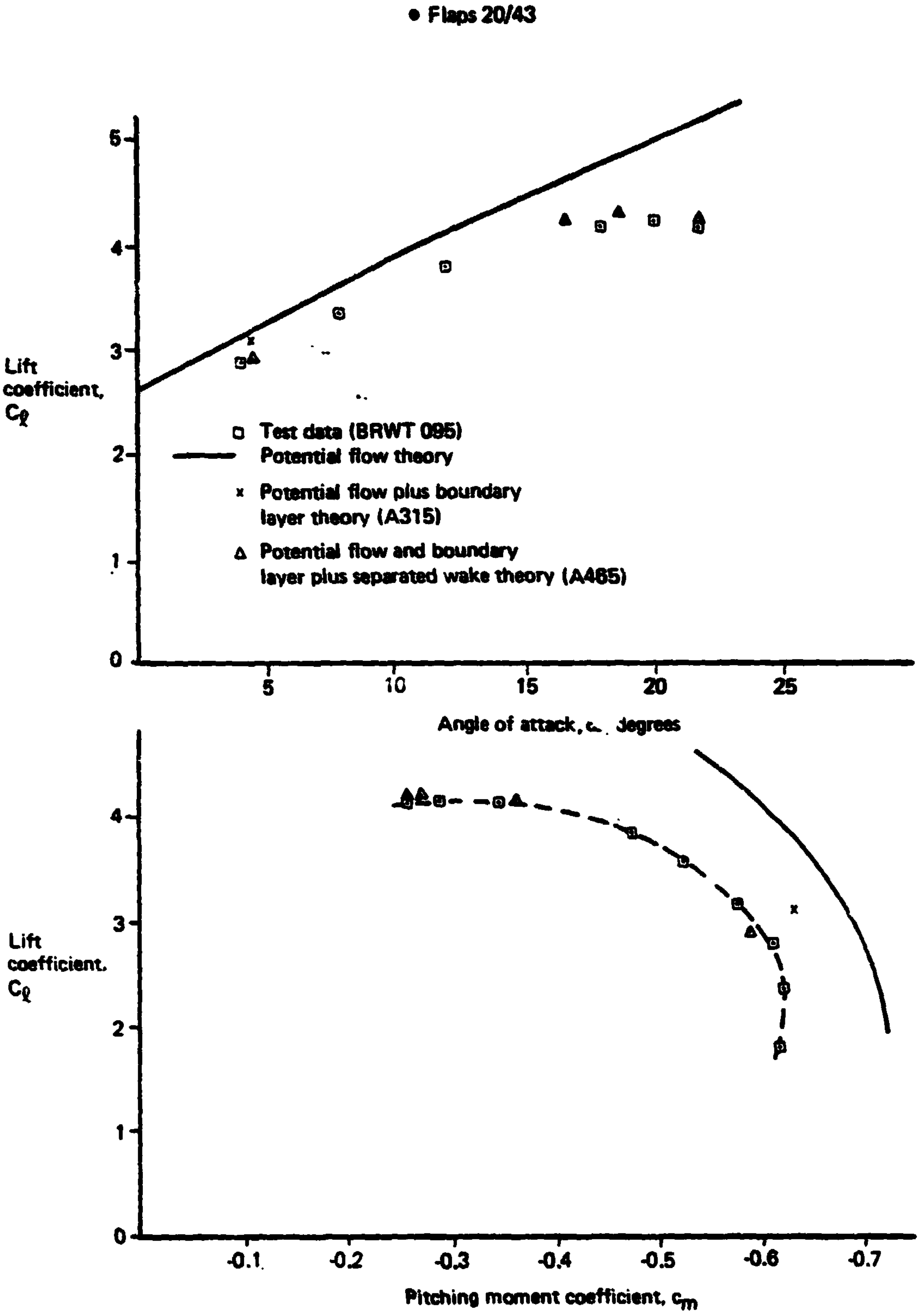

Figure 8. Lift and Pitching Moment Characteristics of Baseline Four-Element Airfoil

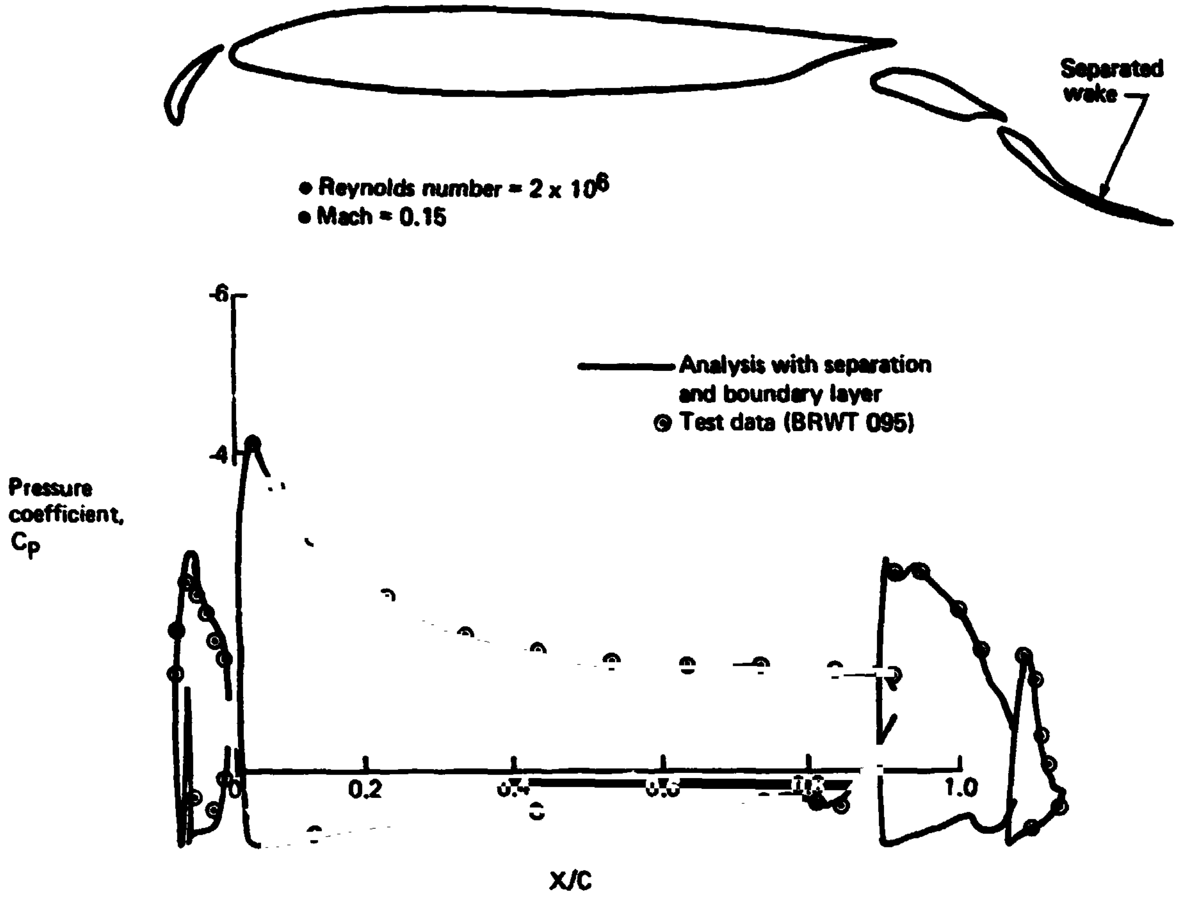

Figure 9. Comparison of Theoretical and Experimental Pressures on Baseline Airfoil—Angle of Attack = 4.4 deg

Procedure

The basic computer programs employed in this analysis are the Contractor-developed VISC and A465 programs. They were used to compute the effects of the boundary layer and separated wakes on the pressure distribution of the baseline flap system. This was accomplished by computing the boundary layer characteristics and points of separation using the VISC program and then employing the A465 program to solve the wake outer boundary problem iteratively in order to provide the proper wake shape and size from which a new pressure distribution was computed. In this way, the inviscid effect of separation was accounted for. The new pressure distribution was then used to recompute the boundary layer characteristics and separation points. This cycle was repeated until a stable solution for separation point and boundary layer thickness was found.

Using this process, the separations and boundary layers on all airfoil segments of the multielement airfoil section were modeled, starting from the trailing element and proceeding forward until separated wakes and boundary layers were being treated simultaneously on all elements. The technique of working forward from the trailing element was adopted to improve convergence. The VISC and A465 programs, and the coupling procedure, are described in more detail in appendix B.

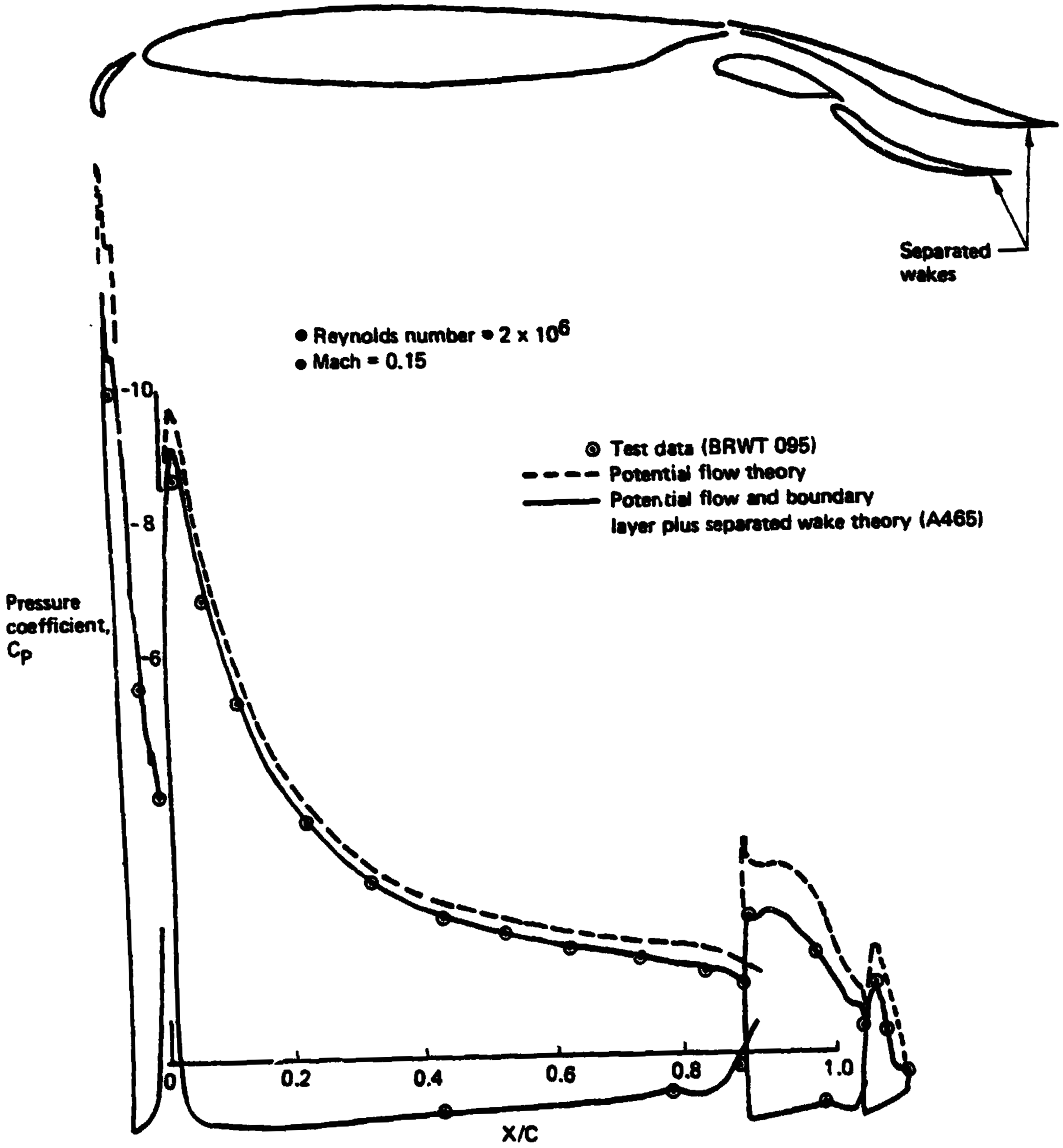

Figure 10. Comparison of Theoretical and Experimental Pressure on Baseline Airfoil— Angle of Attack = 16.6 deg

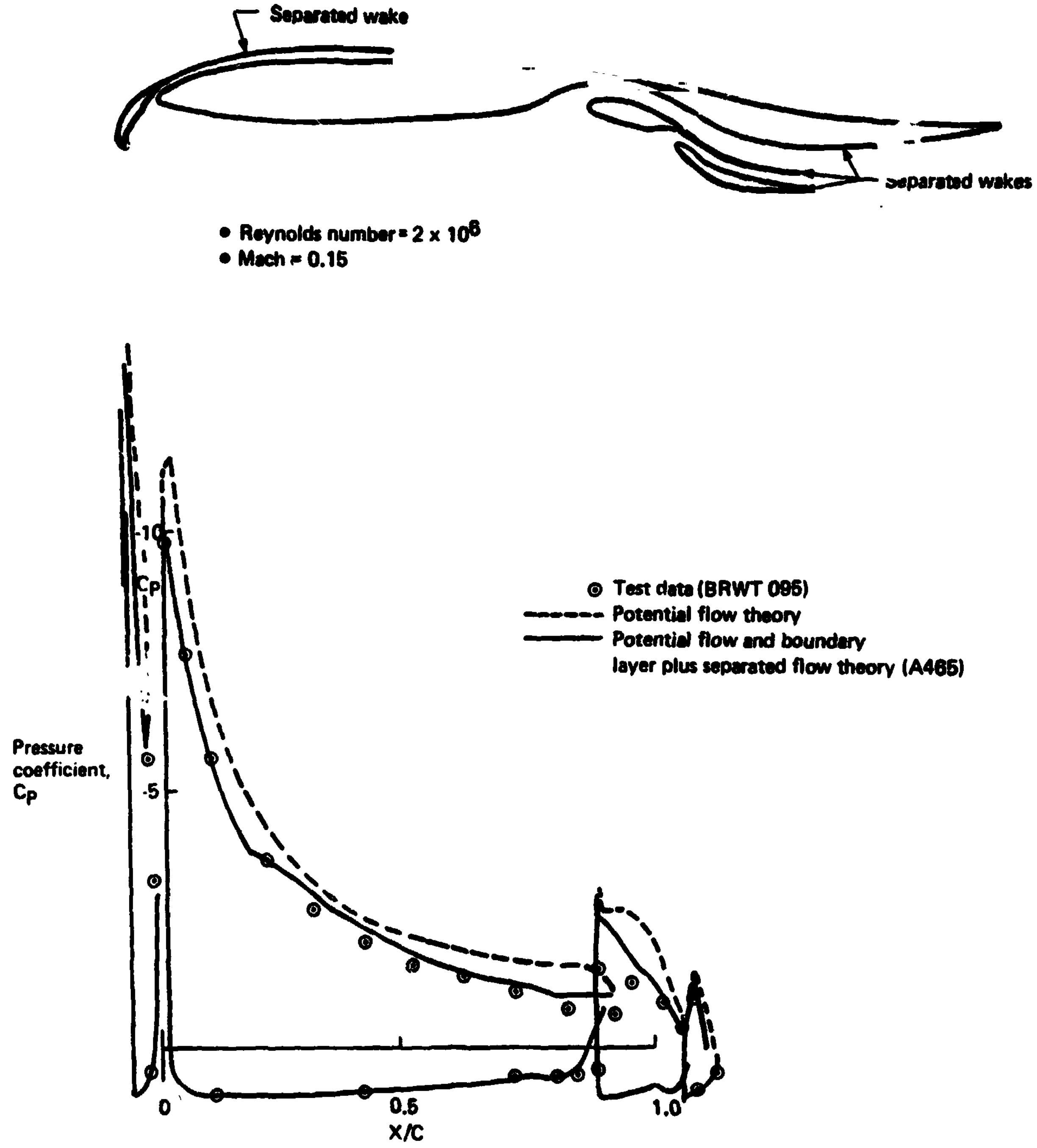

Figure 11. Comparison of Theoretical and Experimental Pressures on Baseline Airfoil—Angle of Attack = 21.7 deg

Typical output is shown in figures 12 through 15 for an analysis of the baseline flap system at 21.7-deg angle of attack. In figure 12, no wakes or boundary layers have been modeled; i.e., the pressure distribution is that of potential flow alone. In figure 13, the aft flap separation and boundary layer are modeled; in figure 14, the main flap and aft flap separations and boundary layer are modeled; in figure 15, the wing, main flap, and aft flap; and finally, in figure 11, the separations and boundary layers on all segments are modeled (i.e., separation points converged and wake shapes determined simultaneously). The lift and pitching moment shown earlier in figure 8 at 21.7-deg angle of attack result from integration of the final pressure distribution in figure 11.

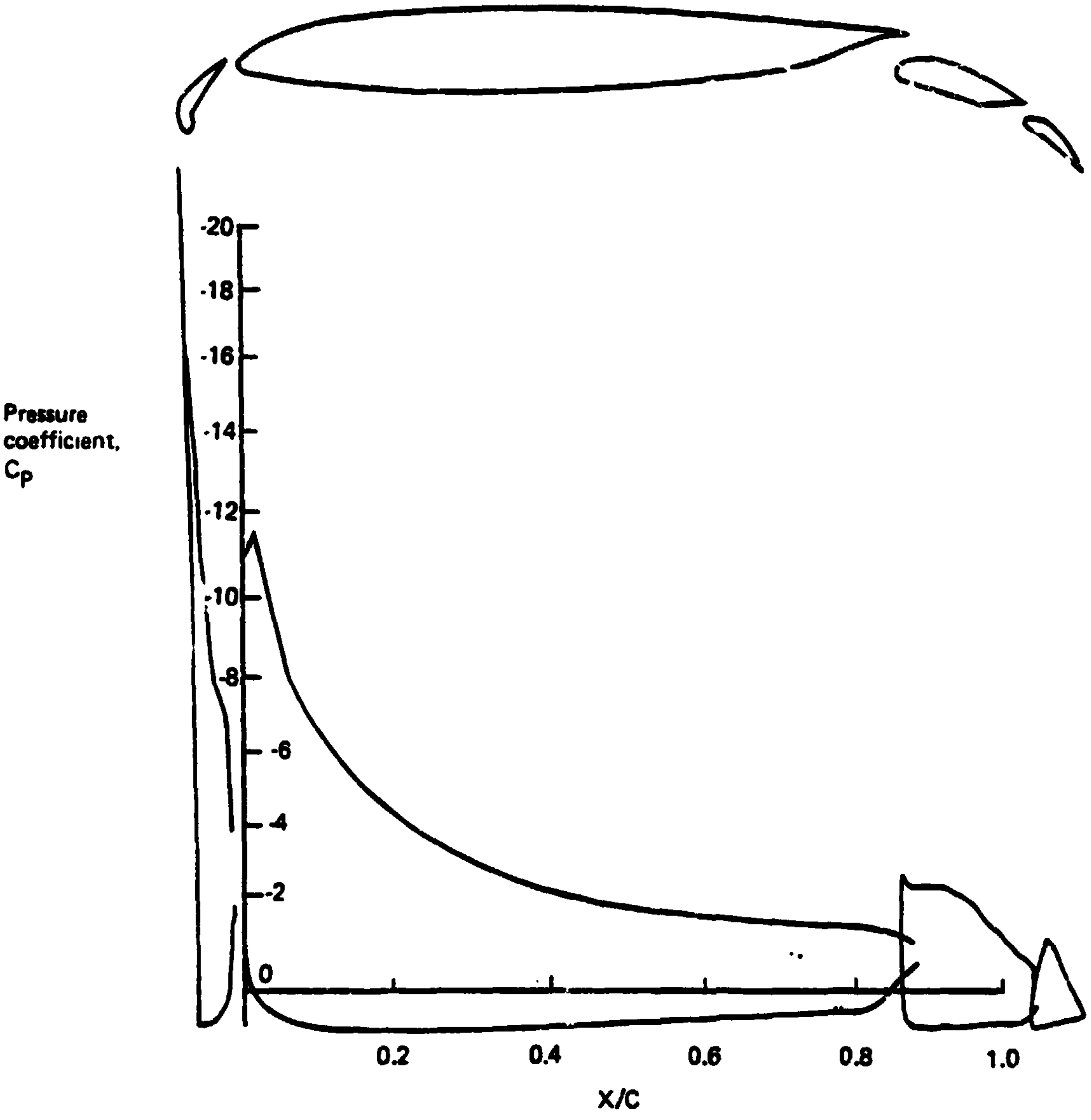

Figure 12. Potential Flow Pressure Distribution of Baseline Airfoil—Angle of Attack = 21.7 deg (A465 Analysis)

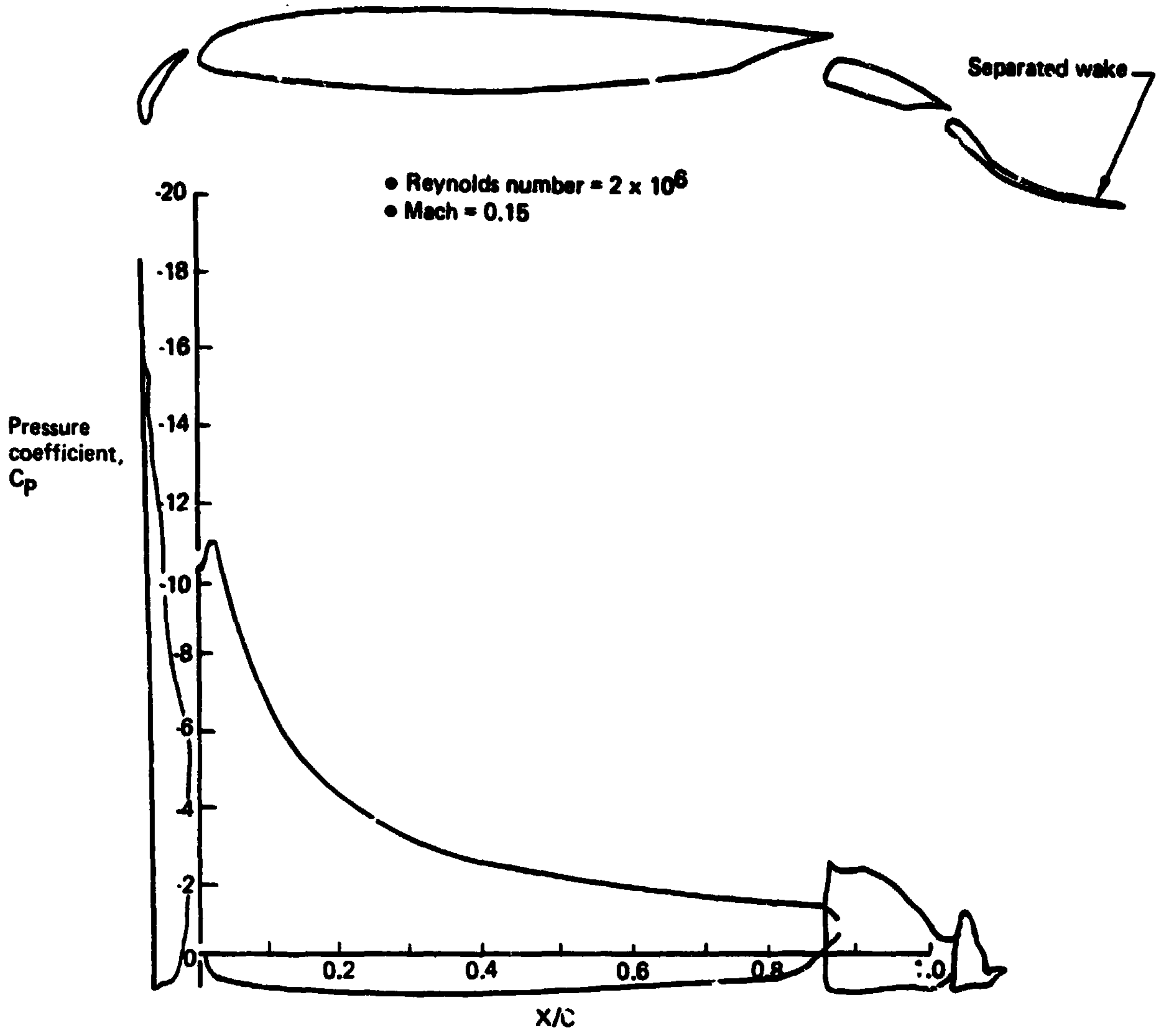

Figure 13. Theoretical Pressure Distribution on Baseline Airfoil—Separation Modeled on Aft Flap Only—Angle of Attack 21.7 deg (A465 Analysis)

It should be noted that the boundary-layer technique employed in these analyses considered the wall layer only. Detailed boundary layer measurements have shown that for reasonably sized slots commonly found in a well-developed high-lift airfoil, such as the baseline, the trailing-edge flap boundary layers are not confluent, and the slight confluence seen aft of the leading-edge flap does not severely affect the calculation of separation points on the wing. A highly confluent configuration could be assembled, but for the nearly optimized configurations discussed in this document, confluence is not important for calculation of lift.

4.1.2 Analysis of Baseline Section $C_{l_{max}}$ at Flight Reynolds Number

The primary objectives of this task were (1) to provide a performance basis, at flight Reynolds number, with which to compare the results of the design efforts, and (2) to

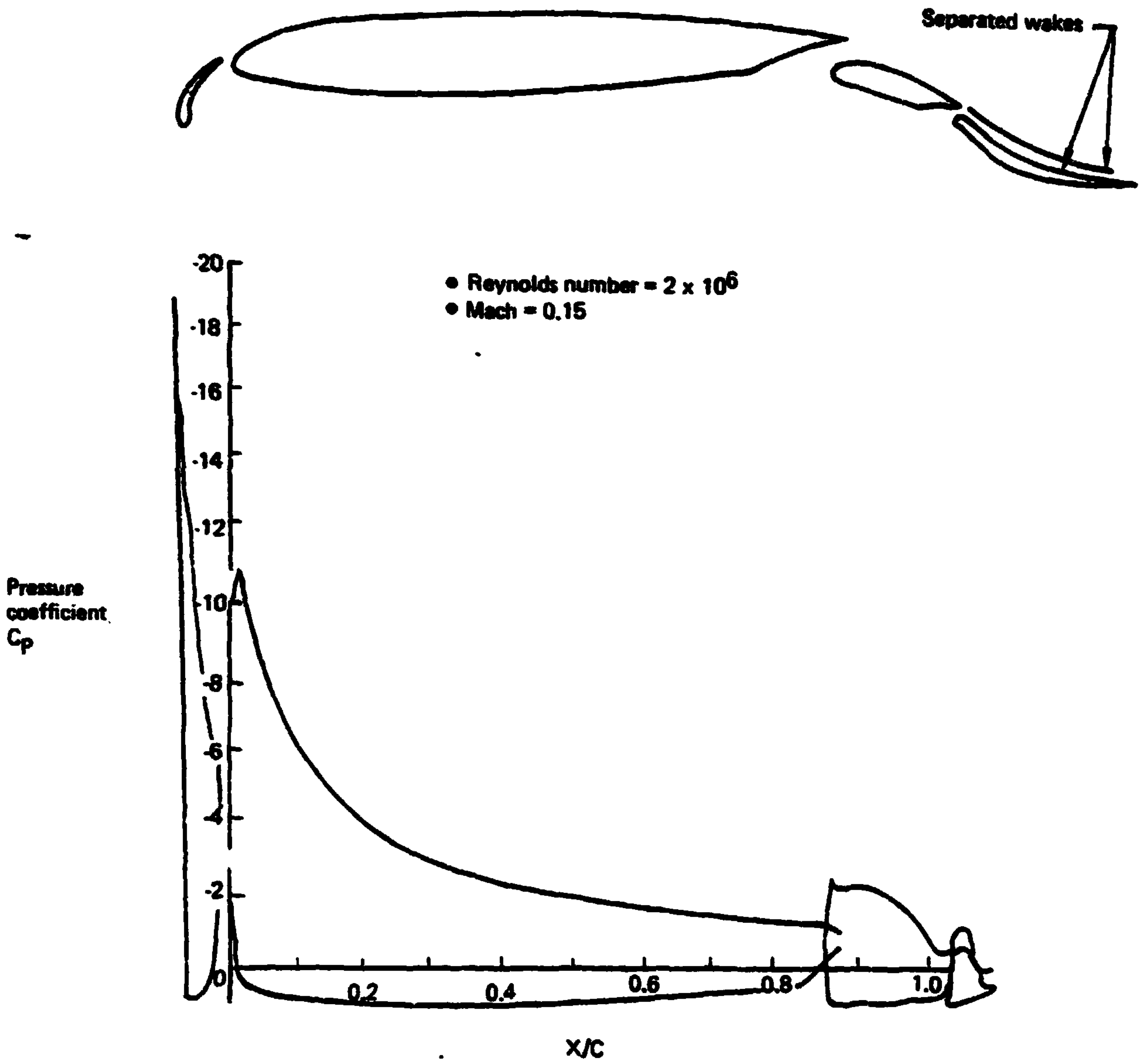

Figure 14. Theoretical Pressure Distribution on Baseline Airfoil—Separation Modeled on Aft and Main Flaps Only—Angle of Attack = 21.7 deg

compare predicted maximum airfoil lift coefficient sensitivity to Reynolds number with test results of similar configurations.

Results

The calculated lift curves at wind tunnel Reynolds number (2×10^6) and flight Reynolds number (17×10^6) are compared in figure 16. For the baseline airfoil, this analysis indicates a $C_{l_{max}}$ increase from the wind tunnel Reynolds number level of 4.22 to 4.6 at flight Reynolds number. Figure 17 shows that the calculated Reynolds number sensitivity compares well with experimental data of similar configurations tested in a variable-density tunnel (the NAE facility in Ottawa, Canada, ref. 4).

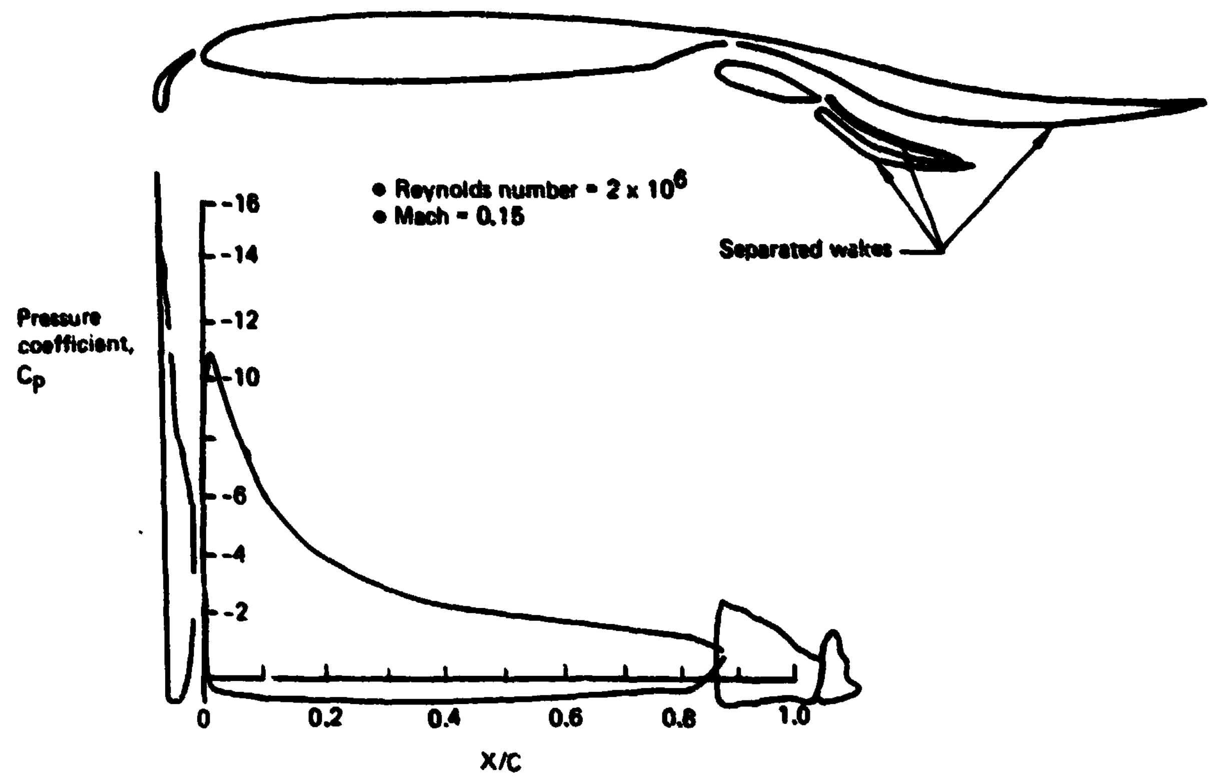

Figure 15. Theoretical Pressure Distribution on Baseline Airfoil—Separation Modeled on Main Airfoil, and Main and Aft Flaps—Angle of Attack = 21.7 deg (A465 Analysis)

Procedure

The analysis technique employed was identical to that used in the wind tunnel Reynolds number analysis discussed in detail in section 4.1.1. Figures 18 through 20 show the wake shapes and resultant pressure distributions that were produced by the flight Reynolds number analysis at 18.6-, 21.7-, and 24-deg angles of attack, respectively.

4.1.3 Design at Flight Reynolds Number for Best $C_{l_{max}}$

In this subtask, a four-element, high-lift airfoil section was designed to maximize lift coefficient at flight Reynolds number using advanced computerized techniques.

Technology gains were explored in terms of $C_{l_{max}}$ available by designing a high-lift system to full-scale Reynolds numbers, rather than to the Reynolds number characteristic of atmospheric wind tunnels. To ensure that improvements were due only to the increased design Reynolds number and more advanced design methodology, the geometric constraints imposed on the baseline high-lift system were also applied to this design. As a result, the $C_{l_{max}}$ design configurations were required to have the same transonic shape, number of elements, flap chord lengths, and Fowler motion as the baseline. Furthermore, the freedom to shape the various flap elements was constrained in exactly the same way

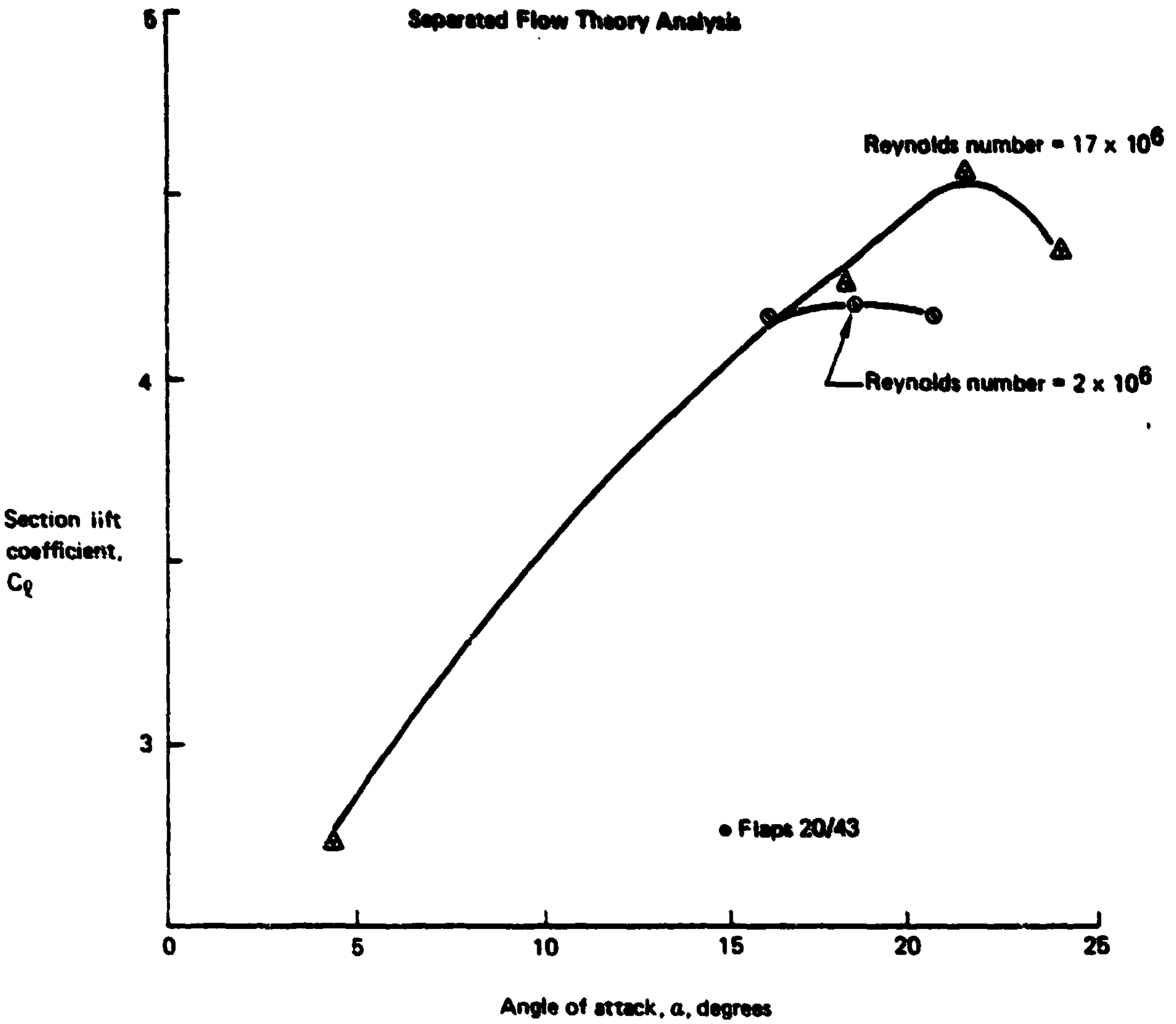

Figure 16. Theoretical Lift Curves of Baseline Airfoil at Wind Tunnel and Flight Reynolds Numbers

as was the baseline flap system. These constraints will be discussed in more detail later in this section.

Results

Maximum lift coefficient, based upon analysis, was increased from the baseline level of 4.6 to a maximum lift coefficeint level of 5.2 for the new design. This is a 13% increase. The computed lift curves, through maximum lift, of the two high-lift systems are compared in figure 21. Lift coefficient at 6-deg angle of attack was increased from the baseline level of 3.0 to a level of 3.35 for the new design, an 11% increase.

The geometries of the baseline system and the new flap system are illustrated in figure 22 to show differences in shape and deflection of the flaps. Pressure distributions and new shapes for the high Reynolds number designs are compared with the baseline pressure

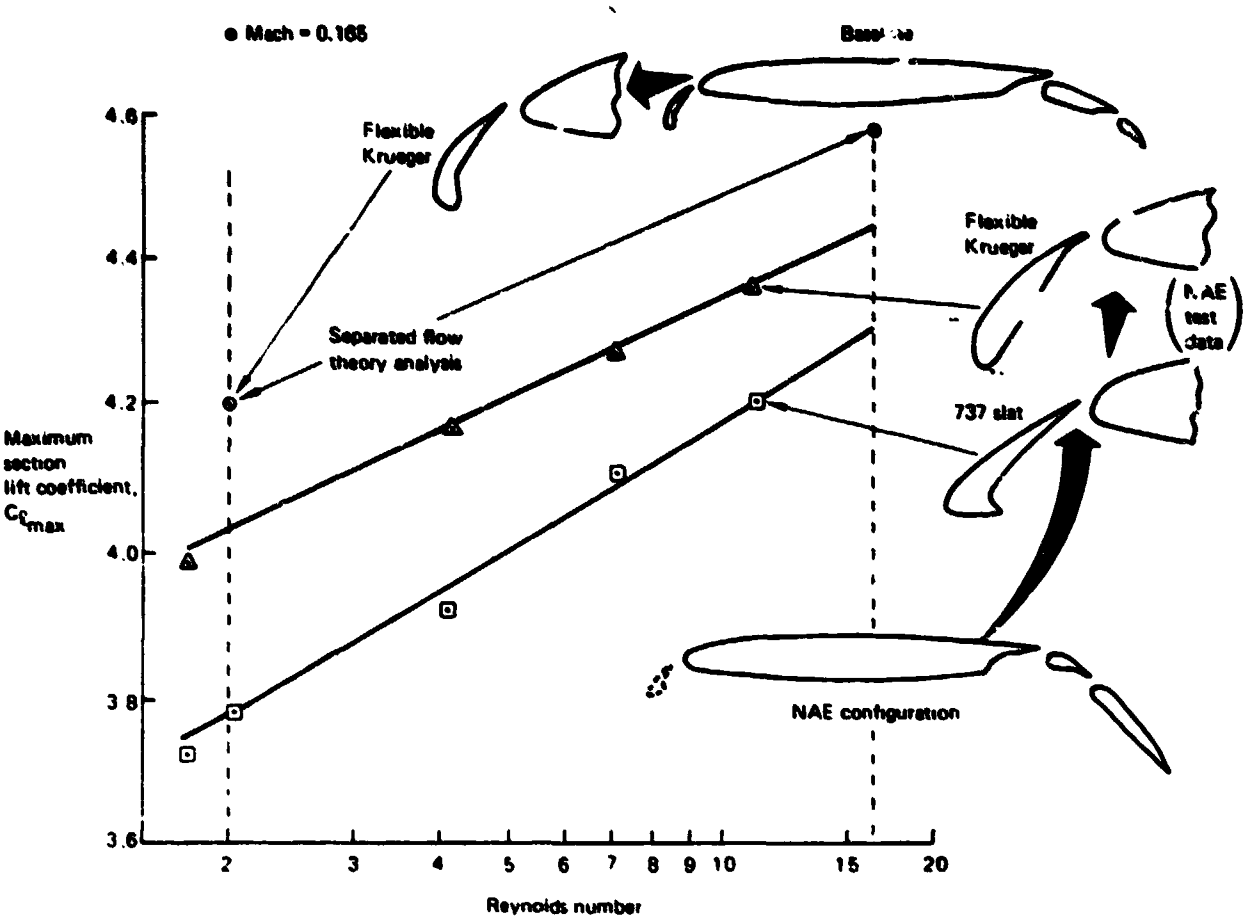

Figure 17. Variation of $C_{\ell_{max}}$ With Reynolds Number

distributions in figures 23 through 26. These figures also compare flap geometries and indicate the regions on the flap surfaces that could be modified. It should be noted that design changes to the aft and main flap were constrained to reshaping of the forward sections.

An important goal of the effort was to develop a rational design method for multielement airfoils using the advanced tools that have been described. This method is depicted by flow charts in figures 27 and 28 and is discussed in more detail in the following paragraphs.

Procedure

The multielement airfoil design flow charts are described in this section, using the maximum lift design at flight Reynolds number as an example. The intent of this approach is to familiarize the reader with the design processes used in the EET design work and to illustrate the decisions made and the constraints involved in the redesign of the baseline high-lift system for $C_{l_{max}}$ at flight conditions.

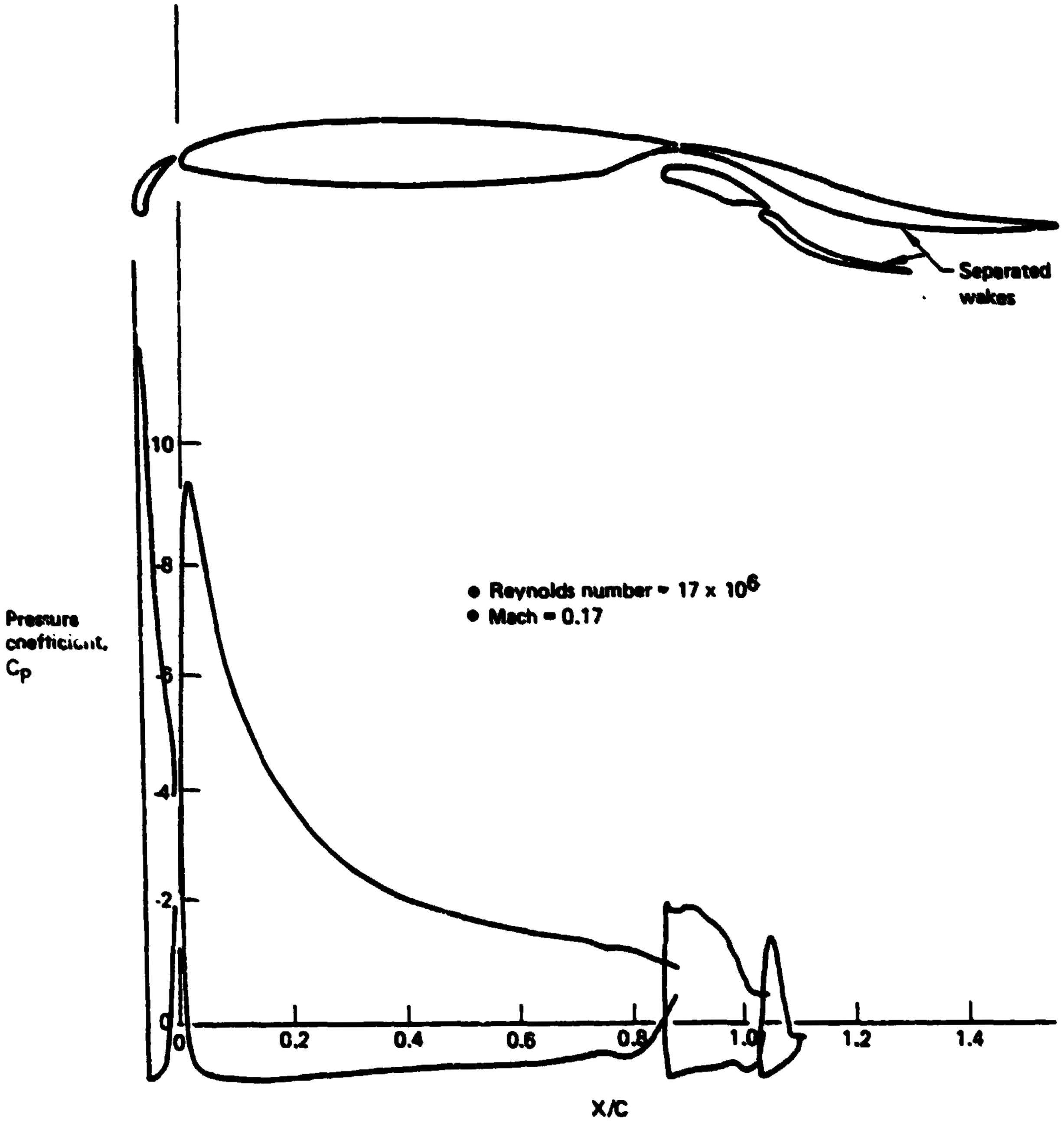

Figure 18. Theoretical Pressure Distribution on the Baseline Airfoil at Flight Reynolds Number—Angle of Attack = 18.6 deg

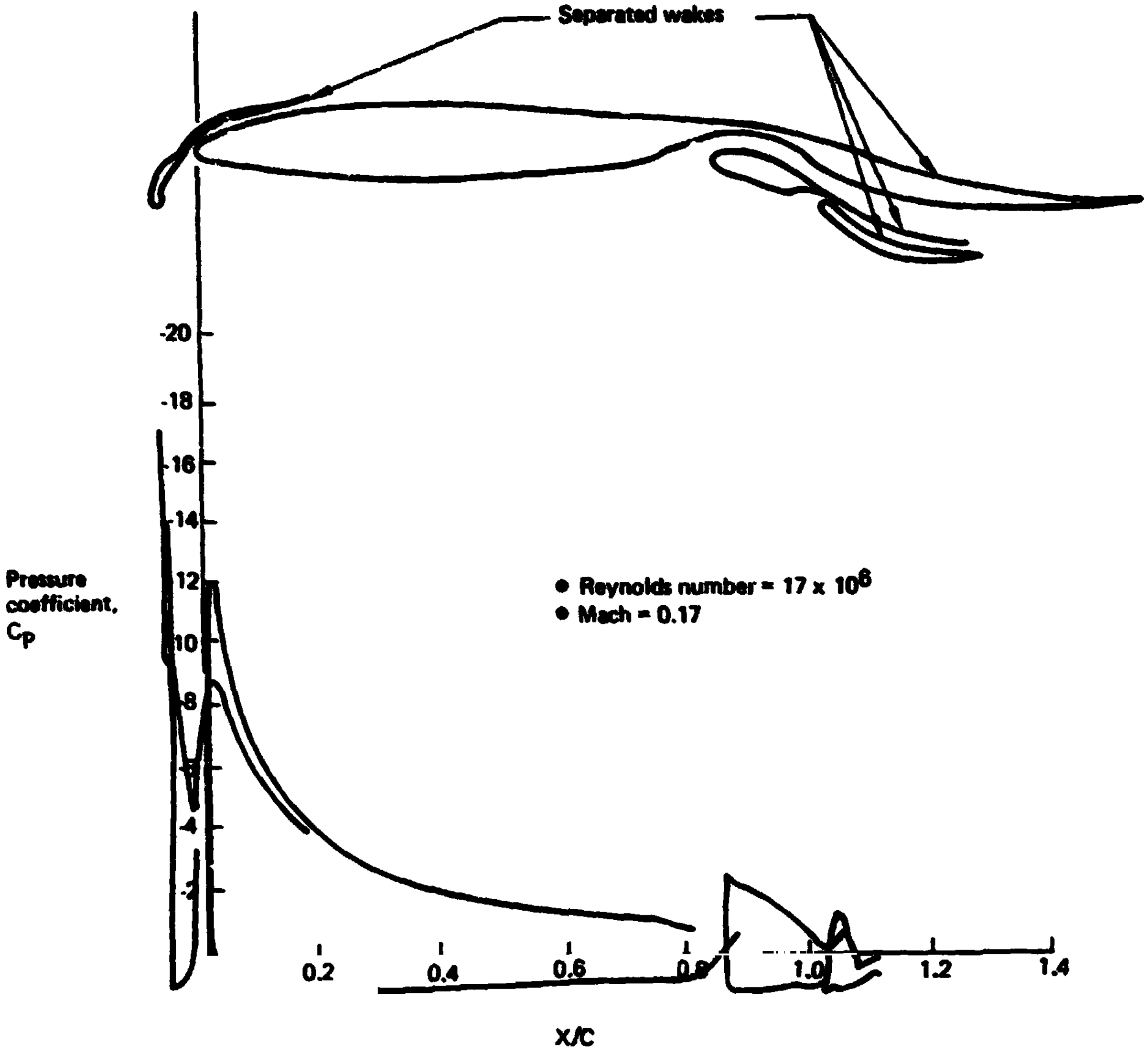

Figure 19. Theoretical Pressure Distribution on the Baseline Airfoil at Flight Reynolds Number—Angle of Attack = 21.7 deg

The first task in the design process was to adequately define the new section in terms of design point(s) and constraints. For the $C_{l_{max}}$ design at flight Reynolds number, this definition was as follows:

a. Aerodynamic performance design points: Maximize airfoil lift coefficient at flight Reynolds number.

b. Aerodynamic performance constraints: The amount of separation on the aft flap computed for the design should be the same as that computed for the baseline flaps at approach lift levels. No constraints were placed on either the drag or pitching moment.

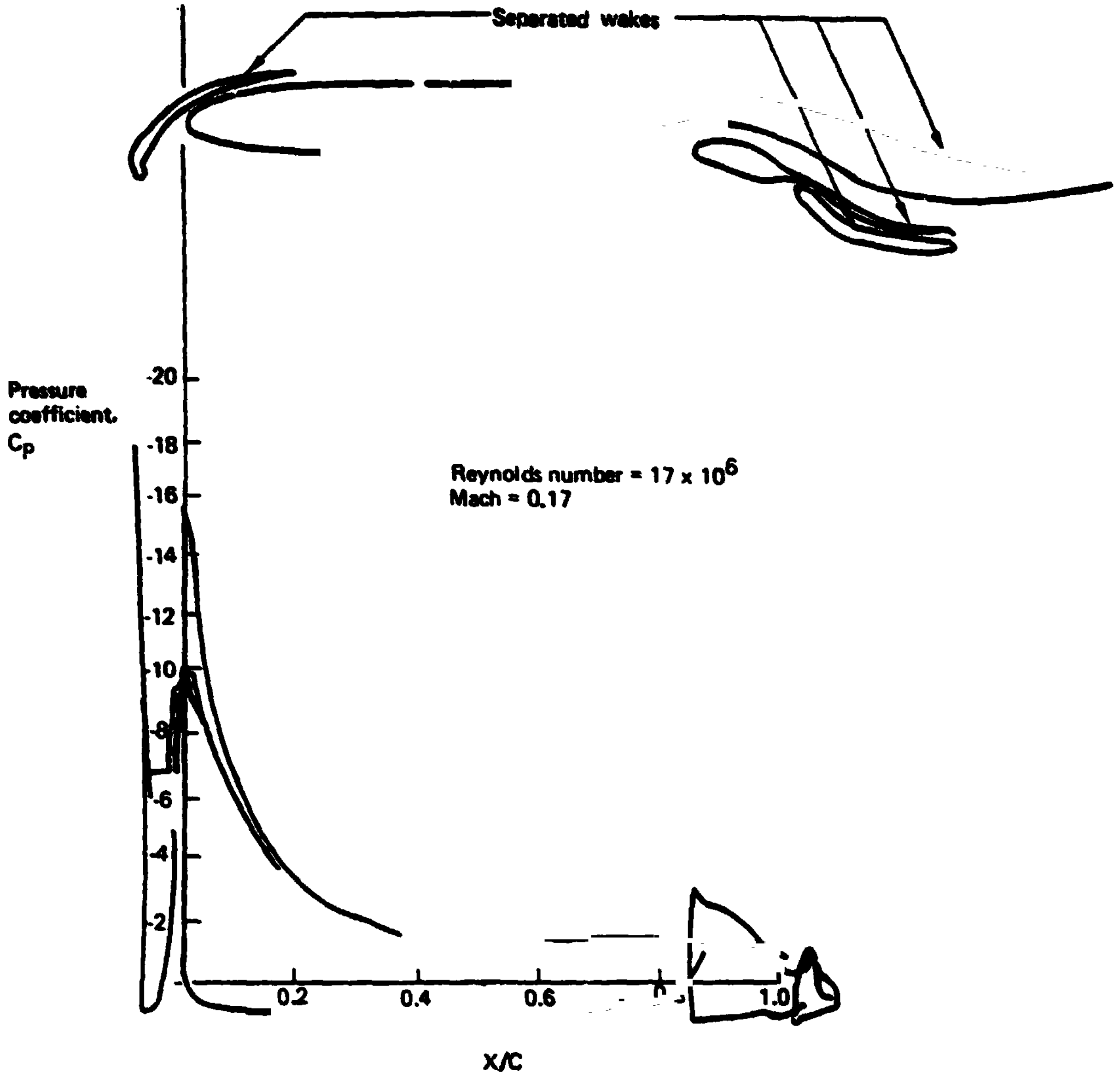

Figure 20. Theoretical Pressure Distribution on the Baseline Airfoil at Flight Reynolds Number—Angle of Attack = 24 deg

c. Flow conditions: Design Reynolds number = 17 x 10^6; design Mach number = 0.17. These correspond to the flow conditions of an outboard section of the EET study transport configuration at stall and at maximum landing weight.

d. Geometric constraints:

1. The leading-edge flap and trailing-edge flaps, when retracted, produce the same cruise airfoil contour as the baseline.

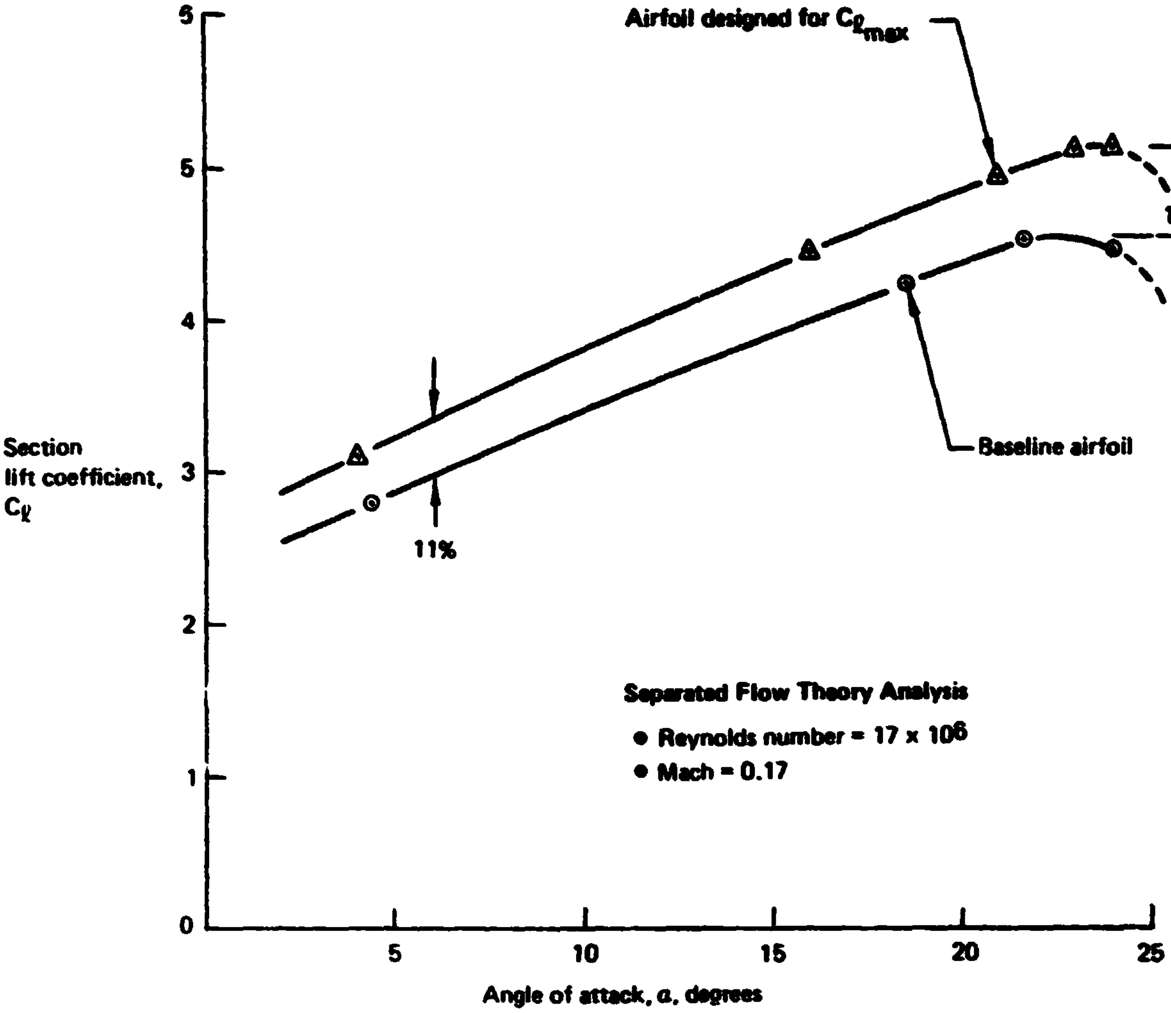

Figure 21. Theoretical Lift Curves of the $C_{\ell_{max}}$ Design and the Baseline Airfoil at Flight Reynolds Numbers

2. The leading-edge device was the only flexible device. The trailing-edge flaps, both the main flap and the aft flap, were defined to be rigid with extension.

3. The leading-edge device could not have greater extension than the baseline device.

4. The nested chords of the trailing-edge flaps are identical to the baseline, and the chord division between the main and the aft flap were identical to the baseline.

5. The positions of the trailing edge of the wing cove and the main-flap cove were identical to the baseline. The implication of this constraint was that the amounts of the main and the aft flap that were buried inside the wing when retracted (and therefore available for modification in the design process) were identical to those of the baseline configuration.

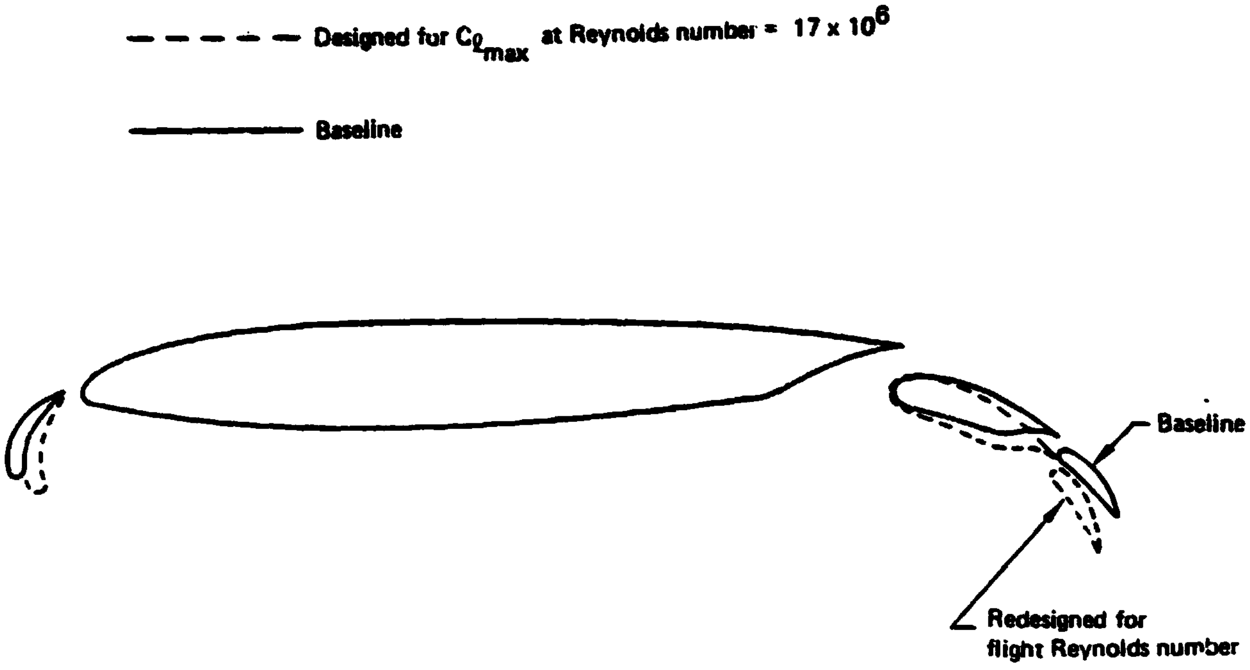
Designed for $C_{\ell_{max}}$ at Reynolds number = 17 x 10^6
Baseline
Baseline
Redesigned for flight Reynolds number

Figure 22. Comparison of High Lift System Geometry

The second task in the design process was to choose the number and relative size of the airfoil elements in the high-lift section and to assemble a starting configuration. This could have required a preliminary study of aerodynamic requirements using the A427 (ref. 2) program, a Contractor-developed inverse boundary-layer program that will allow the number of elements required to be determined for a given lift level. This program is described in more detail later in this section and in appendix C. In the case of the $C_{l_{max}}$ design, the baseline high-lift system was used as the starting geometry.

The third task in the design process was to analyze the starting airfoil section in enough detail to determine what limits its design point performance. In the case of the $C_{l_{max}}$ design, the starting configuration was the baseline high-lift section already analyzed at flight Reynolds number. This analysis showed that the baseline main flap was too lightly loaded and was not providing enough trailing-edge pressure reduction on the wing trailing edge, causing early trailing-edge separation on the wing. Preliminary studies using the inverse boundary-layer program (A427) (ref. 2) also resulted in the following conclusions:

a. The aft flap could be more heavily front loaded, if designed for flight conditions, without increased separation on its upper surface. This would reduce the pressure at the main flap trailing edge and increase the amount of load the main flap could carry.

b. The main flap could be more heavily loaded and more front loaded, if designed for flight conditions, resulting in much greater reduction in pressure at the wing trailing edge.

c. The leading-edge flap loading could be increased if the pressure distribution were redesigned for full-scale Reynolds numbers.

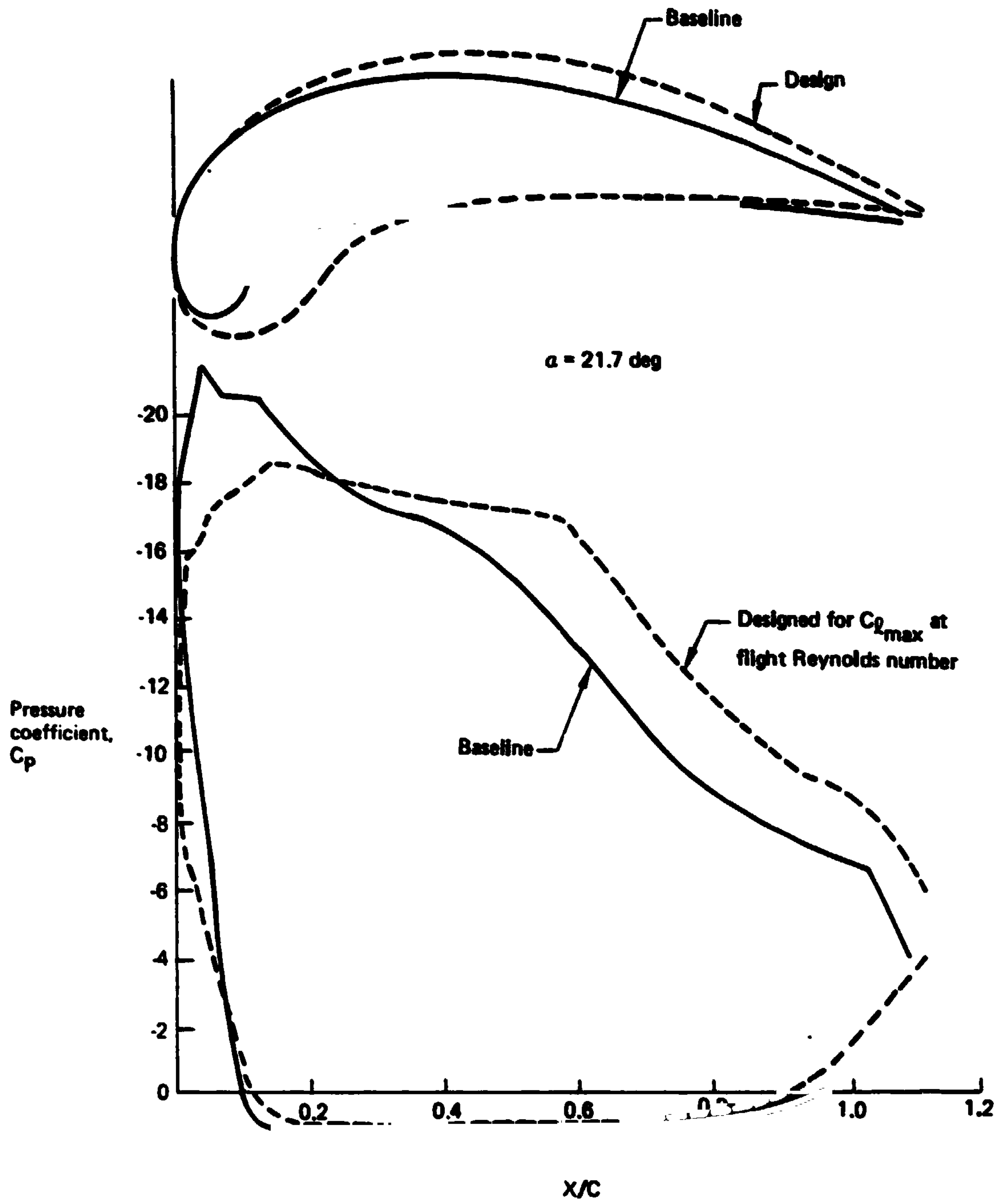

Geometric constraint: Same size as baseline

Figure 23. Comparison of Baseline and Redesigned Pressure Distributions and Geometry—Leading Edge Flap

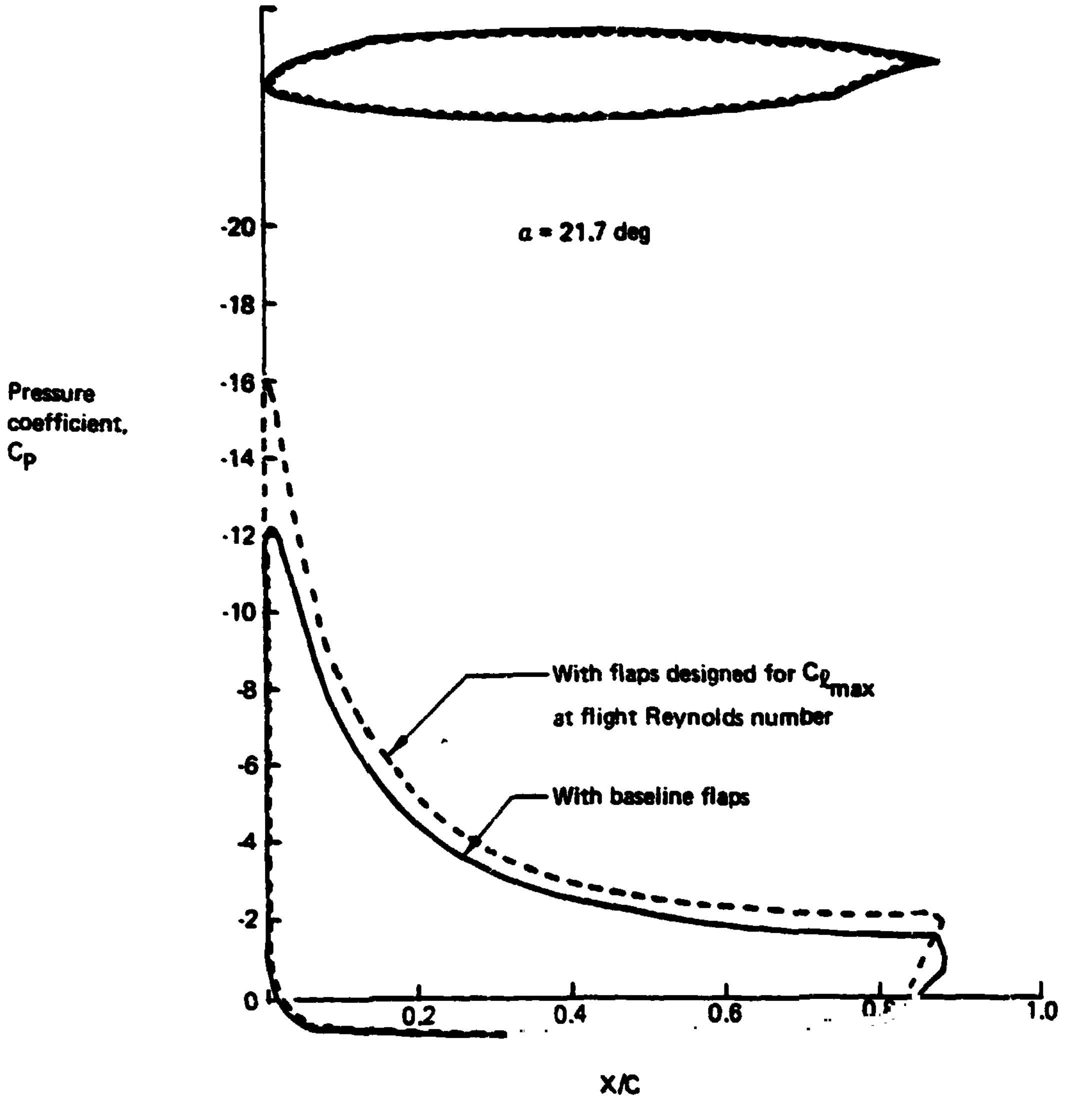

Geometric constraint: No modifications allowed

Figure 24. Comparison of Baseline and Redesigned Pressure Distributions and Geometry—Main Wing

These conclusions led directly to the fourth task in the design process, reshaping the airfoil elements. Each airfoil element was designed in turn, starting with the aft flap and proceeding forward to the leading-edge device, using the process described in figure 28.

The first task in the process of designing an airfoil element was to design the pressure distribution using the inverse boundary-layer program (A427). This program was one of the primary computational tools used in the design work reported here and is described in more detail in appendix C.

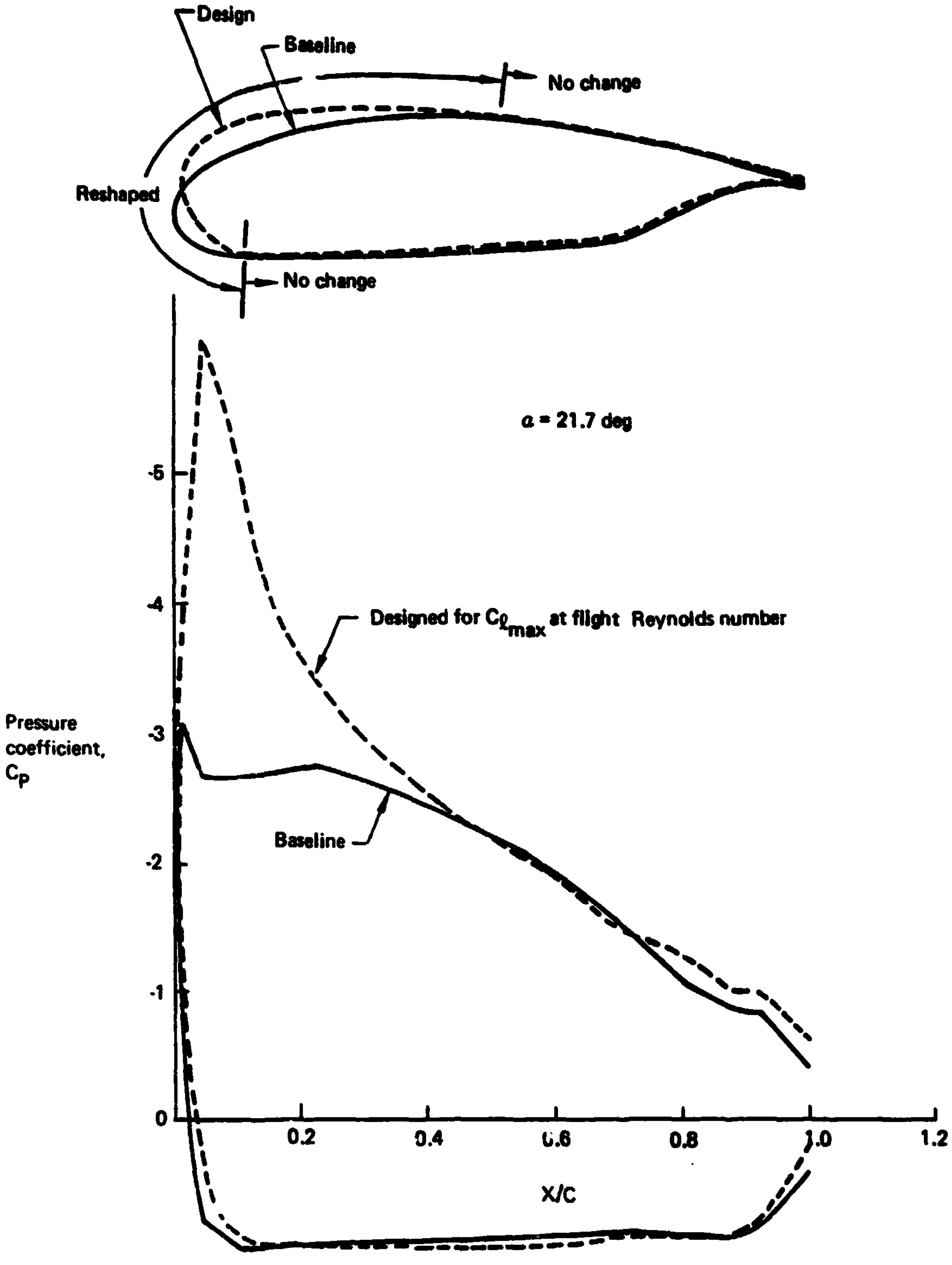

Geometric Constraint: Shape changed in buried regions only

Figure 25. Comparison of Baseline and Redesigned Pressure Distributions and Geometry—Main Flap

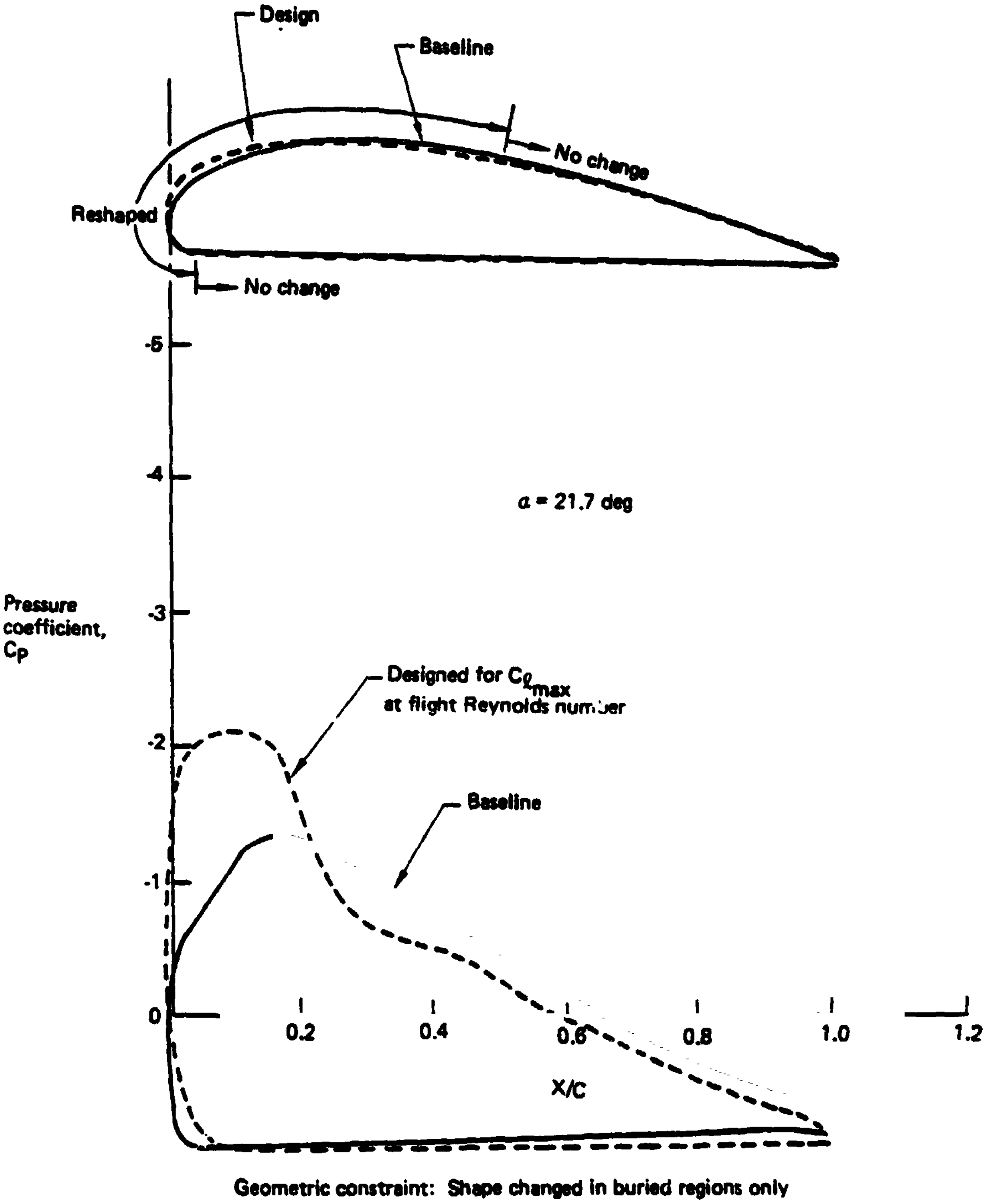

Figure 26. Comparison of Baseline and Redesigned Pressure Distribution and Geometry—Aft Flap

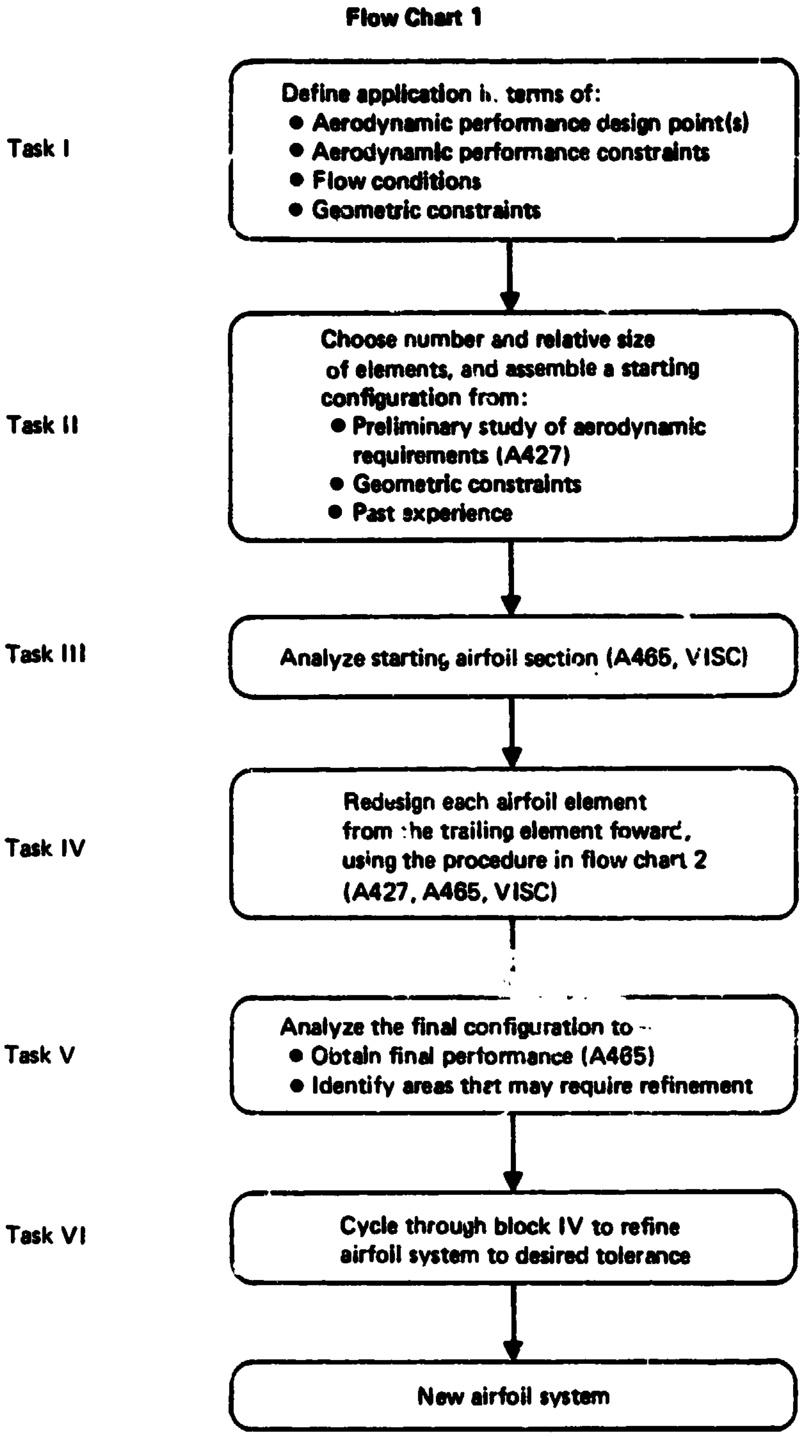
Flow Chart 1
Task I
Define application in terms of:
• Aerodynamic performance design point(s)
• Aerodynamic performance constraints
• Flow conditions
• Geometric constraints
Task II
Choose number and relative size of elements, and assemble a starting configuration from:
• Preliminary study of aerodynamic requirements (A427)
• Geometric constraints
• Past experience
Task III
Analyze starting airfoil section (A465, VISC)
Task IV
Redesign each airfoil element from the trailing element foward, using the procedure in flow chart 2 (A427, A465, VISC)
Task V
Analyze the final configuration to –
• Obtain final performance (A465)
• Identify areas that may require refinement
Task VI
Cycle through block IV to refine airfoil system to desired tolerance
New airfoil system

Figure 27. Multielement Airfoil System Design Process

Flow Chart 2

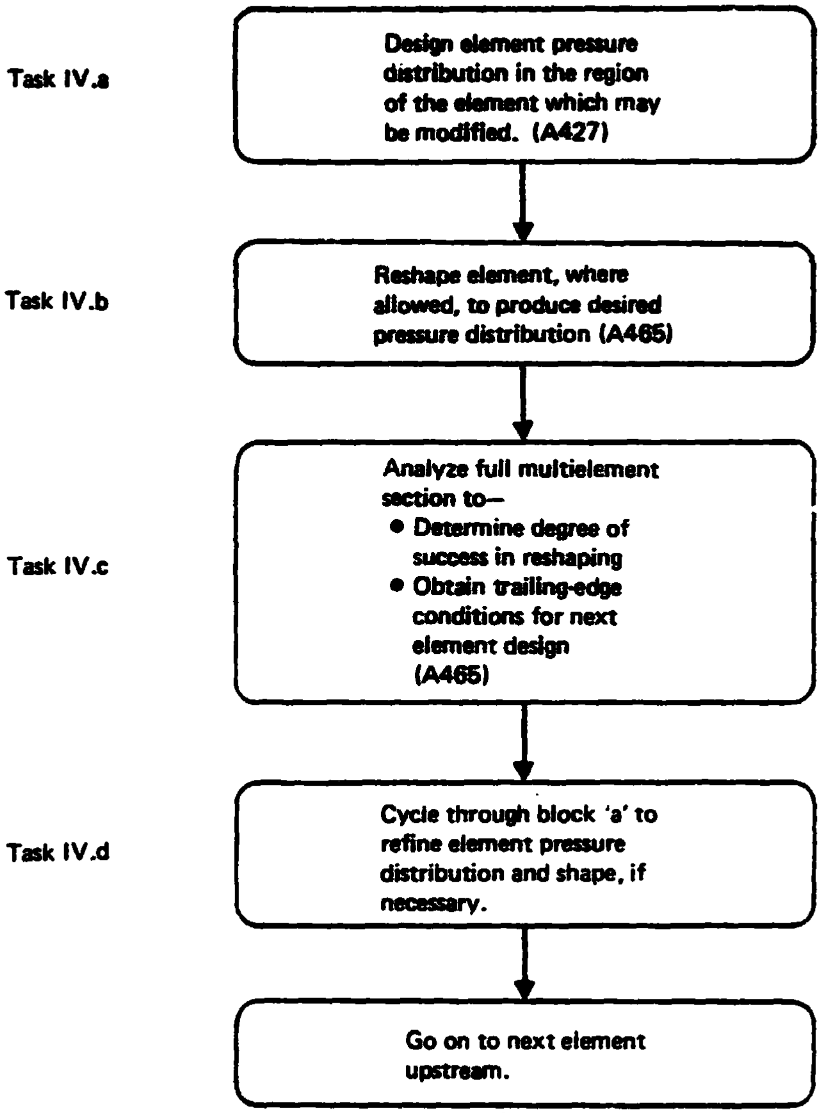
Task IV.a
Design element pressure distribution in the region of the element which may be modified. (A427)
Task IV.b
Reshape element, where allowed, to produce desired pressure distribution (A465)
Task IV.c
Analyze full multielement section to—
• Determine degree of success in reshaping
• Obtain trailing-edge conditions for next element design
(A465)
Task IV.d
Cycle through block 'a' to refine element pressure distribution and shape, if necessary.
Go on to next element upstream.

Figure 28. Design of an Airfoil Element

In the $C_{l_{max}}$ design, the trailing-edge flap pressure distributions were redesigned to produce as much trailing-edge suction for the next element forward as was consistent with the following constraints:

a. There would be no more separation on the redesigned flap than was indicated by analysis of the baseline.

b. The flap loads carried by the redesigned flaps would be equal to or greater than the baseline flaps. This was done to ensure that lift at a constant angle of attack would be improved or maintained.

c. The pressure distribution could not be modified where the geometry was fixed.

This concept allowed the main flap, the wing, and ultimately the leading-edge flap to be more highly loaded than they were on the baseline configuration, without separating, because their trailing-edge pressures (that is, the pressure to which they must recover) were lower.

Applying this philosophy to the baseline trailing-edge flaps resulted in the flap pressure distributions shown in figures 25 and 26. Of particular interest is the reduction in pressure near the leading edge of the main flap where the redesigned pressure distribution achieved a pressure coefficient of -6.0, compared with the baseline leading-edge pressure coefficient of -3.0. Further, the position of the minimum pressure on the main flap was located to have maximum influence on the wing trailing edge. The pressure distribution modification on the main flap resulted in a wing trailing-edge pressure reduction from the pressure coefficient of -1.5 for the baseline to -2.0 for the redesigned main flat (see fig. 24). The effect of this change was to allow the wing to operate at a higher lift level for a given amount of separation.

Having redefined the pressure distribution on an element, the next step was to reshape the element to produce the desired pressure distribution. It was accomplished using the design mode of the A465 program. In this mode, all or any part of the multielement, high-lift section can be reshaped to the specified pressure distribution.

Because of the overconstrained nature of the design problem when only a portion of the flap surface was available for modification, the program could not always converge to exactly the specified pressure distribution. This was particularly true when edge constraints (e.g., slope matching conditions between the fixed portion of the airfoil and the modifiable portion of the airfoil) existed. The result of the design, then, was a pressure distribution that was as close to the specified pressure distribution as possible considering the restraints. Because of this, the modified section was analyzed after the design run was completed to determine the degree of success of the reshaping. It was occasionally necessary to refine the design pressure distribution for the element to more closely reflect the geometric constraints of the particular design problem.

Once the reshaping process converged on the desired pressure distribution, an analysis of the high-lift system with the modified element provided the trailing-edge pressure distribution for the next element forward. The trailing-edge conditions then were used as aerodynamic constraints in the design of the new pressure distribution on that element. The pressure distribution design-reshaping procedure was repeated until all the elements had been reshaped.

Once all the elements had been reshaped, the lift curve near Cl_{max} was analyzed to identify areas on the new high-lift system that might require some refinement. This refinement process is similar to the initial reshaping process.

During the Cl_{max} design, very little refinement was required in the design of the trailing-edge flaps; typically, two cycles through the reshaping process for each element were sufficient to obtain the desired performance. Because of the increased curvature of the flow field near the wing leading edge and the resultant greater nonlinearity of the design problem, the leading-edge flap design was more difficult and required some six iterations of shape refinement and pressure distribution refinement to achieve what was felt to be its potential for Cl_{max} improvement.

4.1.4 Design at Flight Reynolds Number for Simplification

In the design work described in section 4.1.3, the benefits of rationally designing a high-lift section to full-scale Reynolds numbers were applied to improving maximum lift coefficient. The intent of the simplified flat design was (1) to use the same computational techniques to design a high-lift system to the same maximum lift coefficient as the baseline section, while (2) applying the advantages of improved technology and higher design Reynolds numbers to designing a simpler, more efficient (i.e., lower drag) flap arrangement.

Results

The product of the design effort was a three-element, high-lift airfoil section with the following geometric features:

a. A sealed, variable-camber Krueger flap

b. A single-slotted trailing-edge flap with a simple hinged tab

This configuration is compared with the baseline four-element, high-lift system in figure 29. Ordinates describing all elements are contained in appendix D.

The major simplification produced by this design is replacement of the baseline double-slotted Fowler flap with a single-slotted Fowler flap having a simple hinged tab as shown in figure 29. The sealed, variable-camber leading-edge flap was not a simplification, but rather the result of an effort to satisfy two design requirements for the new flap system: the same maximum lift coefficient as the baseline system at flight Reynolds number, and

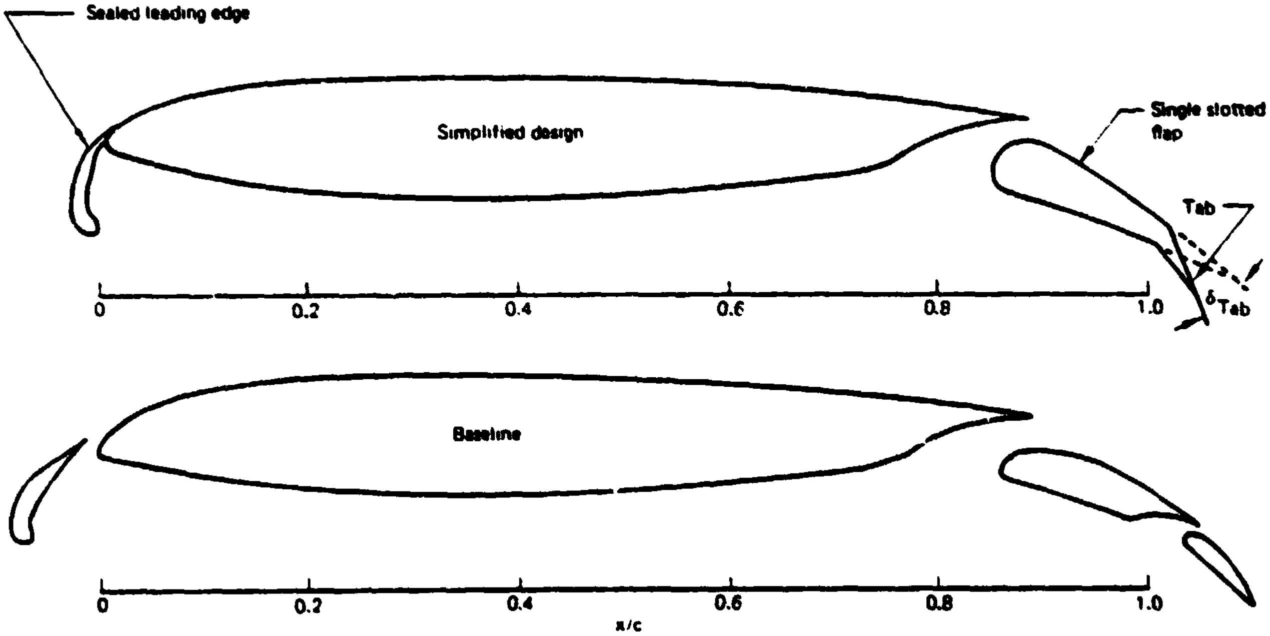

Figure 29. Simplified and Baseline High-Lift System Geometries

improved takeoff lift-to-drag characteristics at takeoff flap deflections with the tab not deflected.

Preliminary estimates based upon wind tunnel experience and a section drag polar analysis for the Denver takeoff configuration (leading-edge flap extended, trailing-edge flap retracted and no tab deflection) indicated a lift-to-drag improvement of 5.6% at Denver takeoff lift levels and 9.5% at sea-level takeoff lift levels.

Careful design of the leading-edge and trailing-edge flap shapes (where allowed) resulted in the simplified flap system having essentially the same lift performance as the baseline system. This is illustrated in figure 30.

Procedures

The same design procedures and programs that were described in detail in section 4.1.3 were employed in the design of the simplified flap system. This section generally describes the design exercise and discusses the decisions that led to crucial geometric constraints that defined the design problem.

The simplified high-lift system design represented a more difficult problem than the design for maximum lift coefficient for two reasons. First, there were the following aerodynamic design criteria and constraints on both lift and drag:

a. Maximum lift coefficient at flight Reynolds number must be equal to 4.6 (i.e., the same as the baseline).

b. Lift coefficient at 8-deg angle of attack must be greater than or equal to 3.4 (i.e., no increase in approach attitude allowed).

c. Takeoff drag should be reduced.

Second, the primary design goal, simplification, was difficult to quantify in terms of the aerodynamic performance criteria and tended to change in a discontinuous, quantum fashion.

To determine how simplification should best be accomplished, a preliminary study was performed of several possible simplification techniques. In-house wind tunnel data and preliminary-design-type sizing criteria were employed to compare the different simplification permutations. The results are displayed in table 1.

The sealed Krueger leading-edge device and single-slotted trailing-edge flap with hinged tab (configuration 5 in table 1) were chosen because, on a preliminary basis, they appeared to be the best compromise between simplicity and performance.

This decision was based upon the requirement that the baseline $C_{l_{max}}$ level (4.6) must be achieved by the new design. If a lower level of $C_{l_{max}}$ were required, a different system would have been chosen. For example, if the ground rules had been to provide the simplest system that would produce just enough $C_{l_{max}}$ to make a 64-m/s (125-Keas) approach speed at the baseline design point wing loading, the $C_{l_{max}}$ required of the outboard section would have been 4.2, and configuration 3 (the single-slotted trailing-edge flap and three-position slat) would have been chosen.

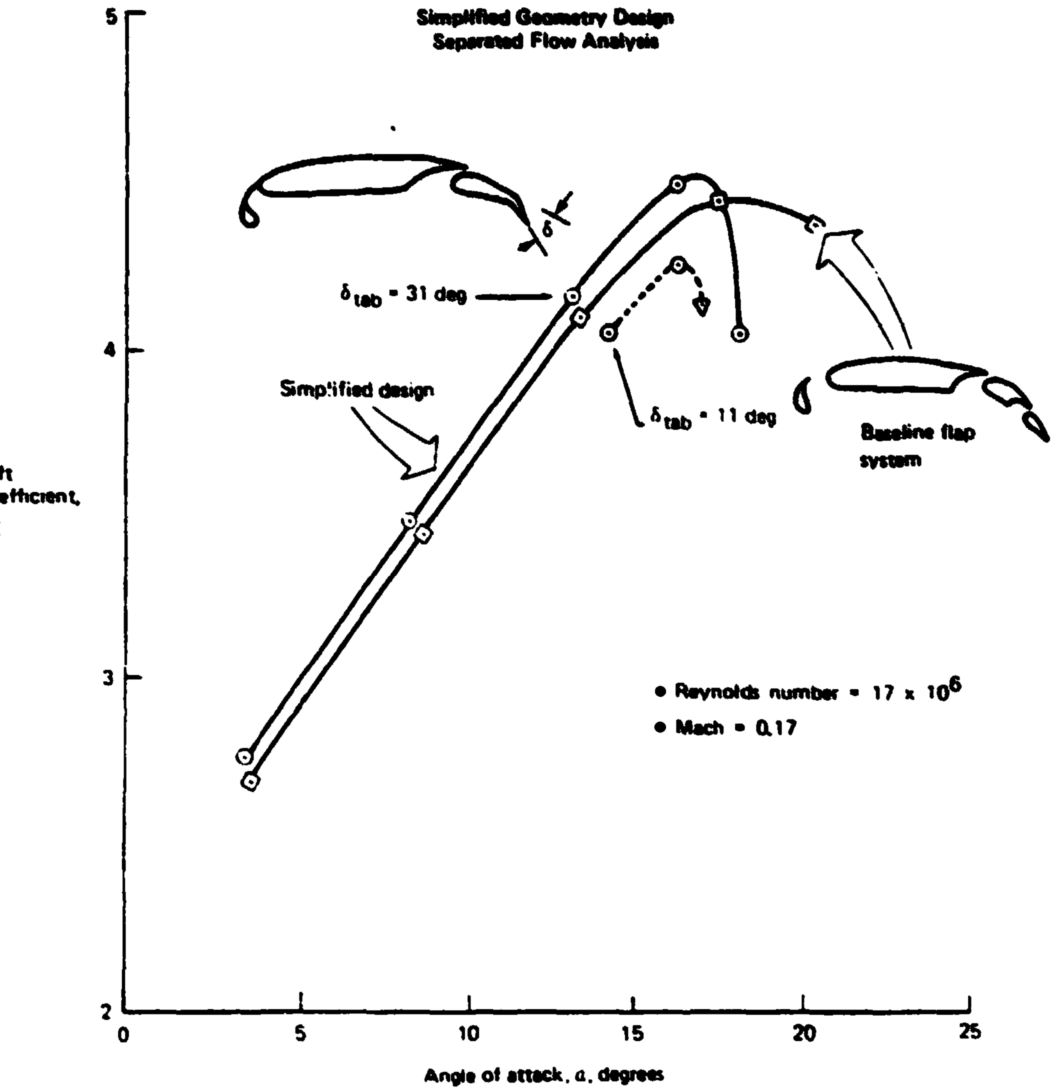

Figure 30. Simplified Design and Baseline Lift Curves

Having chosen the mode of simplification, the design problem reduced to reshaping the elements of this system, where allowed, to maximize design point performance. The following paragraphs describe the decisions and assumptions made in the design of the flap and sealed Krueger.

The starting flap system was the baseline variable-camber Krueger, sealed to the airfoil leading edge, and a single-slotted trailing edge flap having the nested chord of the baseline flaps and the nose shape of the baseline main flap. This flap was deflected until the potential flow lift coefficient at 8-deg angle of attack was the same as that of the baseline.

Analysis of this configuration showed that the required lift coefficient of 3.4 at 8-deg angle of attack could be achieved only at the expense of an unacceptable amount of separation on the flap surface. The tab arrangement shown in figure 29 was employed to achieve the required lift levels at low angles of attack with a controlled amount of separation.

Table 1. Comparison of Configurations 1 Through 5

Configuration	Trailing edge flap description	Leading edge flap description	Advantages	Disadvantages
1	Double-slot	2-position slat (retracted, extended for landing positions)	Simpler leading edge flap than baseline variable-camber Krueger (VCK)	Retains double-slotted trailing edge flaps No takeoff L/D improvement
2	Double-slot	3-position slat (retracted, takeoff, and landing positions)	Substantial L/D improvement for high-altitude airport takeoff (i.e., Denver, La Paz, Mexico City	Retains double-slotted trailing edge flap Leading edge flap only marginally simpler than VCK
3	Single-slot	3-position slat	Substantial L/D improvement Simpler trailing edge flap	Baseline level of $C_{L_{max}}$ not achievable due to limited design freedom in designing slat and wing surface
4	Single-slot	Slotted variable-camber Krueger	Sufficient $C_{L_{max}}$ capability Simpler trailing edge flaps	No takeoff L/D improvement Excessive flap separation in landing configuration Retains complex VCK
5	Single-slot with tab	Sealed variable-camber Krueger	Sufficient $C_{L_{max}}$ capability Improved takeoff L/D at both sea level and high-altitude fields Simpler trailing edge flaps Tab may be used as a control surface both extended and retracted	Retains complex VCK

The pressure distribution on the modifiable portion of the flap system (i.e., the forward surface covered by the airfoil when the flap was retracted) was designed to have as much suction near the trailing edge as was consistent with the requirement that the flap separation be limited to the tab. This was done to maximize the influence of the trailing-edge flaps on stall. Figure 31 displays the resulting flap pressure distribution (with separation modeled) at 12-deg angle of attack.

An analysis of the redesigned trailing-edge flap (with separation modeled) and the starting leading-edge device indicated that the shape of the leading-edge flap was inappropriate for a sealed device and that it allowed the airfoil to stall below the required Cl_{max} of 4.6. A pressure distribution was designed for the Krueger that would maximize Cl_{max} and the required shape was computed. An analysis of this contour showed that Cl_{max} was now somewhat higher than the design requirement. The chord of the new leading-edge device then was judiciously reduced and the shape redesigned in order to trade Cl_{max} for improved L/D and reduced weight. The final shape is shown in figure 29, and the corresponding pressure distributions at 12-, 18-, 20-, and 22-deg angles of attack are shown in figures 32 through 35, respectively.

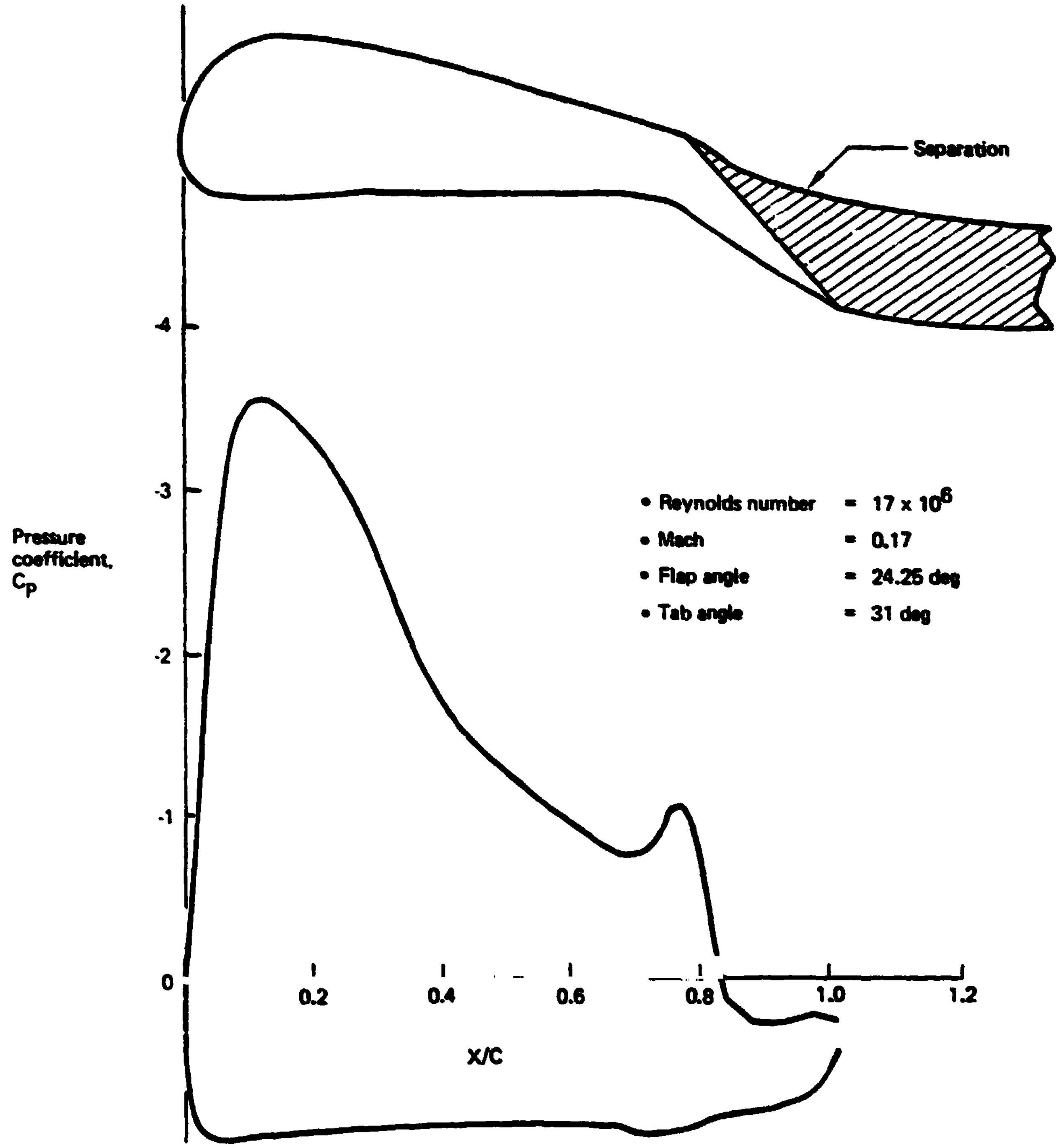

Figure 31. Simplified Trailing Edge Flap Pressure Distribution—Angle of Attack = 12 deg

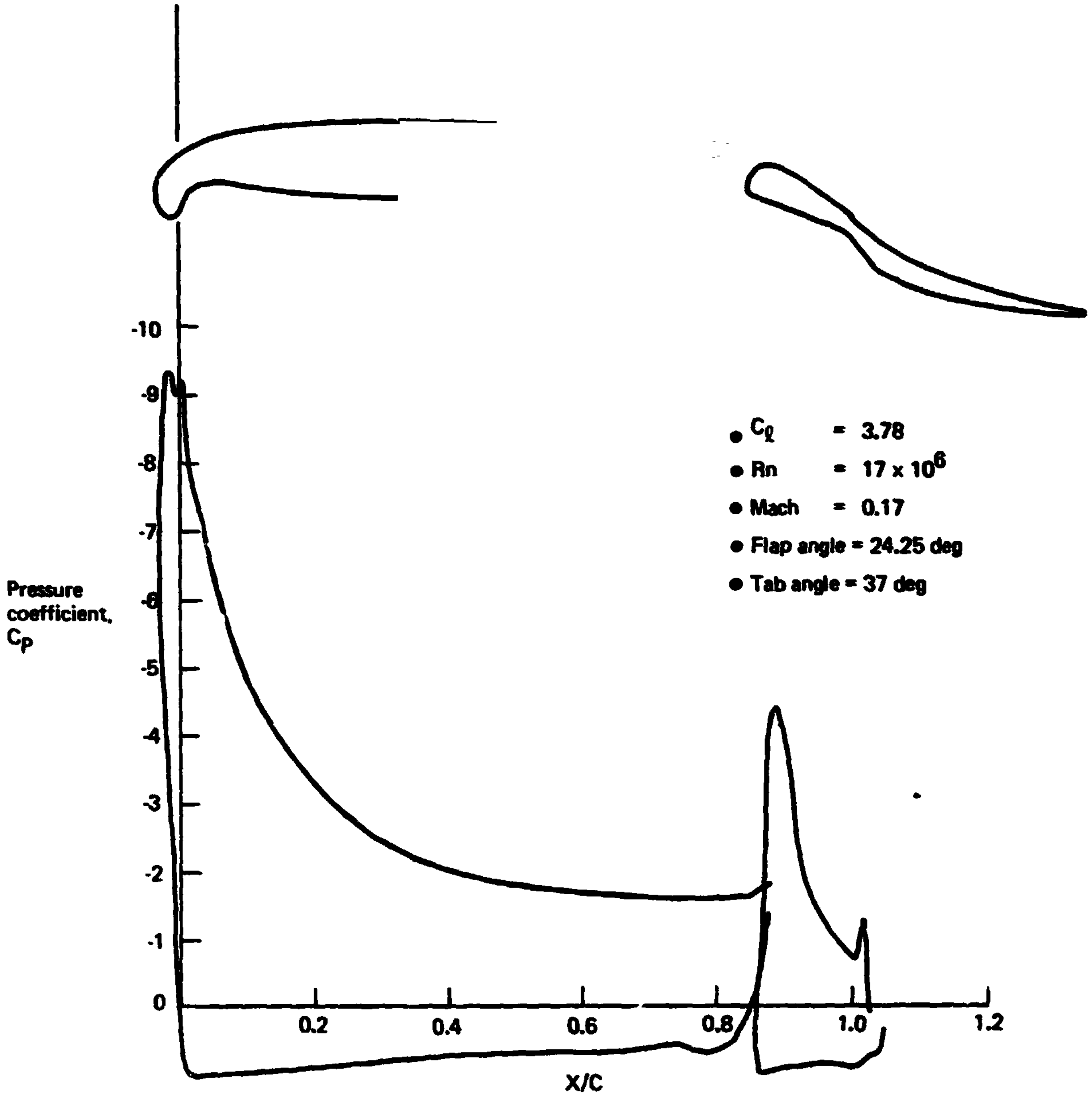

Figure 32. Separated Flow Theory Analysis of the Simplified Design—Angle of Attack = 12 deg

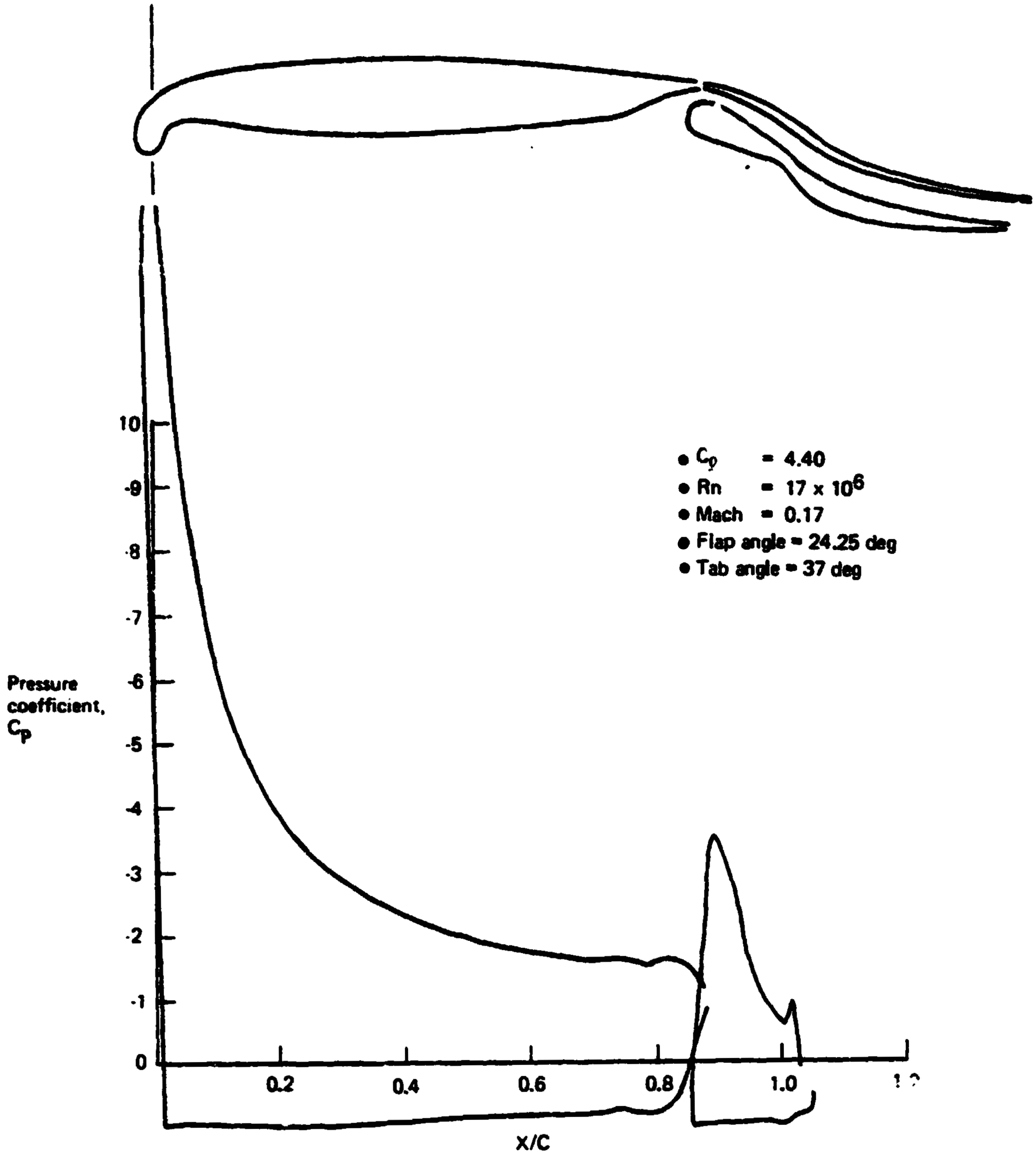

Figure 33. Separated Flow Theory Analysis of the Simplified–Design Angle of Attack = 18 deg

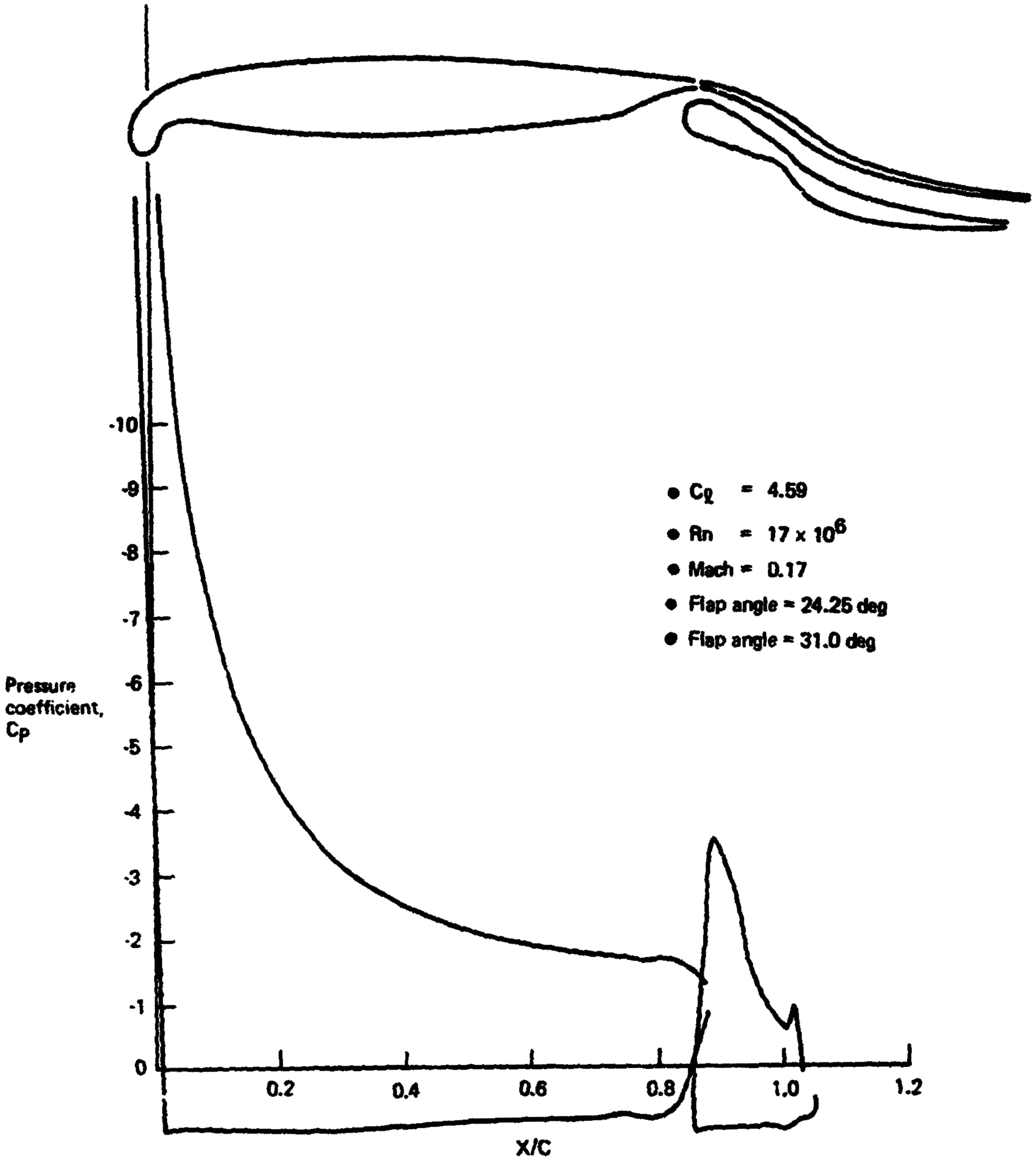

Figure 34. Separated Flow Theory Analysis of the Simplified Design—Angle of Attack = 20 deg

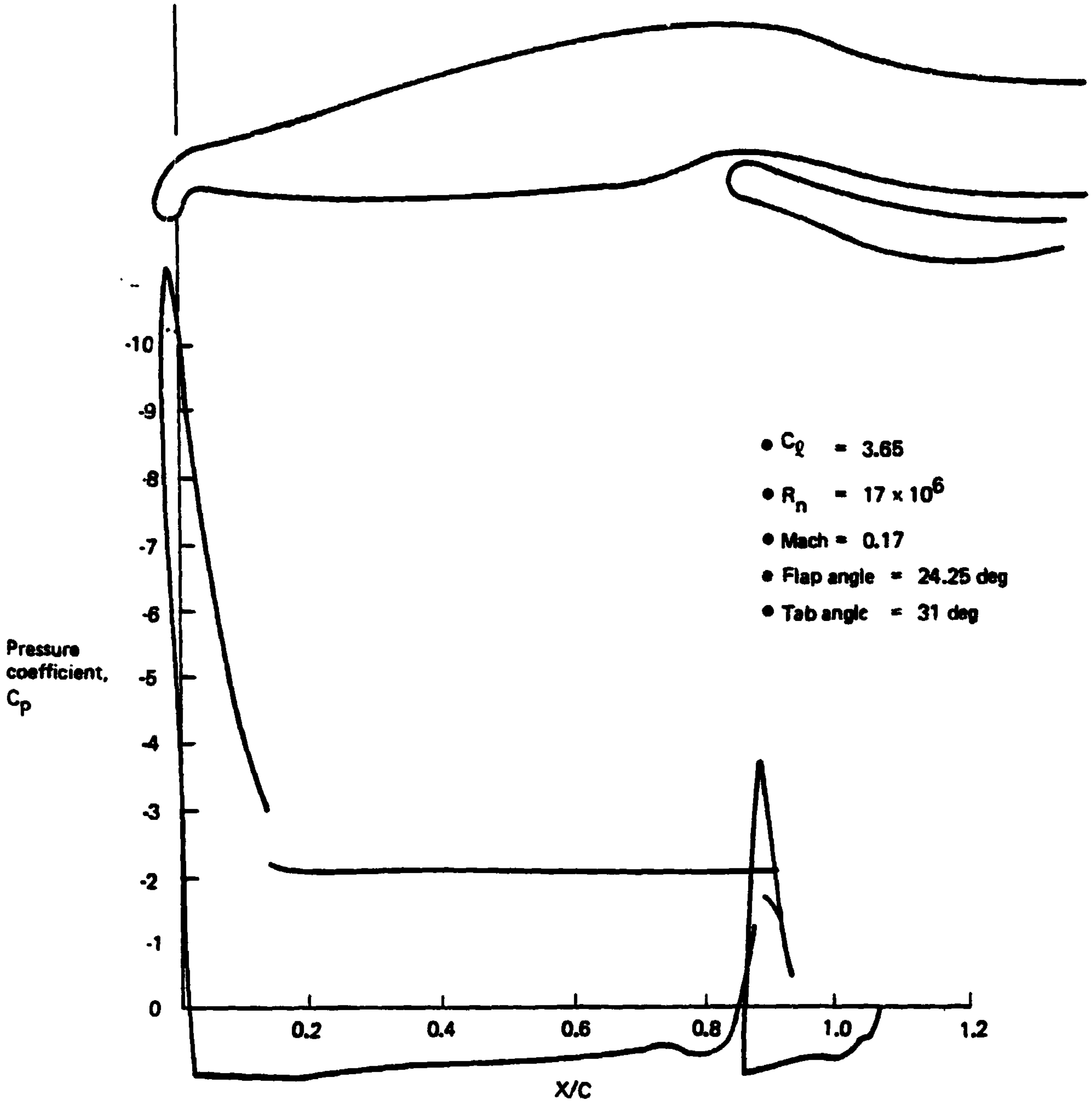

Figure 35. Separated Flow Theory Analysis of the Simplified Design—Angle of Attack = 22 deg

4.2 REQUIREMENTS DEFINITION STUDIES

Requirements definition involved trade studies of a baseline configuration. Key variables were wing planform, assumed flap technology, optimization of climb and descent profiles with and without partial flap deflection, and augmented stability.

4.2.1 Baseline Sizing and Study Ground Rules

The EET high-lift study baseline airplane and its changes due to selected technology concepts are contained in this section. The twin-engined baseline configuration definition and performance are described in the following paragraphs. All of the trade studies used the same configuration concept (illustrated in fig. 6), with changes in wing, empennage, and engine size adjusted to match design constraints for different levels of high-lift characteristics.

The design selection charts contained in this section show results, limits, and requirements pertinent to the trade study. Some of the common performance, airplane size, and nonlimiting constraint lines are deleted for clarity. Figure 36 shows the baseline airplane sizing trends only, not absolute levels. This plot represents a matrix of design point airplane solutions that satisfy the design payload, range, cruise Mach number, and appropriate reserves for a fixed airplane configuration concept. Wing, engine, and empennage size are scaled to meet the fixed payload range requirements. The dependent airplane performance and TOGW are shown as lines of constant values.

Two areas of interest for unconstrained designs are the minimum block fuel and minimum TOGW locations. Selection of an airplane design for minimum energy consumption conflicts with selection of an airplane design for minimum airplane takeoff gross weight for the 196-passenger, 3704-km (2,000-nmi) mission requirements assumed in the trade studies. The minimum TOGW at high wing loadings represent small airplane size (small thrust and small wing areas). However, the minimum block fuel design area is found at low wing loadings (large wings) with 20% larger engines than the minimum TOGW point. Disregarding constraints imposed by takeoff, landing, and altitude capability (engine out and all engines operating), the following relative airplane size effects are found in figure 36:

	Relative	
Design Condition	Block Fuel	TOGW
Minimum block fuel	1.000	1.085
TOFL 2285m (7,500 ft)	1.005	1.035
Minimum TOGW	1.070	1.000

The following data generally refer to relative airplane size within or along the limiting constraint boundaries. Airplanes that do not meet performance objections are not candidate design selection points. The sizing ground rules for the baseline airplane are as follows:

a. Payload = 196 passenger
b. Still air range = 3704 km (2,000 nmi)
c. Long-range cruise design Mach = 0.80

d. Takeoff field length (sea level, 29°C) = 2290m (7,500 ft)
e. V_{APP} (mission landing weight) = 64 m/s (125 Keas)
f. Initial cruise altitude capability = 10 670m (35,000 ft)
g. Engine-out altitude capability = 3660m (12,000 ft)
h. Reserves = ATA domestic
i. Reference wing area based upon trapezoidal definition
j. Constant wing geometry (aspect ratio, sweep angle, airfoil)

The baseline airplane for the EET high-lift studies is defined as follows:

a. Twin-engined model 768-785B
b. Two CF6-50C type engines (scaled)
c. 196 passengers, seven-abreast seating (15/85 mixed class)
d. 5.38m (212 in.) body width
e. Design range = 3704 km (2,000 nmi) in still air
f. Reference area = 232 m^2 (2,500 ft^2)
g. Aspect ratio = 10.24
h. Quarter-chord sweep angle = 0.52 rad (30 deg)
i. Taper ratio = 0.3158
j. Outboard thickness-to-chord ratio = 0.103

Model 768-785B is the reference-sized airplane for the EET high-lift studies. The engines are scaled CF6-50C's, sized to meet the above constraints. This is consistent with a current conventional technology level that is also reflected in the aerodynamic data. Tail sizing and control system definitions are conventional with no dependence on advanced stability augmentation. Sized airplane characteristics and performance are summarized in table 2.

The design selection chart, Thumbprint, is shown in figure 36, with the design point and limiting criteria identified. The design point is located on the 2290-m (7,500-ft) takeoff field length line at a wing loading of 513 kg/m^2 (105 lb/ft^2), which is very near the minimum block fuel point. The block fuel and takeoff gross weight (TOGW) lines are used as trend data and not for absolute levels. The design point has a margin of 445m (1,460 ft) over the requirement for an initial cruise altitude capability (ICAC) of 10 670m (35,000 ft). The 62-m/s (120-kn) landing approach speed is below the desirable maximum of 64 m/s (125 kn).

Wing loading could be allowed to increase up to a value of 560 kg/m^2 (114 lb/ft^2) without exceeding a mission landing weight approach speed of 64 m/s (125 kn), but block fuel would then increase by about 2.5%. The design point is the best compromise between the minimum TOGW and block fuel points and has the minimum DOC for the 2290-m (7,500-ft) field length (as shown in fig. 47). The baseline airplane was found to be insensitive to landing $C_{l_{max}}$ improvements due to the low wing loading required to satisfy sea-level takeoff and enroute engine-out altitude requirements while minimizing block fuel, TOGW, and DOC.

The baseline airplane performance was found to be most sensitive to improvements in takeoff lift-to-drag ratio (L/D), particularly at the low lift coefficient levels typical of takeoff out of high, hot airfields (e.g., Denver).

The general arrangement of the 768-785B is shown in figure 37.

Table 2. Sized EET Airplane Performance and Characteristics (Model 768-785B)

Mission Requirements

Still air range = 3704 km (2000 nmi)
Payload = 196 passengers, 18 225 kg (40 180 lb)
Initial cruise altitude ≥ 10 668m (35 000 ft)
Cruise Mach number = 0.80
Takeoff field length ≤ 2290m (7500 ft)
Approach speed ≤ 231.5 km/h (125 kn)
Reserves = 1967 ATA domestic

Airplane size and geometry characteristics	
Wing area	235.51 m^2 (2535.0 ft^2)
Wing span	49.11m (161.12 ft)
MAC	5.23m (17.15 ft)
Aspect ratio	10.24
$Sweep_{c/4}$	0.52 rad (30 deg)
Taper ratio	0.3158
t/c, SOB/tip*	15%/10.3%
Horizontal tail area	51.65 m^2 (556.0 ft^2)
Vertical tail area	36.14 m^2 (389.0 ft^2)
Body length	47.55m (156.0 ft)
Body diameter	5.39m (17.67 ft)
Engines	2 scaled CF6-50C
Bypass ratio	4.4
Sea level static thrust (uninstalled)	164.27 kN (36 930 lb)

*Based on gross chord length

Airplane performance	
Takeoff gross weight	120 719 kg (266 140 lb)
Operating empty weight	76 861 (169 450)
Block fuel	19 061 (42 000)
Reserves	6827 (15 050)
Mission landing weight	101 913 (224 680)
Thrust/weight	2.726 N/kg (0.278 lb/lb)
Wing loading	512.67 kg/m^2 (105.0 lb/ft^2)
Initial cruise altitude capability	11 113m (36 460 ft)
Average cruise altitude	11 723m (38 460 ft)
Range factor	22 909m (12 370 nam)
Lift/drag	18.2
Specific fuel constant	0.069 kg/hr/N (0.674 lb/hr/lb)
$C_{D_{P_{MIN}}}$	0.01791
FAR TOFL, SL, 29°C (84°F)	2290m (7500 ft)
$C_{L_{V_2}}$	1.506
V_{APP} (1.3 V_s)	222 km/h (120 kn)
$C_{L_{APP}}$	1.81

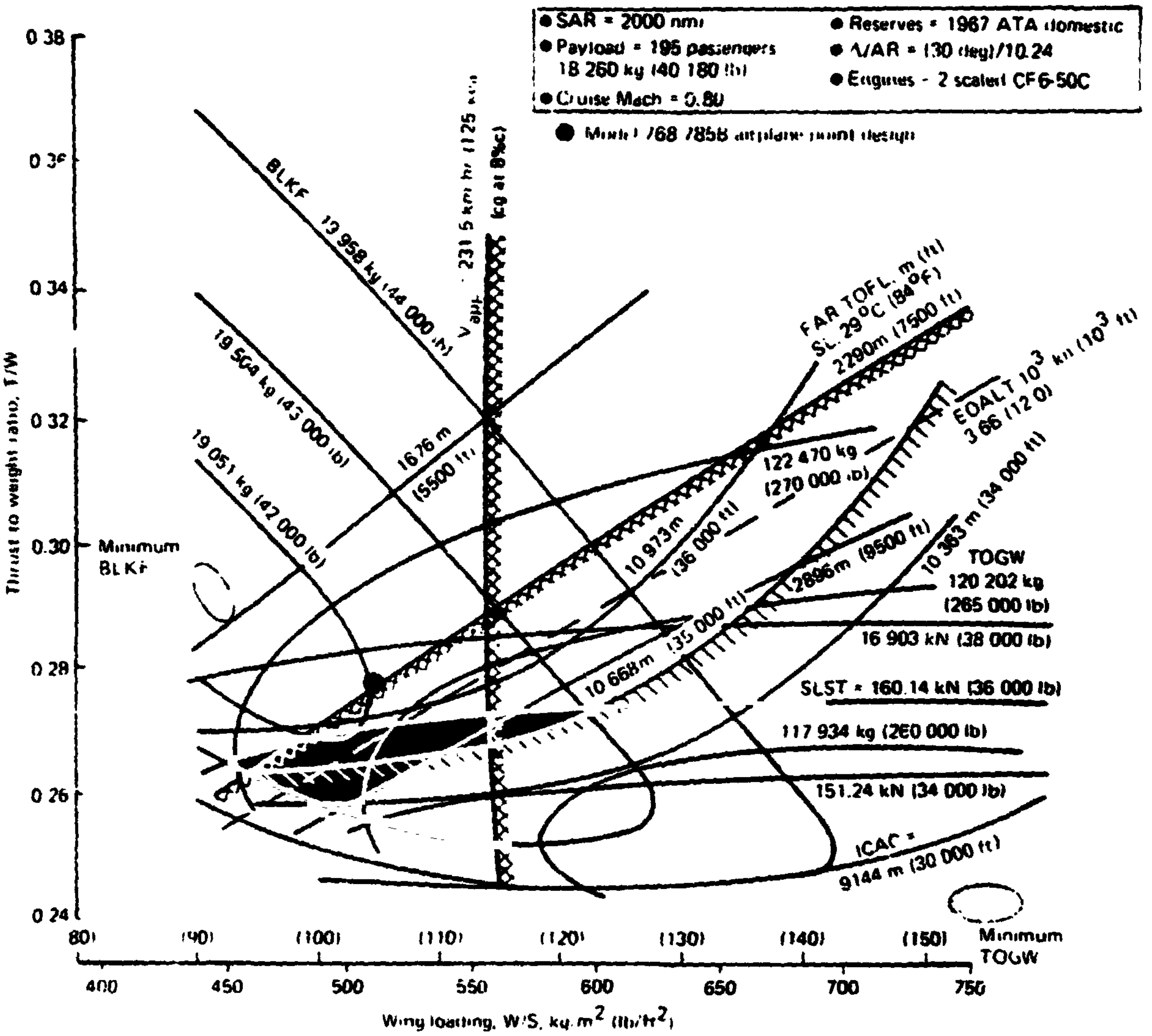

Figure 36. Design Selection Chart for Reference Airplane, 768-785B

4.2.2 Planform Trade Studies

The wing planform trade studies included variations in both wing aspect ratio and percent of wing chord occupied by high-lift devices.

Wing Aspect Ratio Trade Study

A previous Contractor study of aspect ratio effects was done under ground rules similar to those for the baseline reference airplane of this study. Because that study had much greater technical depth than was possible under the current study level of effort, it was decided to utilize the results of the previous study, rather than to repeat it at a lower technological depth. The mission ground rules of the previous study were as follows:

a. Payload = 201 mixed-class passengers

b. Range = 3230 km (1,745 nmi).

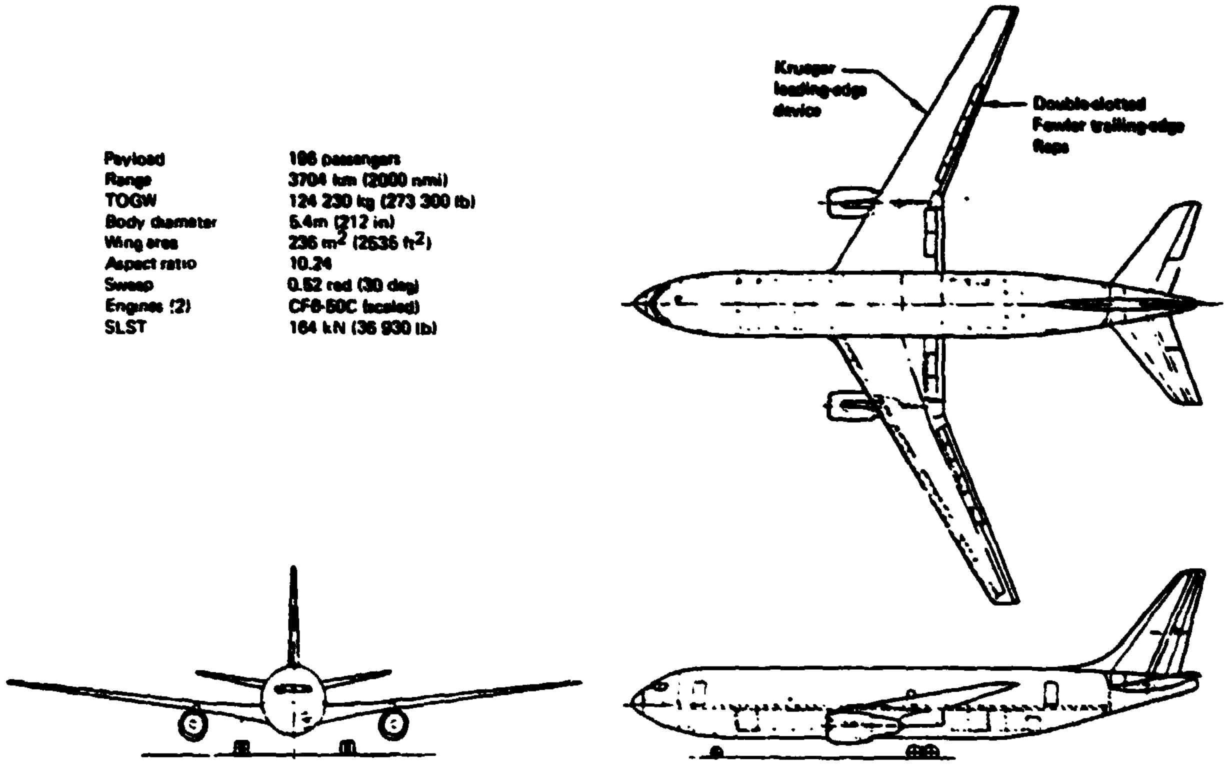
Krueger leading-edge device
Double-slotted Fowler trailing-edge flaps

Payload	196 passengers
Range	3704 km (2000 nmi)
TOGW	124 230 kg (273 300 lb)
Body diameter	5.4m (212 in)
Wing area	236 m^2 (2536 ft^2)
Aspect ratio	10.24
Sweep	0.52 rad (30 deg)
Engines (2)	CF6-50C (scaled)
SLST	164 kN (36 930 lb)

Figure 37. Baseline Airplane (Model 768-785)

c. Wing loading = 572 kg/m^2 (117 lb/ft^2)

d. Design cruise speed = 0.78 Mach and 0.82 Mach

e. Initial cruise altitude capability = 10 060m (33,000 ft) at design speed and initial cruise weight

f. Takeoff field length $\leqslant$ 2290m (7,500 ft), sea level, 29°C (84°F)

g. Approach speed $\leqslant$ 70 m/s (135 kn) at maximum landing weight

h. Reserve fuel = ATA domestic

This study provided aspect ratio trend information compatible with the rest of the high-lift studies. Aspect ratio trends are shown in figure 38. At either cruise Mach number, the choice of aspect ratio has a significant influence on fuel economy and engine size required for the design mission. Within the range of wing geometries studied, both takeoff gross weight and operating weight increase with aspect ratio, while block fuel and engine size decrease.

A comparison of fuel savings with the corresponding operating weight penalty, as aspect ratio increases, is illustrated in figure 39 for the Mach 0.78 planforms. Within the aspect ratio range from 8 to 11, approximately 3 lb of OEW (operating empty weight) are required to save 1 lb of fuel.

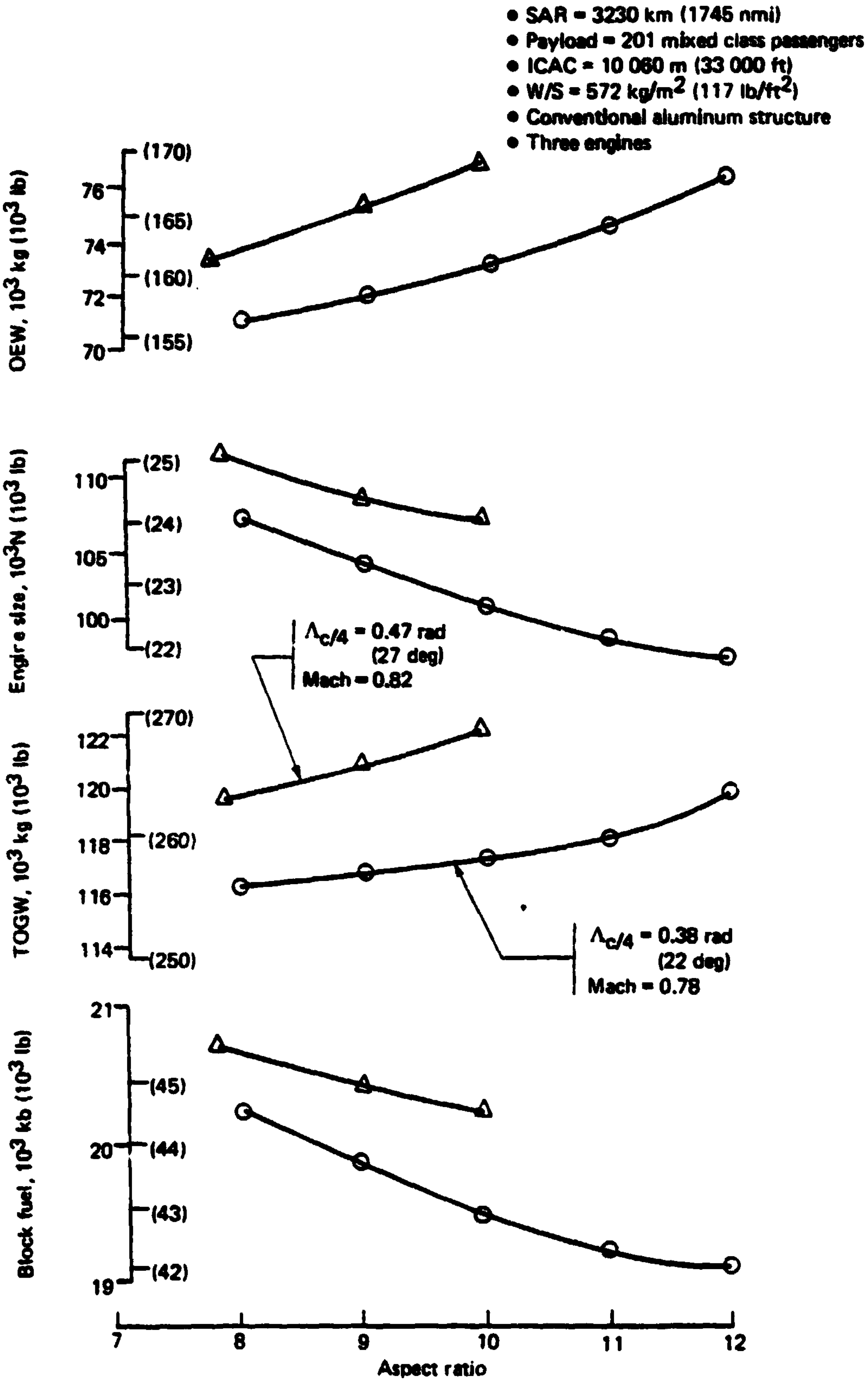

- SAR = 3230 km (1745 nmi)
- Payload = 201 mixed class passengers
- ICAC = 10 060 m (33 000 ft)
- W/S = 572 kg/m^2 (117 lb/ft^2)
- Conventional aluminum structure
- Three engines

Figure 38. Cruise Mach/Wing Planform Trades

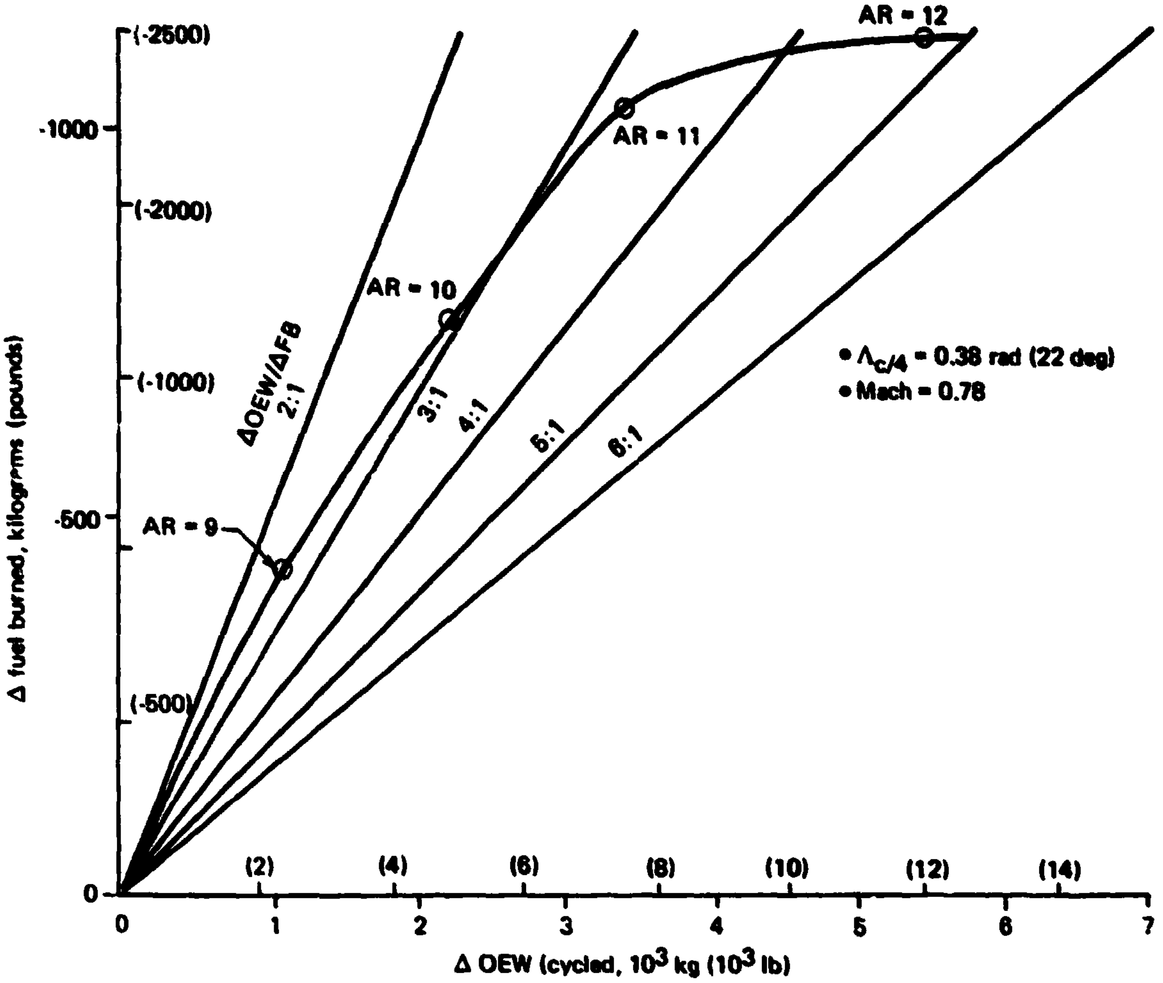

Figure 39. Fuel/OEW Trade (Conventional Aluminum Structure)

As either aspect ratio or sweep are increased, the additional span increases the root bending moments, and hence the wing box weight increases. Elastic problems also increase, requiring additional jig twist (tip wash-in) to maintain the desired "1-g" cruise loading and causing a loss in wing stability due to flexibility.

Flutter analyses show that additional torsional stiffness is required to meet the 1.2 V_D (dive speed) criterion for aspect ratios of 9 and above. Figure 40 shows the results of the wing flutter study.

As shown in figure 41, direct operating cost tends to increase with increasing aspect ratio. and increasing speed, especially if airplane price is varied as a function of airframe weight and engine size. These data were calculated using a Boeing-modified ATA cost equation.

An aspect ratio of about 10 was chosen as a good compromise between fuel economy, engine size, airplane weight, and flutter risk.

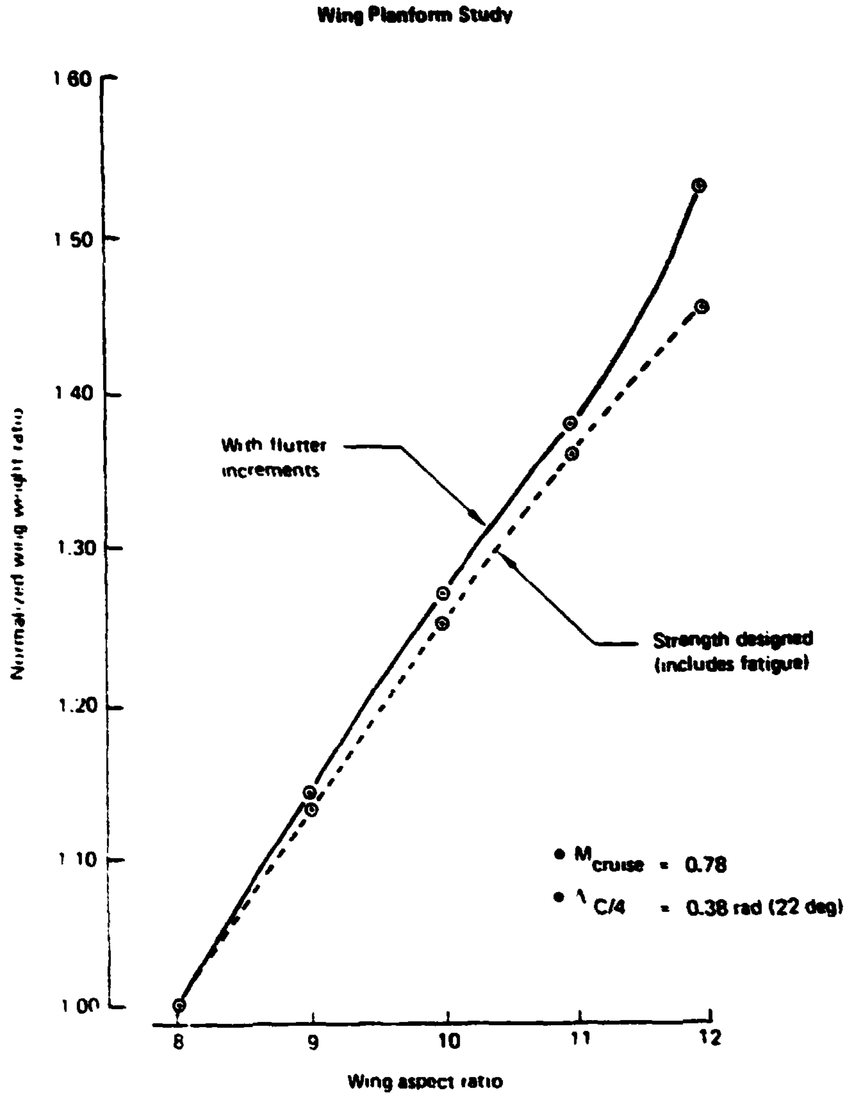

Figure 40. Normalized Wing Weight Versus Aspect Ratio (Conventional Aluminum Structure)

Flap Chord Trade Study

In the study of performance effects of varying leading- and trailing-edge flap sizes, flap size was varied by changing the percentage of flap chord on the wing, relative to the reference configuration. The range and combinations of flap sizes studied are shown in table 3.

The effects of flap chord variations on low-speed envelope performance are shown in figures 42 and 43. The lift and drag characteristics for the flap chord study were derived from empirical corrections to wind tunnel models with similar geometry. Note that flap

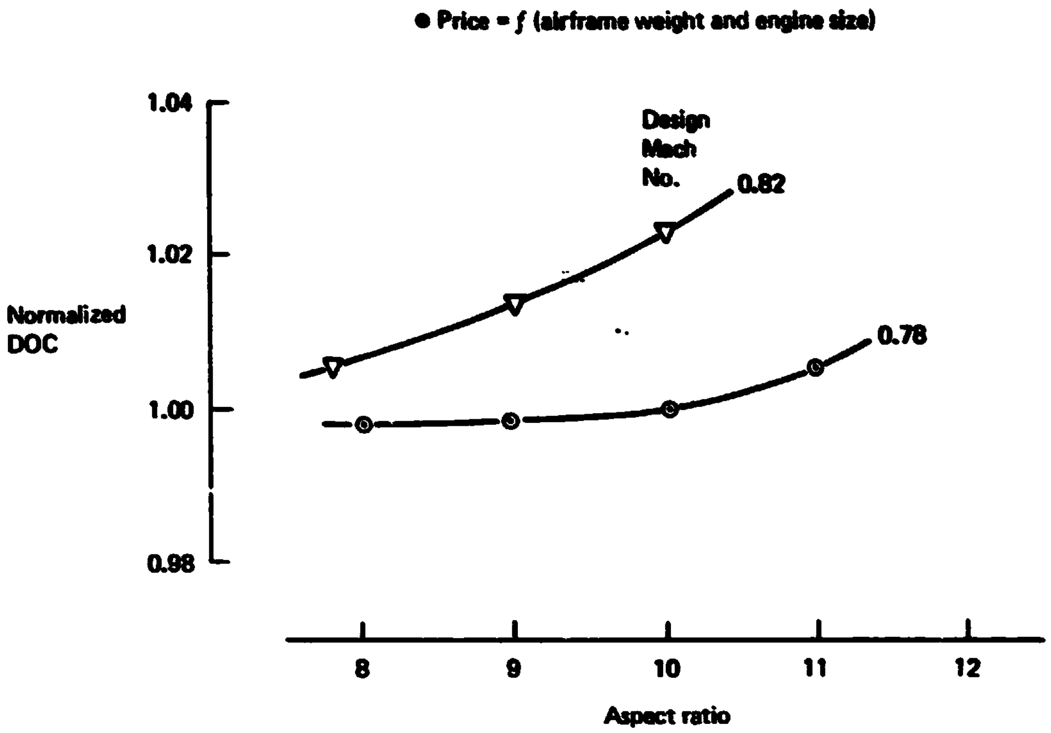

Figure 41. Economic Comparison With DOC at 1852 km (1000 nmi)

Table 3. Flap Chord Sizes

Trailing edge C_{flap}/C_{wing} ↓	Leading edge C_{flap}/C_{wing} →		
	0.06	0.11	0.[illegible]
0.17		X	
0.22		X EET baseline (768-785B)	
0.27	X	X	X

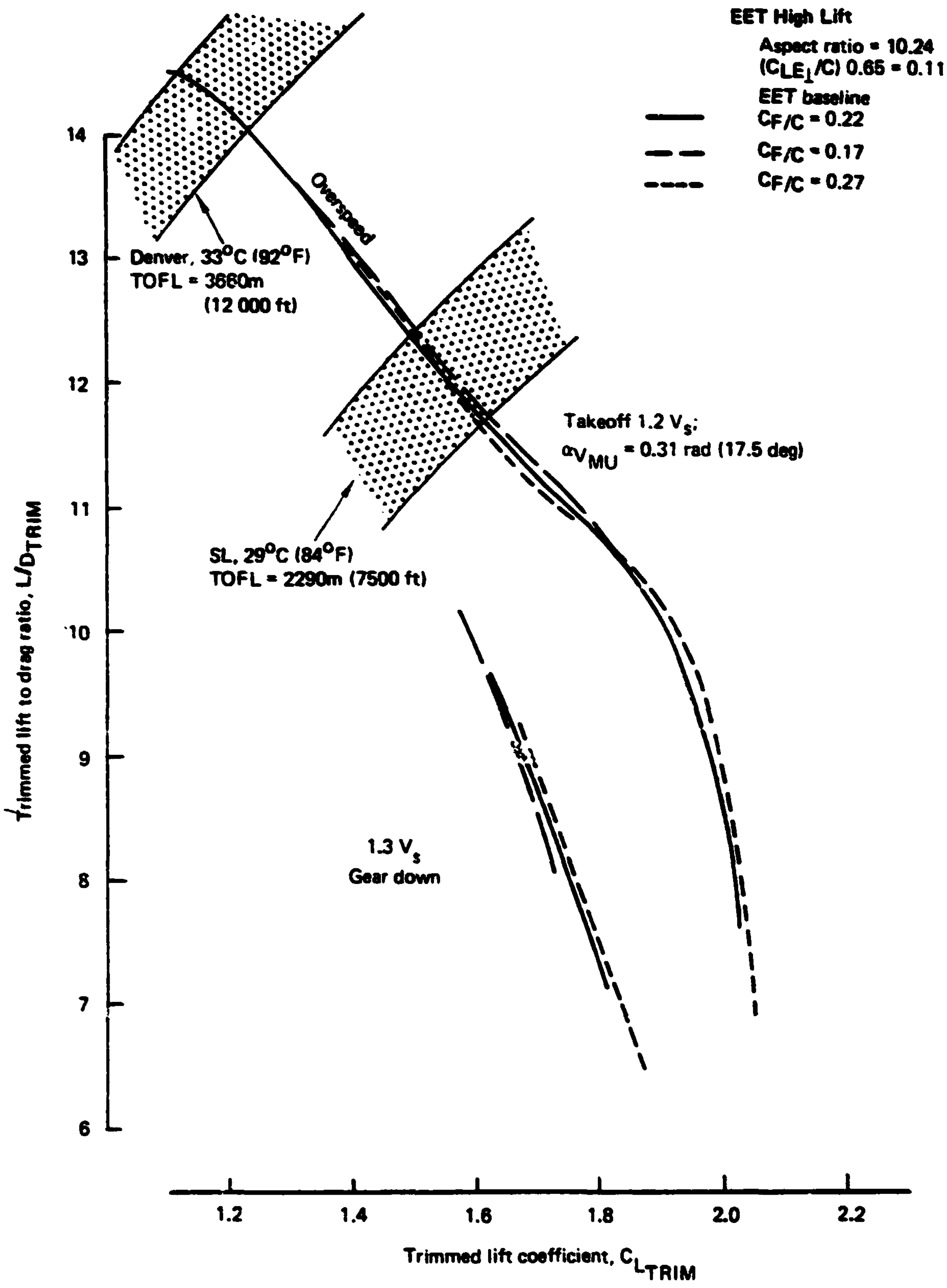

Figure 42. Effect of Trailing Edge Flap Chord

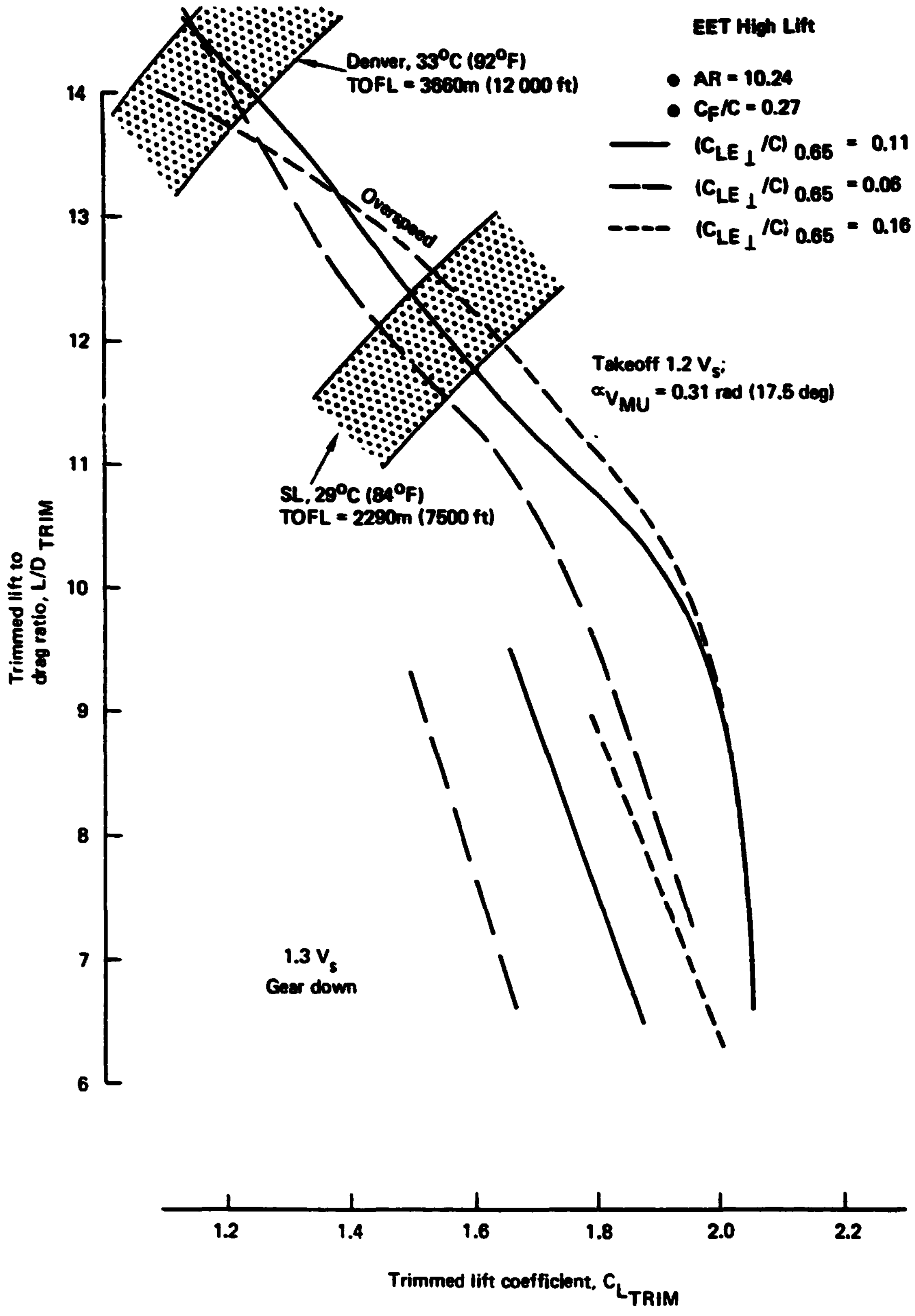

Figure 43. Effect of Leading Edge Flap Chord

chords were varied $\pm 5\%$ from the reference baseline size and that leading-edge flap chord effects were studied only in combination with the largest of the trailing-edge flaps. The envelope performance is based upon either minimum unstick speed or 1.2 times stall speed, whichever was limiting. At low lift coefficient, "overspeed" (i.e., a velocity higher than 1.2 V_s) with the lowest flap deflection angle is used. The lift-to-drag ratio envelopes shown in figure 42 are nearly identical, indicating that takeoff performance is insensitive to $\pm 5\%$ change in trailing-edge flap chord.

The relative performance of each flap size is illustrated on the design selection chart (fig. 44). Wing loadings at which the desired approach speed can be attained are shown for each flap size. Approach lift coefficient is improved by increasing trailing-edge flap chord, but approach speed objectives are met with even the smallest trailing-edge flaps studied. When the trailing-edge flap was changed, only small changes in wing loadings and thrust-to-weight ratios were required to meet the 2290-m (7,500-ft) takeoff field length constraint. A change in trailing-edge flap chord of $\pm 5\%$ results in essentially no change in sea-level takeoff performance. Takeoff performance is affected by leading-edge flap chord changes. The 16% leading-edge flap chord has worse takeoff performance than the baseline 11% flap chord at low values of C_{LV2}.

The 11% and 6% leading-edge flap chords have about the same off-design performance (i.e., high-altitude, hot-day takeoffs). The 11% leading-edge flap chord is required to meet the approach speed criterion of 64 m/s (125 Keas) when used with the 17% trailing-edge flap chord (see fig. 44).

With minimum block fuel as a primary requirement, the simplification offered by slightly smaller trailing-edge flaps appears to be a desirable choice. The wing loading sensitivities for airplanes sized to fixed P/L, SAR, and TOFL, shown in figure 45, illustrate the merit of reducing trailing-edge flap chord from 22% (baseline) to 17%. Both TOGW and block fuel are reduced by small amounts, less than 1/2%. The minimum in block fuel at a wing loading of 500 kg/m^2 (102.5 lb/ft^2) on the 2290-m (7,500-ft) TOFL design constraint line is, in general, the result of two opposing airplane cruise factors. These two factors are maximum lift-to-drag ratio (L/D), which increases for decreasing wing loading (larger wings), and OEW, which decreases with increasing wing loading (smaller wings). An additional effect on the L/D factor is the change in initial cruise performance match when engines are sized for TOFL length and not for cruise range factor. Figure 45 for a fixed field length shows that as wing loading is decreased, engine size is reduced, which lowers initial cruise altitude. This results in a lower cruise L/D, while wing area and OEW become larger. Increasing wing loading reduces maximum L/D, which offsets the airplane weight benefit and results in higher fuel usage. The change in trailing-edge flap chord results in a shift in level with nearly the same characteristic, since the low-speed polar envelope is similar and the change in weight is small. The smaller trailing-edge flap chord reduces TOGW and block fuel less than 1/2%.

4.2.3 Flap Technology Trade Studies

Three levels of advanced flap technology have been studied for application to the reference twin-engined airplane. Performance studies were conducted for the baseline mission ground rules sea level, 2290-m (7,500-ft) TOFL, etc., and for high-altitude, hot-day performance [2870 km (1,550 nmi), 3660-m (12,000-ft) TOFL, 1625-m (5,332-ft) altitude, 33°C (92°F)]. The engine-out enroute climb altitude capability, 3660m (12,000 ft), at design payload and range is an additional design consideration.

- SAR = 3704 km (2000 nmi)
- Payload = 196 passengers (40 180 lb)
- Cruise Mach = 0.80
- Reserves = ATA domestic
- Λ/AR = 30 deg/10.24
- Engines = 2 scaled CF6-50C

$(C_F/C\ LE/C_F/C\ TE) = (0.XX/0.XX)$

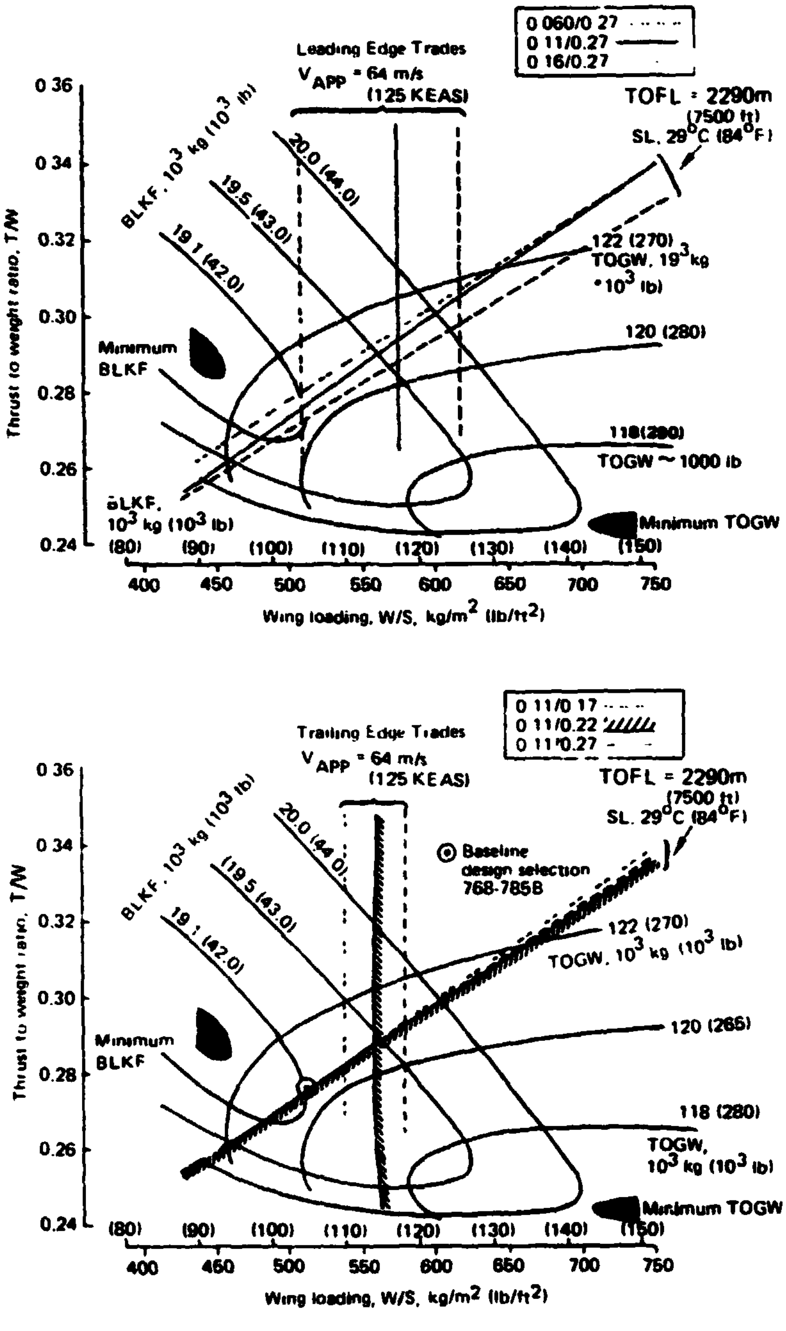

Note: These design selection charts show only low-speed drag polar effects (i.e., no flap weight changes)

Figure 44. Effects of Varying Flap Chord on Low-Speed Sizing Constraints (Model 768-785B)

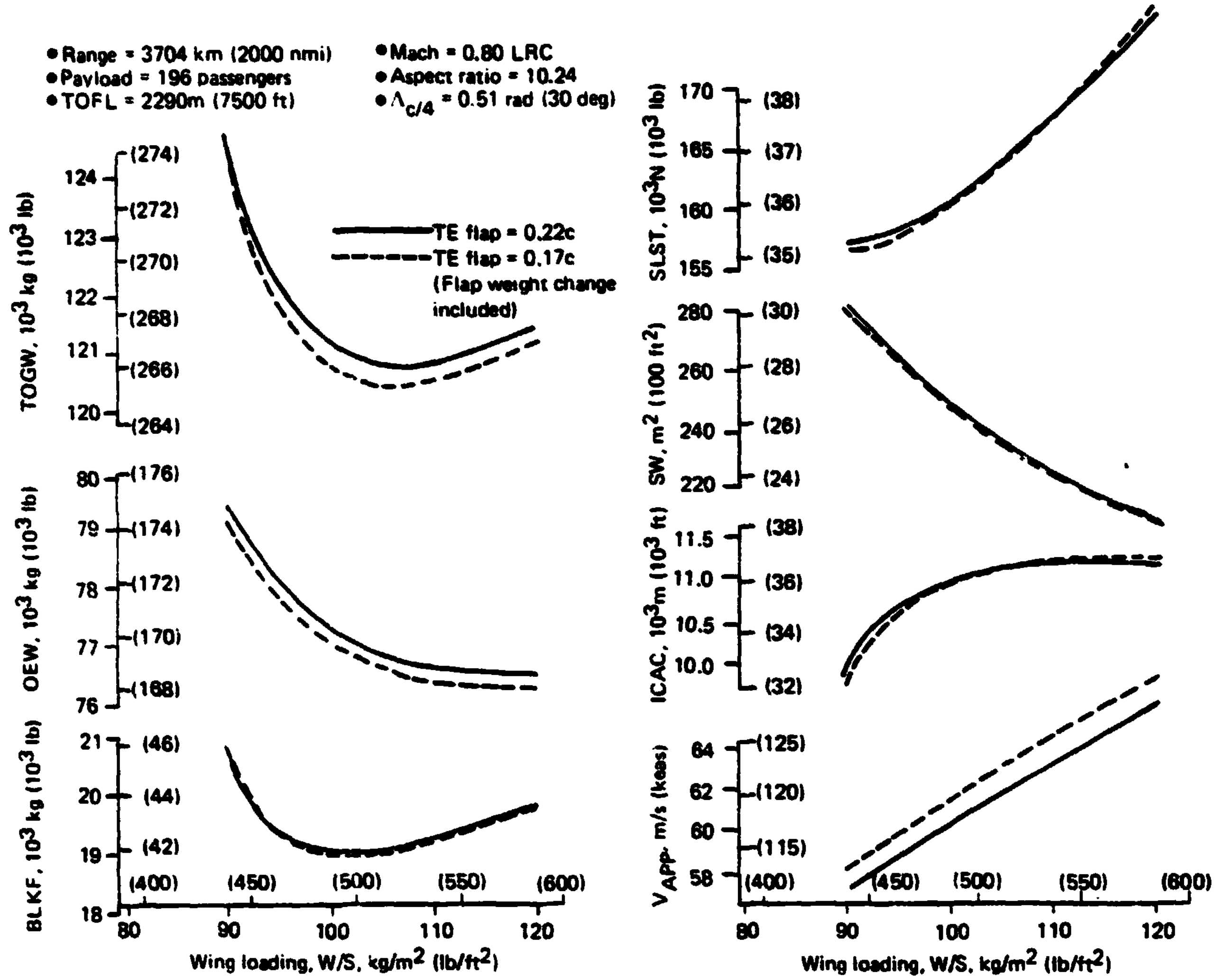

Figure 45. Trailing Edge Flap Chord Trade (0.22c Versus 0.17c)

The flap configuration definitions are as follows:

Baseline	Leading-edge device is a two-position, variable-camber Krueger. Trailing-edge flaps are double-slotted.
System A	Leading-edge device is a three-position, variable-camber Krueger (sealed takeoff, slotted approach). Trailing-edge flaps are the same as the baseline.
System B	Leading-edge device is a three-position, variable-camber Krueger redesigned for maximum $C_{l_{max}}$ at flight Reynolds number. Trailing-edge device is a double-slotted device redesigned for the same goal as the leading-edge device.
System C	Leading-edge device is a two-position, variable-camber Krueger designed for maximum L/D at flight Reynolds number (constrained to

have the same Cl_{max} at approach as the baseline). Trailing-edge flap is a single-slotted device with trailing-edge tab, designed for maximum L/D at flight Reynolds number.

Because the design applications subtask was begun at the same time as the requirements definition subtask, no detailed analyses of flap systems A, B, and C were available when requirements definition was begun; consequently, it was necessary to make preliminary estimates of the aerodynamic performance of these alternative systems for the work to proceed.

The estimated aerodynamic performance characteristics of each flap system are summarized in figure 46. The impact of sizing to meet takeoff requirements at a high-altitude airport on a hot day is important; Mexico City and Denver are two examples, and the latter was chosen for this study. The ranges of design lift coefficients required at Denver and sea level are illustrated, along with the relative lift-to-drag ratios of the flap systems for both design conditions.

The design selection chart (fig. 47) illustrates the configuration and performance effects of the alternative flap systems. The minimum-TOGW airplane is at a wing loading of 757 kg/m^2 (155 lb/ft^2), with minimum direct operating cost shown at a wing loading of 680 kg/m^2 (140 lb/ft^2); both are well beyond the takeoff and landing speed constraint lines. Minimum block fuel occurs at a wing loading of 440 kg/m^2 (90 lb/ft^2), which is within the performance constraint boundaries of takeoff field length, approach speed, and initial cruise altitude, and has good growth potential and buffet margins. However, design selections must also consider direct operating cost within TOFL constraints (either Denver or sea level).

The data shown in table 4 compare airplanes selected for minimum DOC, constrained by the sea-level and Denver TOFL performance requirements. None of the airplanes are limited by approach speed (i.e., $C_{L_{APP}}$). Although not shown in the table, airplanes sized by sea-level TOFL using flaps A, B, or C have a similar DOC improvement, relative to the base system. However, these airplanes do not have adequate enroute engine-out altitude capability and therefore cannot show a DOC advantage with the improved flap systems.

Because a higher approach lift coefficient capability is not required, flap system C with design for maximum L/D and the simpler, single-slotted trailing-edge flap was preferred. Further improvements in L/D at low lift coefficients should be investigated to improve Denver performance.

4.2.4 Climb and Descent Studies

The basic ground rules for climb and descent optimization studies were as follows:

a. 196 passengers
b. 3704 km (2,000 mi) still air range
c. Cruise Mach = 0.80
d. Constant altitude cruise at 10 670m (35,000 ft)
e. OEW = 76 860 kg (169,450 lb)

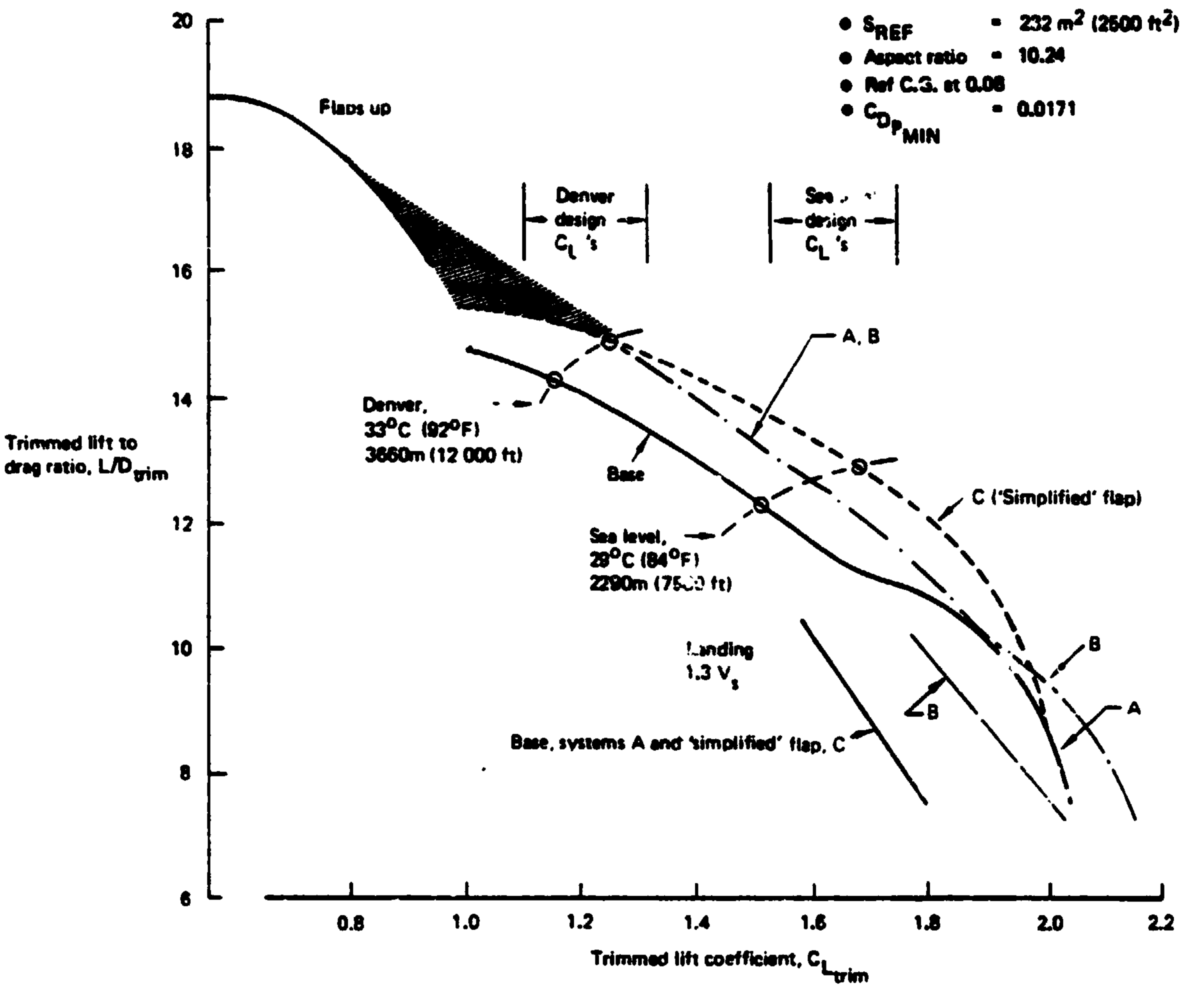

Figure 46. 'Simplified' Flap Envelope

Common climb and descent speed schedules were varied to seek possible reduction of mission fuel. The resulting effects on block fuel and block time relative to the base schedule (250 kcas/300 kcas/0.75 Mach number) are shown in figure 48. Changing to a speed schedule of 144 m/s (280 kcas) and 0.7 Mach number for the standard mission would save about 104 kg (230 lb) (0.5%) of fuel at an expense of about 2.5 min (0.9%) in block time. However, previous studies of climb and descent speeds for similar aircraft indicate that DOC would increase slightly at this lower climb speed. A slightly faster climb and descent speed schedule of 154 m/s (300 kcas), 0.8 Mach number produces minimum DOC at a small increase in block fuel.

The data shown in figure 49 indicate no advantage to climbing at a lower speed with partial trailing-edge flaps deployed. The clean wing and the partial trailing-edge flap polars cross at a lift coefficient that represents a speed too slow for best climb efficiency and very near stall.

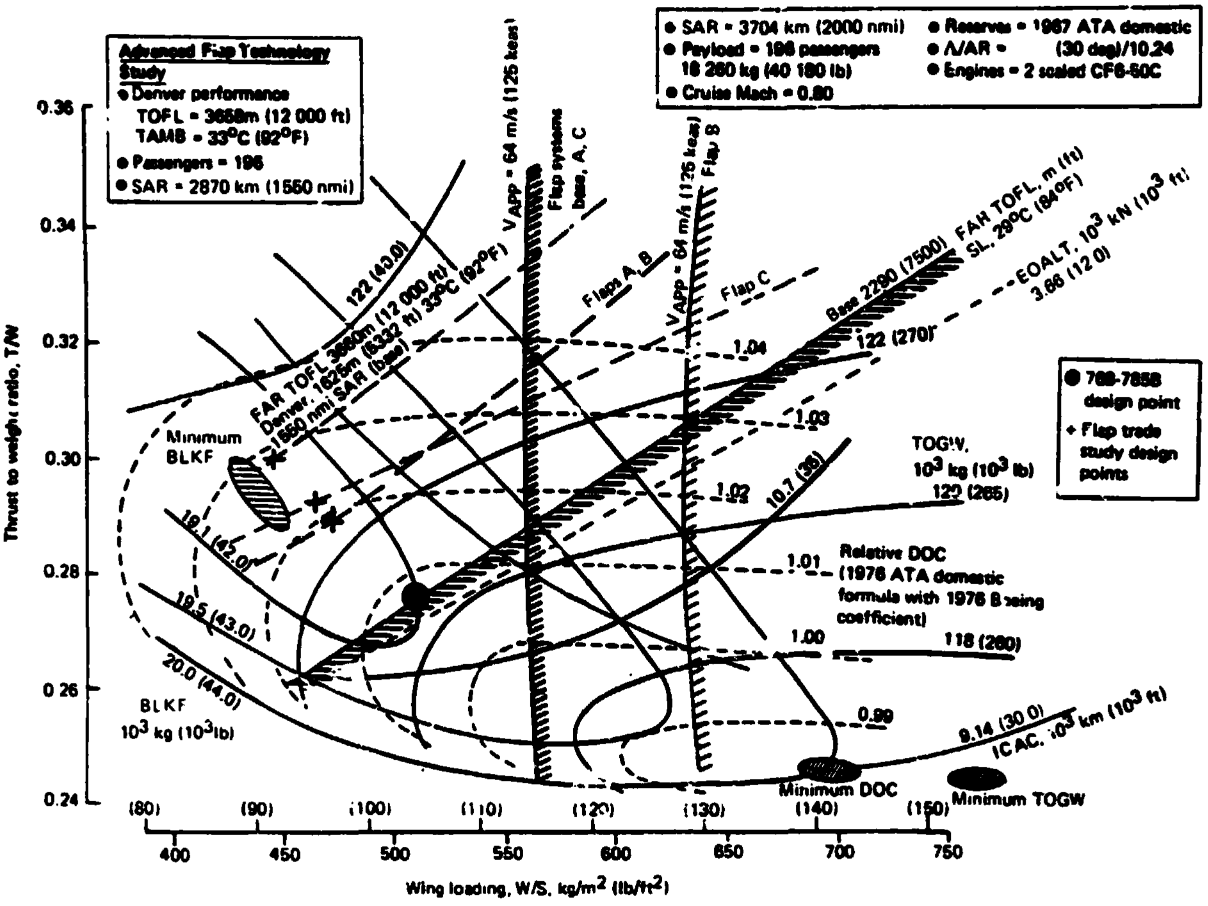

Figure 47. EET Baseline Design Selection Chart

Overall climb and descent fuel efficiency can be improved slightly with moderate changes in climb speed lift-to-drag ratios. However, since excess thrust is the driving force for climb capability, reductions in drag during climb yield a smaller reduction in thrust required (and therefore fuel flow) for the same rate of climb. Also, maintaining maximum climb power results in a lower rate of climb improvement than the percent change in climb used during the early stages of ascent (i.e., under 6100m (20,000 ft) and 25% of the distance required to climb to cruise altitude). The lower overall energy efficiency of the turbofan engine at low speeds, combined with the high excess power required to climb and accelerate from the low energy state at sea level to cruise conditions, allows only very small improvements in climb fuel (approximately 1%) for substantial increases in climb lift-to-drag ratios (approximately 5 to 10%).

Based upon these data, the baseline airplane climb speed schedule of 154 m/s (300 kcas), 0.75 Mach number, and the baseline flap procedures were retained.

Table 4. EET Twin Advanced Flap Study Size and Performance Comparison

- 196 passengers
- 0.80 cruise Mach
- 3704 km (2000 nmi) SAR
- 2 scaled CF6-50C engines

Design condition	Flap system	Thrust to weight ratio, T/W	Wing loading, W/S, kg/m² (lb/ft²)	Maximum TOGW, 10³ kg (10³ lb)	Engine size, SLST, kN (10³ lb)	Wing area (trap) m² (ft²)	Relative DOC*	Relative fuel burned	ICAC, m (ft)	V_{APP}, m/s (keas)
Sized for SL TOFL, 2290m (7500 ft), 28.9°C (84°F) minimum DOC	Base	0.278	512.6 (105.0)	121 (266.1)	16.4 (36.9)	236.8 (2535)	Base	Base	11 130 (36 500)	61.9 (120.2)
Sized for Denver range 2870 km (1550 nmi), 33°C (92°F)	Base	0.301	447.2 (91.6)	125 (275.7)	18.4 (41.4)	279.0 (3000)	+2.1%	-0.5%	11 890 (39 000)	59.0 (114.7)
	A	0.292	473.1 (96.6)	123 (271.2)	17.6 (39.6)	261.3 (2810)	+1.2%	-0.3%	11 580 (38 000)	56.5 (116.5)
	B	0.292	473.1 (96.6)	123 (271.2)	17.6 (39.6)	261.3 (2810)	+1.2%	-0.3%	11 580 (38 000)	56.2 (109.1)
	C	0.294	464.8 (95.2)	124 (272.2)	17.8 (40.1)	266.0 (2860)	+1.5%	-3.4%	11 670 (38 300)	59.0 (114.7)

*DOC based on 1967 ATA domestic formula with 1976 Boeing coefficients

Airframe cost = \$5.2 × 10^6 + \$222/kg (\$100/lb) airframe weight

Engine cost = \$10.3/kN (\$46/lb) SLST

Fuel cost = \$0.082/l (\$0.31/gal)

Fuel density = 0.803 kg/l (6.7 lb/gal)

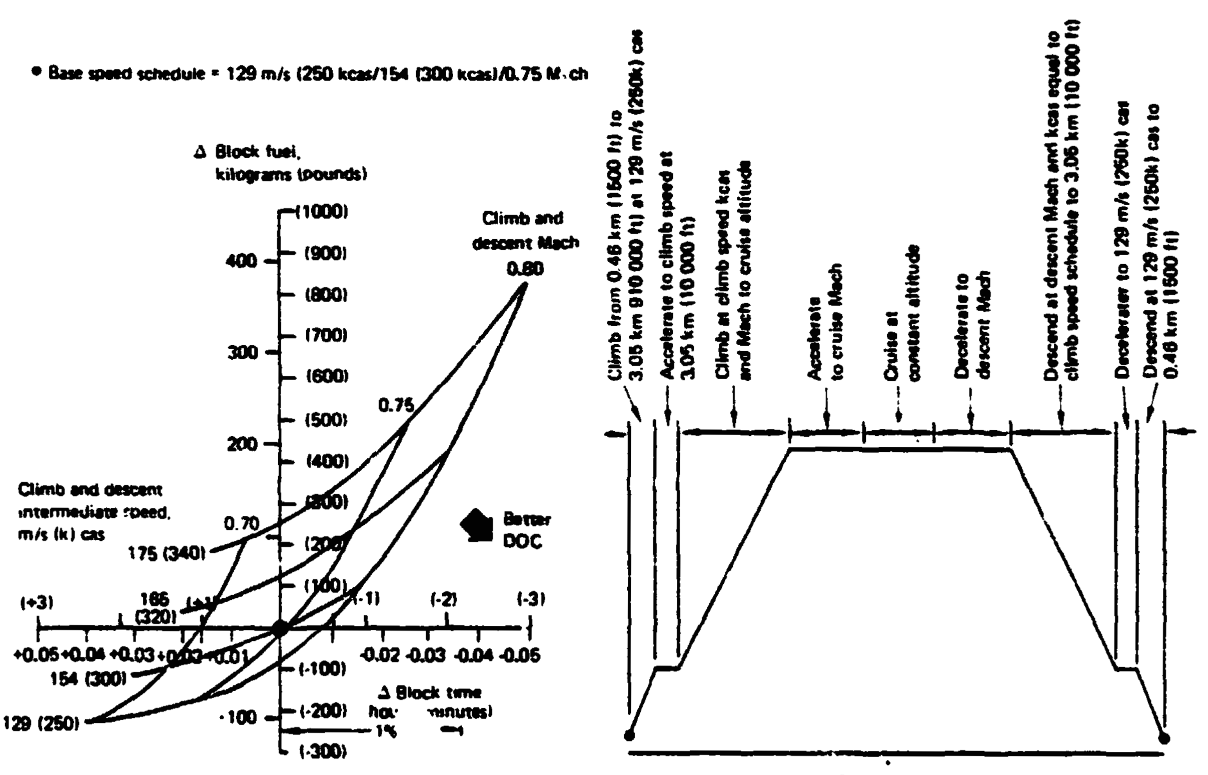

• Base speed schedule = 129 m/s (250 kcas/154 (300 kcas)/0.75 Mach

Δ Block Time Versus Δ Block Fuel for Various Climb and Descent Speed Schedule

Common Climb and Descent Flight Profile

Figure 48. Common Climb and Descent Speed Schedule

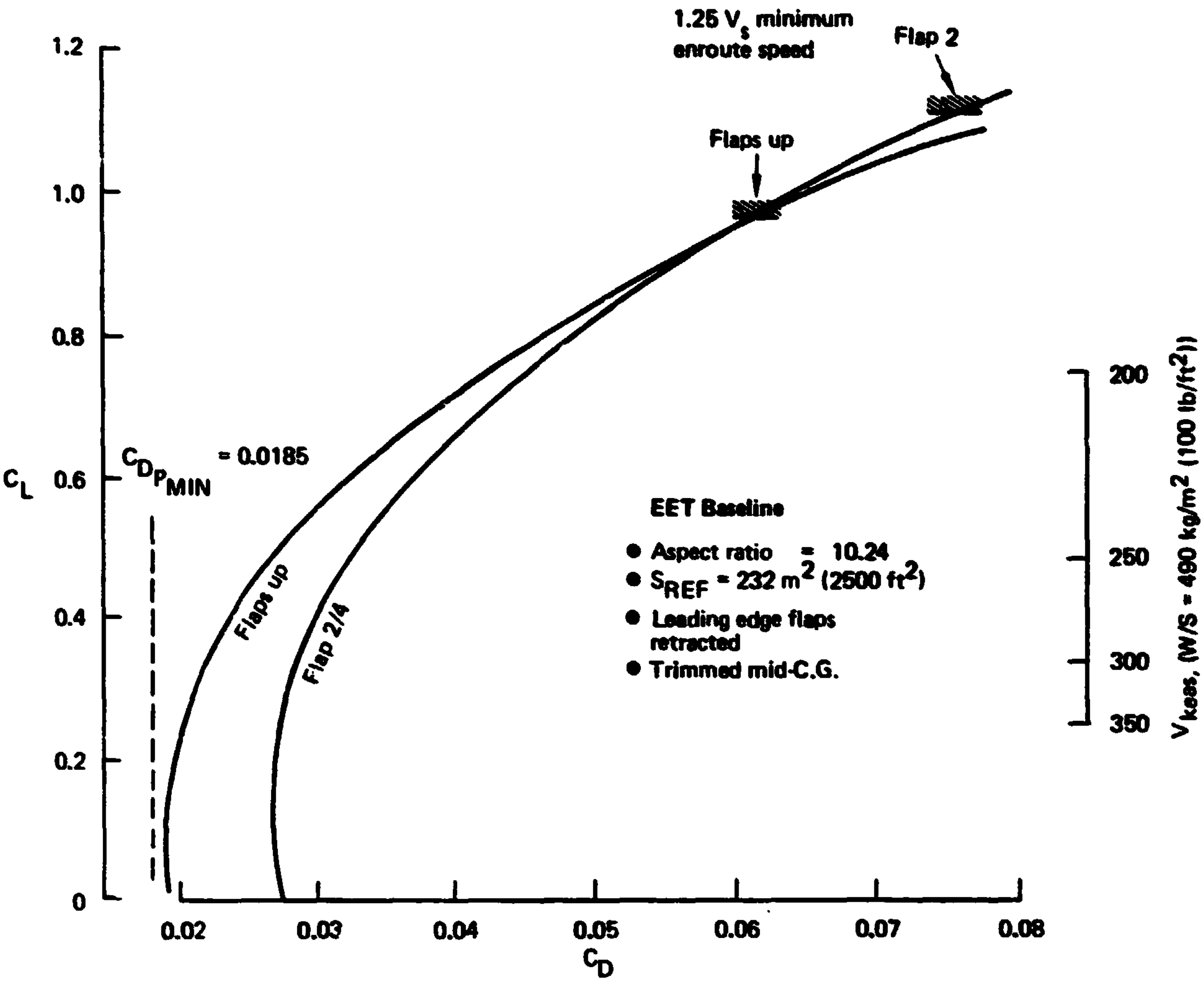

Figure 49. Enroute Drag

4.2.5 Augmented Stability Studies

The EET reference baseline airplane (768-785B) was analyzed with low-speed aerodynamic characteristics based upon a center-of-gravity position of 8% mean aerodynamic chord (MAC) at takeoff without stability augmentation systems (SAS). Low-speed performance effects resulting from more aft center-of-gravity locations are shown in figure 50. Lift-to-drag ratio envelopes were developed with center-of-gravity positions at 28% MAC and 48% MAC to search for the limits of aft center-of-gravity benefits to low-speed performance.

Subsequent to this study, estimated extensions of aft center-of-gravity limits and criteria were provided for handling qualities (HQ) and hard (H) SAS. The aft center-of-gravity movements permitted by HQSAS and HSAS are quite small (2 and 4 to 8%, respectively) compared with the center-of-gravity movements studied. Configuration and weight effects associated with aft center-of-gravity positions at high gross weights were not

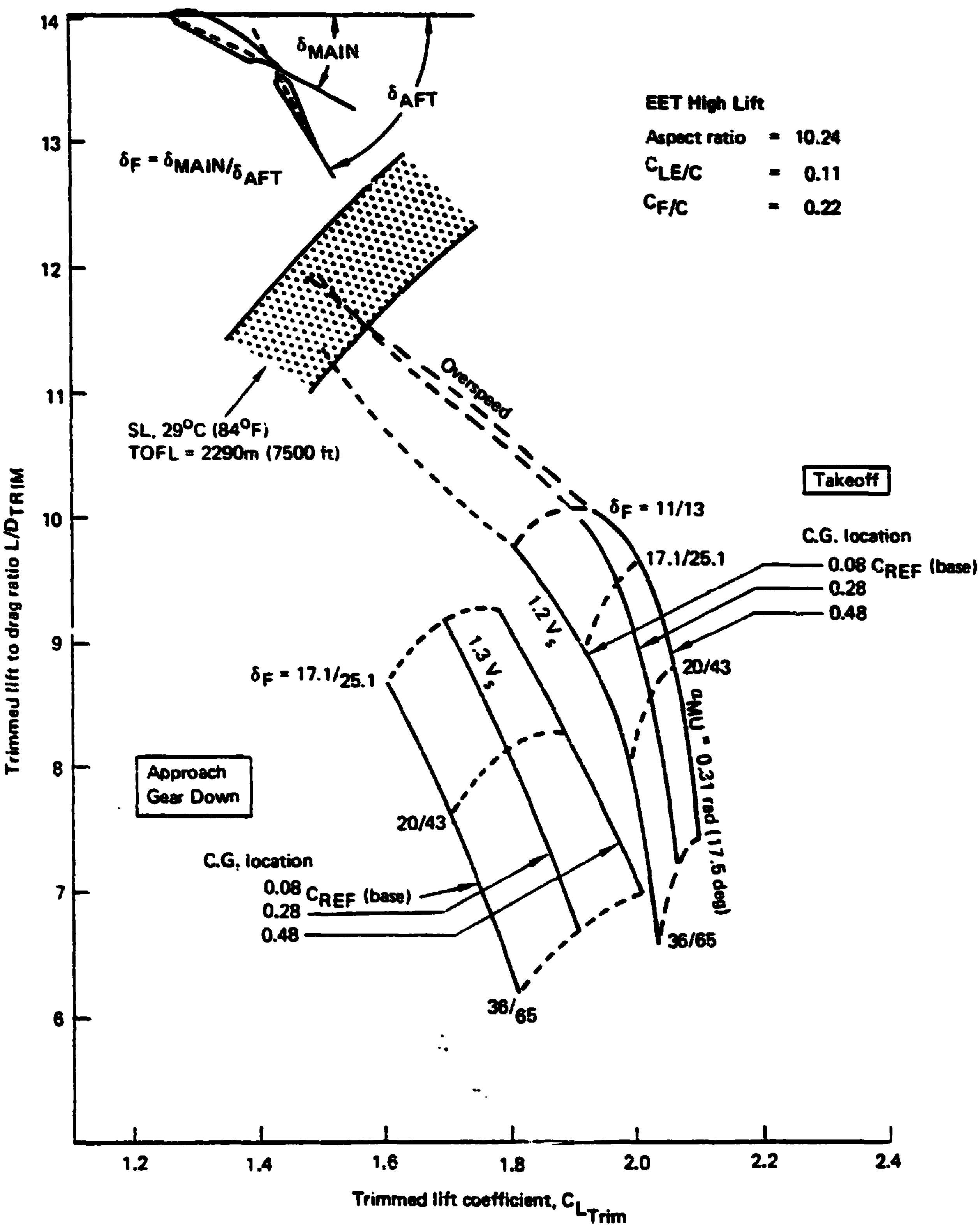

Figure 50. Effect of Trim C.G. Location

included in this study. Performance results are shown in the form of relative takeoff and landing performance on the reference baseline design selection chart (fig. 51). Benefits of the further aft center-of-gravity limits were shown to be better takeoff field length and landing approach speeds, but the effects on fuel efficiency were quite small. No cruise benefit for aft center of gravity was included in this study. Reduced trim drag and associated configuration changes would show larger fuel savings than those shown here, which reflect only low-speed performance effects.

The study of aft center-of-gravity positions was done to measure the low-speed performance benefits of reduced trim drag due to reduced horizontal tail downloads. Continued improvement in maximum lift coefficient was evident as the center-of-gravity moved rearward, but the improvement in the takeoff lift-to-drag envelope was not significant for center-of-gravity locations aft of 28% MAC. As center-of-gravity shifted rearward, the horizontal-tail load required to trim changed direction from downward to upward; further rearward movement produced increasing lift on the horizontal tail, which contributed more induced drag. As the center-of-gravity moves aft, the desired landing

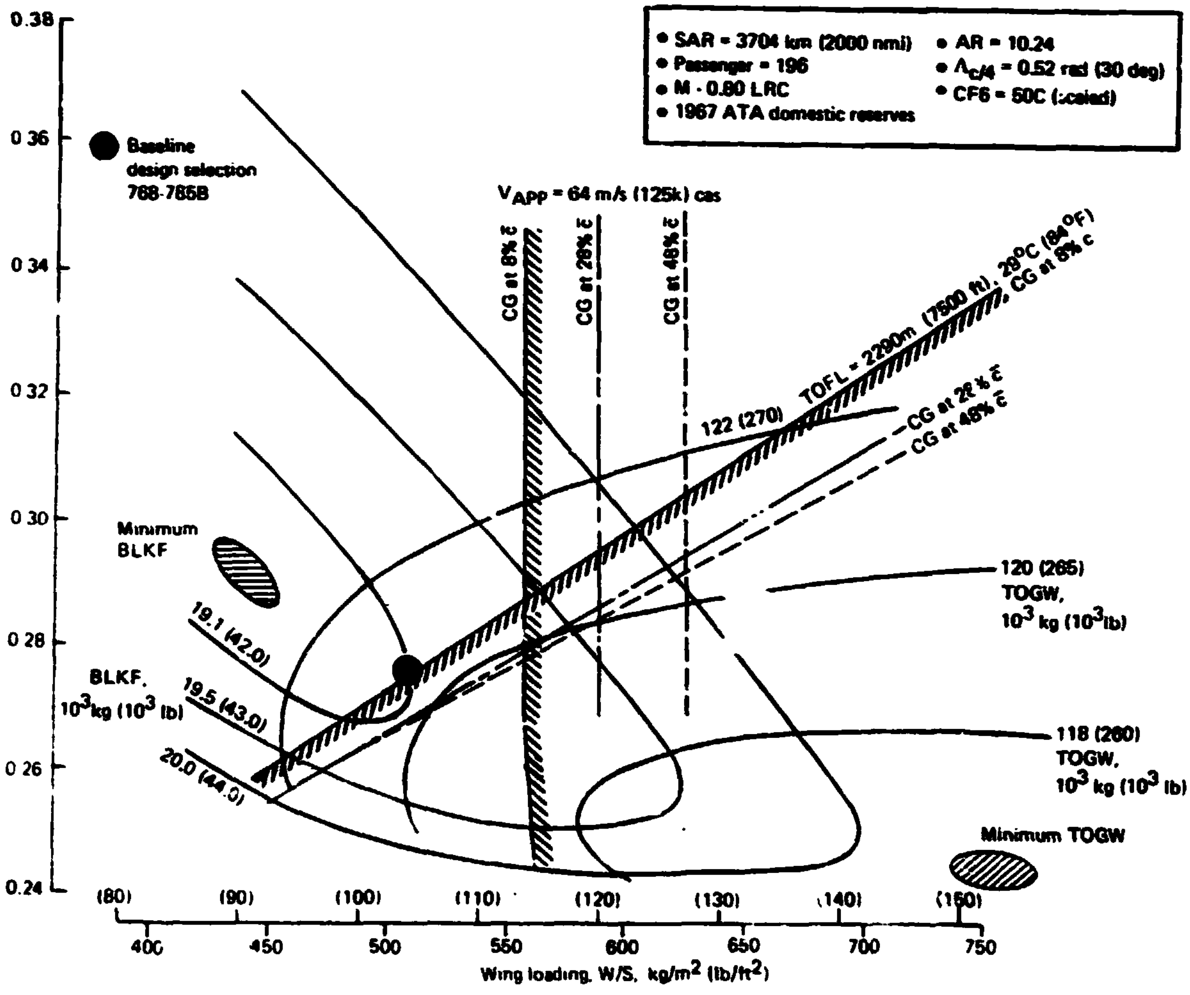

Figure 51. Effects of Aft CG Position on Low-Speed Sizing Constraints

approach speed, 64 m/s (125 keas) can be attained with higher wing loadings. However, this trend cannot be used in selecting a point design without increasing block fuel. Figure 51 shows that the baseline airplane is sized by the TOFL requirement at a point between minimum TOGW and minimum block fuel and is not sized by the approach speed limit. In fact, sizing for minimum block fuel only (disregarding DOC) would have eliminated the 2290-m (7,500-ft) TOFL constraint as well. The results shown in figure 50 indicate that there is little benefit to takeoff performance from moving the takeoff center-of-gravity at 28% MAC (i.e., no further improvement in L/D). If a point design selection were made with takeoff center-of-gravity at 28% MAC, the characteristics and performance changes, relative to the baseline, would be:

-0.4% in takeoff gross weight
-0.6% in operating empty weight
+0.1% in block fuel
-0.3% in direct operating cost

The effect of reduced horizontal-tail size is not included. When maintaining the same airplane loading flexibility (center-of-gravity travel), only a 2% shift aft in forward center-of-gravity limit and a 3% smaller horizontal-tail were identified with the use of HQSAS. Using HSAS, a 4 to 8% shift aft was suggested as "reasonable," with a 6 to 12% smaller horizontal-tail size. However, this would have to be verified by a dynamic analysis on this particular configuration. The reduced horizontal-tail area, while slighlty benefiting takeoff gross weight, operating empty weight, and block fuel, would have a negligible effect on the takeoff and landing field lengths and speeds. The low-speed lift-to-drag ratio benefits of either HQSAS or HSAS would be smaller than the values shown above for a 28% MAC center-of-gravity position, but fuel and weight savings should be positive.

These results are mission and configuration sensitive, and some other mission-airplane combination might show more benefits for aft center-of-gravity SAS. If the airplane were sized for high-altitude airports (i.e., Denver, Colorado, where takeoff L/D is critical), it might profit more in terms of improved payload or range. Benefits might be more significant for this baseline if the takeoff design lift coefficient also were much higher (i.e., as for a trijet version) and if minimum takeoff gross weight were a more critical design selection factor.

Stability augmentation systems that would permit the center-of-gravity to be moved aft by 2% MAC (HQSAS) or 4 to 8% MAC (HSAS) would not cause a large improvement in fuel usage or gross weight for a medium-range twin-engined transport that is already sized essentially for minimum block fuel. Reductions in horizontal-tail size of 3 to 12% will reduce drag and OEW a small amount (this effect is not included in the analyses described above). This analysis addressed only the low-speed matching characteristics with SAS.

4.3 EVALUATION OF IMPACT OF BEST HIGH-LIFT SYSTEM ON EET AIRCRAFT

This subtask evaluated the improvements to the baseline EET configuration obtained by resizing the high-lift sections designed in the design applications studies to obtain the best high-lift system.

The sizing studies, described in sections 4.2.1 and 4.2.3, showed that the baseline EET configuration was sized by sea-level takeoff field length rather than the 64-m/s (125-keas) approach speed requirement and consequently was insensitive to improvements in approach $C_{l_{max}}$. Because of this, the simplified design was chosen for the impact study. However, even though the simplified design provides significantly better aerodynamic performance at sea level in terms of lift-to-drag ratio at takeoff (see fig. 52), only part of the potential DOC benefits from resizing may actually be realized because of the interposition of the enroute engine-out altitude requirement (as shown in the design selection chart, fig. 53). The following table compares the potential and realizable DOC benefits for resizing at sea level using the improved high-lift system:

	Fuel burned, %	DOC, %
Resizing not limited by engine-out altitude	+3/4	-3/4
Resizing limited by engine-out altitude = 3660 m (12,000 ft)	+1/4	-1/4

To show high benefits of advanced design more clearly, an additional study was performed in which the integrated effect of advanced high-lift technology features are presented in

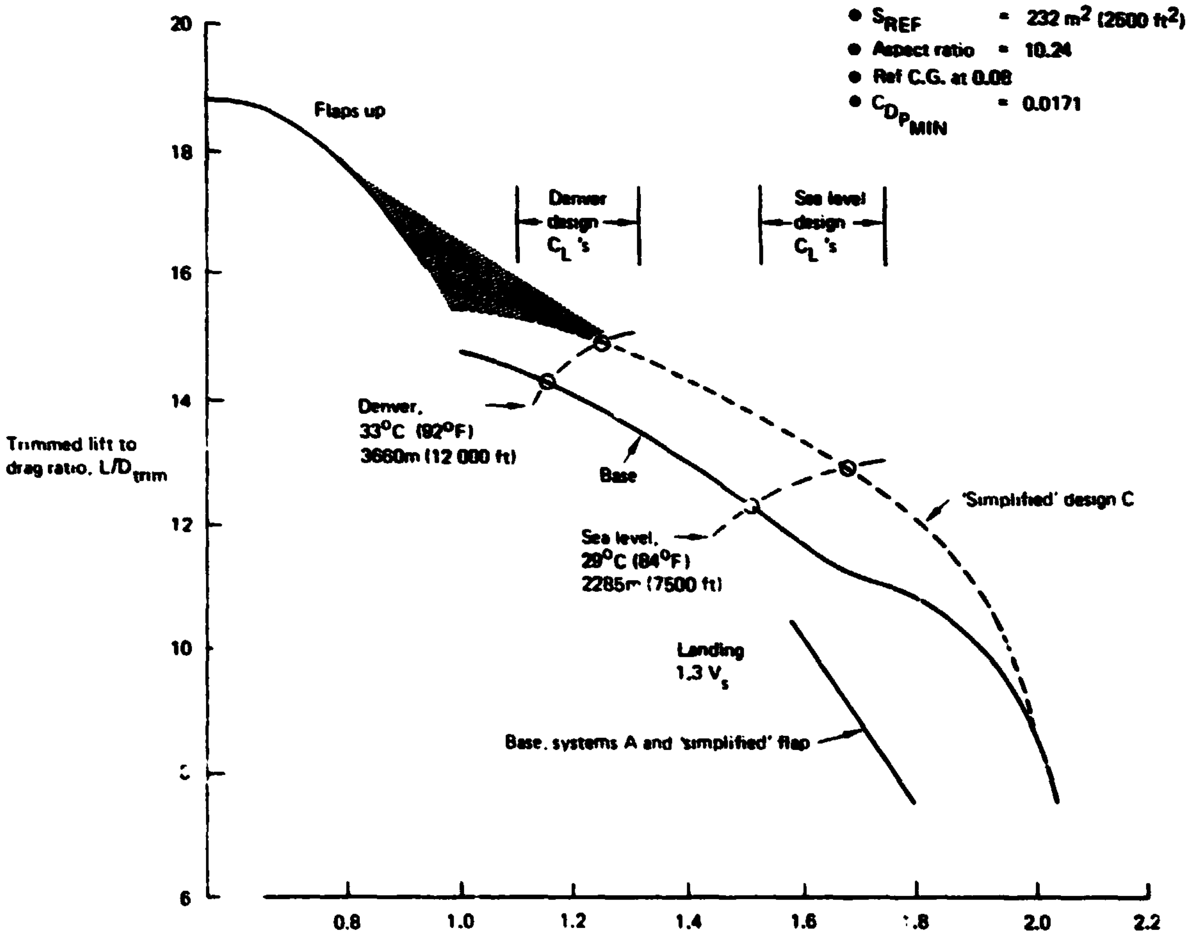

Figure 52. 'Simplified' Flap Envelope

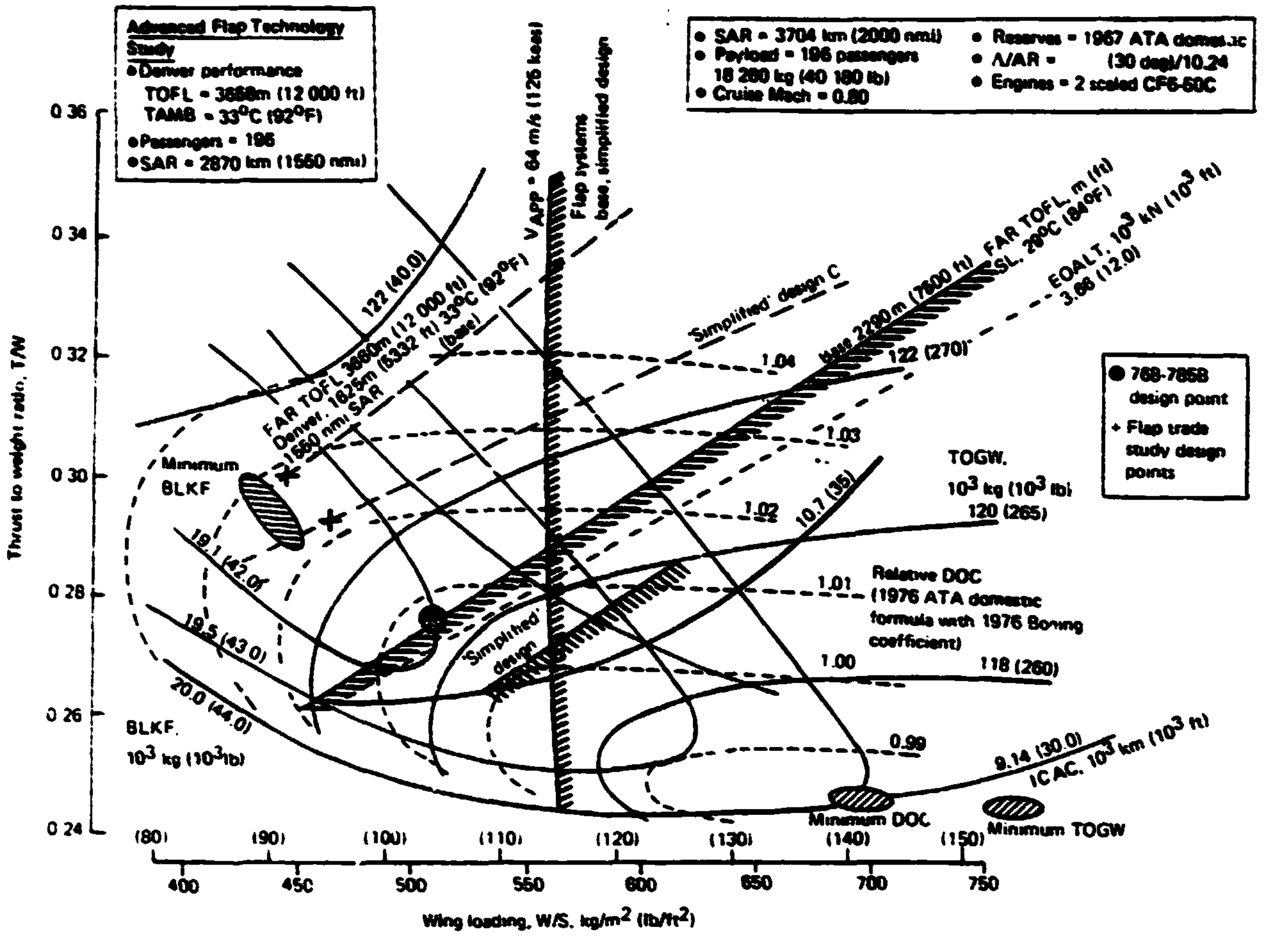

Figure 53. Impact 'Simplified' Design on EET Sizing

terms of increased payload capability when the airplane is limited simultaneously by second-segment climb gradient and takeoff field length, commonly found at hot, high-altitude airports (payload is often restricted for these operations). This section shows the potential performance benefits for the high-lift technology improvements when applied to a twin-engined, domestic, 196-passenger airplane (see fig. 54).

Flap Size

Leading- and trailing-edge flap chord sizing trades may be used to improve takeoff performance or approach speed capability. On the baseline airplane, a shorter, lighter trailing-edge flap chord could be used, since approach speed was not critical. This resulted in an increased payload of two passengers for a fixed airplane size and takeoff gross weight (fig. 54).

Flap Technology

The takeoff lift-to-drag improvements demonstrated by the simplified high-lift system over the base flap system (shown in fig. 49) offer the largest gains in payload life

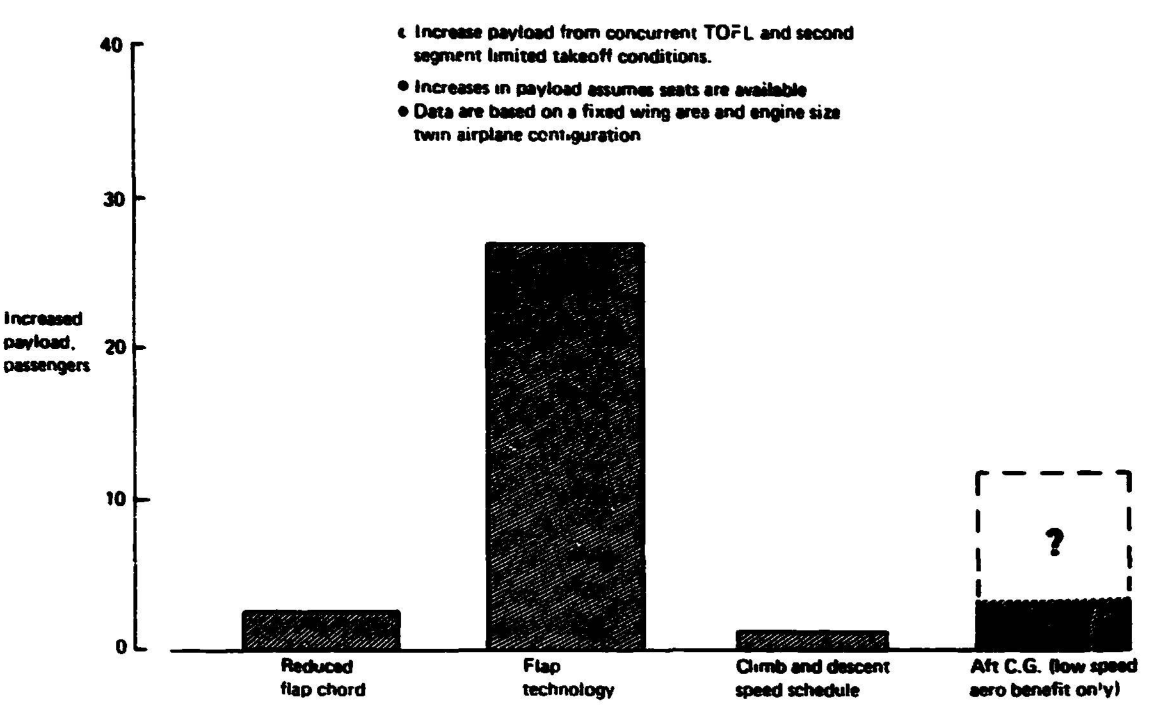

Figure 54. EET High Lift Technology Takeoff Performance Benefits

capability. The 5% increase in lift-to-drag ratio at V_2 at hot, high fields like Denver on a 33°C (92°F) day, allows 26 additional passengers to be carried at a fixed range (fig. 54).

Climb and Descent Speed Schedule

Slower climb and descent speed schedules (shown in fig. 45) tend to increase direct operating cost for a fixed payload. However, when fuel is traded for additional payload, the increased revenue may offset the increased trip cost associated with the longer block time. The potential improvement for payload-limited missions is small, approximately one passenger (fig. 54).

Augmented Stability Study

The effects of further aft center-of-gravity positions possible with different stability augmentation systems have been identified in terms of low-speed lift and drag changes. The low-speed aerodynamic improvements, achievable with a 2 to 6% further aft center-of-gravity position, produce a 2- to 12-passenger increase at a fixed mission range. The total improvements require the complex integration of structures, weights, flight controls, and high- and low-speed aerodynamic characteristics. The total magnitude of the benefit was not shown in this portion of the study.

As shown in figure 54, flap technology improvements (i.e., improved L/D_{V2} at low takeoff C_L) offer the biggest potential for airplane productivity improvements. In general, airplane benefits from advanced high-lift technology are mission and configuration sensitive. However, these study results and trends are applicable only to the baseline study, a 200-passenger, domestic, twin-engined airplane.

5.0 CONCLUSIONS AND RECOMMENDATIONS

5.1 CONCLUSIONS

One of the most important products of the high-lift study was the validation of new analytical techniques for the prediction of multielement airfoil lift curves, including maximum lift coefficient.

- Maximum airfoil section lift coefficient was predicted within 2% of wind tunnel measurements for a four-element, high-lift section that, near maximum lift, showed separation on all four elements. At lower lift levels, the lift loss due to a partially separating aft flap element was predicted very accurately.

- Maximum lift coefficient of this same high-lift section was predicted at flight Reynolds number and, when combined with the previous analysis, these two results show a maximum lift coefficient sensitivity to Reynolds number that was very similar to wind tunnel test data for similar configurations.

These analyses represented a breakthrough in analytic capability. While the analysis programs were developed with Contractor IR&D funds, the validation performed in this contract was invaluable in increasing confidence in these methods and will accelerate their application to both in-house problems and future contract work.

Two high-lift sections were designed to explore the benefits of designing to flight Reynolds number using advanced methodology.

- A four-element high-lift airfoil was designed that, at flight conditions, produced a predicted 13% improvement in $C_{l_{max}}$ and an 11% increase in lift at 4-deg angle of attack, relative to the baseline high-lift system at the same flow conditions.

- A simplified high-lift airfoil with a carefully designed single-slotted flap and slotless leading-edge flap was designed that produced the same $C_{l_{max}}$ and C_l at a given angle of attack as the baseline. In addition to being simpler, this airfoil produced 5.6% improvement in L/D at Denver takeoff lift levels, due primarily to the slotless leading-edge flap.

An important byproduct of these design tasks was the validation of a rational design method for the synthesis of multielement high-lift airfoils. Using analytic techniques, this methodology allows optimization of pressure distributions and airfoil shapes within the aerodynamic and structural constraints and greatly reduces the trial-and-error design process.

While these results were encouraging, the $C_{l_{max}}$ improvements obtained from the first design would not impact the sizing of the study EET configuration because of the low wing loadings required to minimize fuel burned for the design mission. In fact, the baseline high-lift system has excess $C_{l_{max}}$ relative to the 125-keas approach speed requirement used in the sizing studies. The sizing studies show that the study configuration is much more sensitive to takeoff L/D (especially at hot high-altitude airports) than to approach C_L, so that, of the two designs, the simpler, lower drag section design would be best applied to the EET configuration. The simplified-design high-lift

PRECEDING PAGE BLANK NOT FILMED

system considered L/D as a secondary optimization parameter. There is additional potential for L/D improvement if L/D were the primary optimization parameter.

5.2 RECOMMENDATIONS

Since neither design specifically addressed the baseline EET configuration high-lift requirements as determined by the parallel requirements trade studies, it is recommended that follow-on contract design work and testing be done in the following sequence:

- Design a high-lift section for maximum L/D at takeoff lift levels within project-type constraints
- Refine the $C_{l_{max}}$ design to be consistent with the above constraints
- Test both designs in NASA's low-turbulence pressure tunnel at both full-scale and atmospheric wind tunnel Reynolds numbers (17×10^6 and 2×10^6)

6.0 REFERENCES

1. Henderson, M. L.: "A Solution to the 2-D Separated Wake Modeling Problem and Its Use to Predict $C_{L_{max}}$ of Arbitrary Airfoil Sections," AIAA 16th Aerospace Sciences Conference Paper, January 1978.

2. Henderson, M. L.: "Inverse Boundary Layer Technique for Airfoil Design," Advanced Technology Airfoil Research Conference Paper, March 1978.

3. Brune, G. W. and Manke, J. W.: "An Improved Version of the NASA-Lockheed Multielement Airfoil Analysis Computer Program," NASA Contractor Report No. CR 145323, March 1978.

APPENDIX A:
DESCRIPTION OF THE BASELINE HIGH-LIFT SYSTEM GEOMETRY

The figures in this appendix describe the baseline high-lift section in detail.

Figure	Title
A1	Location of the Baseline Airfoil on the Wing Planform
A2	Leading- and Trailing-Edge Flaps
A3	Definition of Baseline Main Airfoil Element
A4	Definition of Main and Aft Flap Elements
A5	Definition of Baseline Leading-Edge Flap

PRECEDING PAGE BLANK NOT FILMED

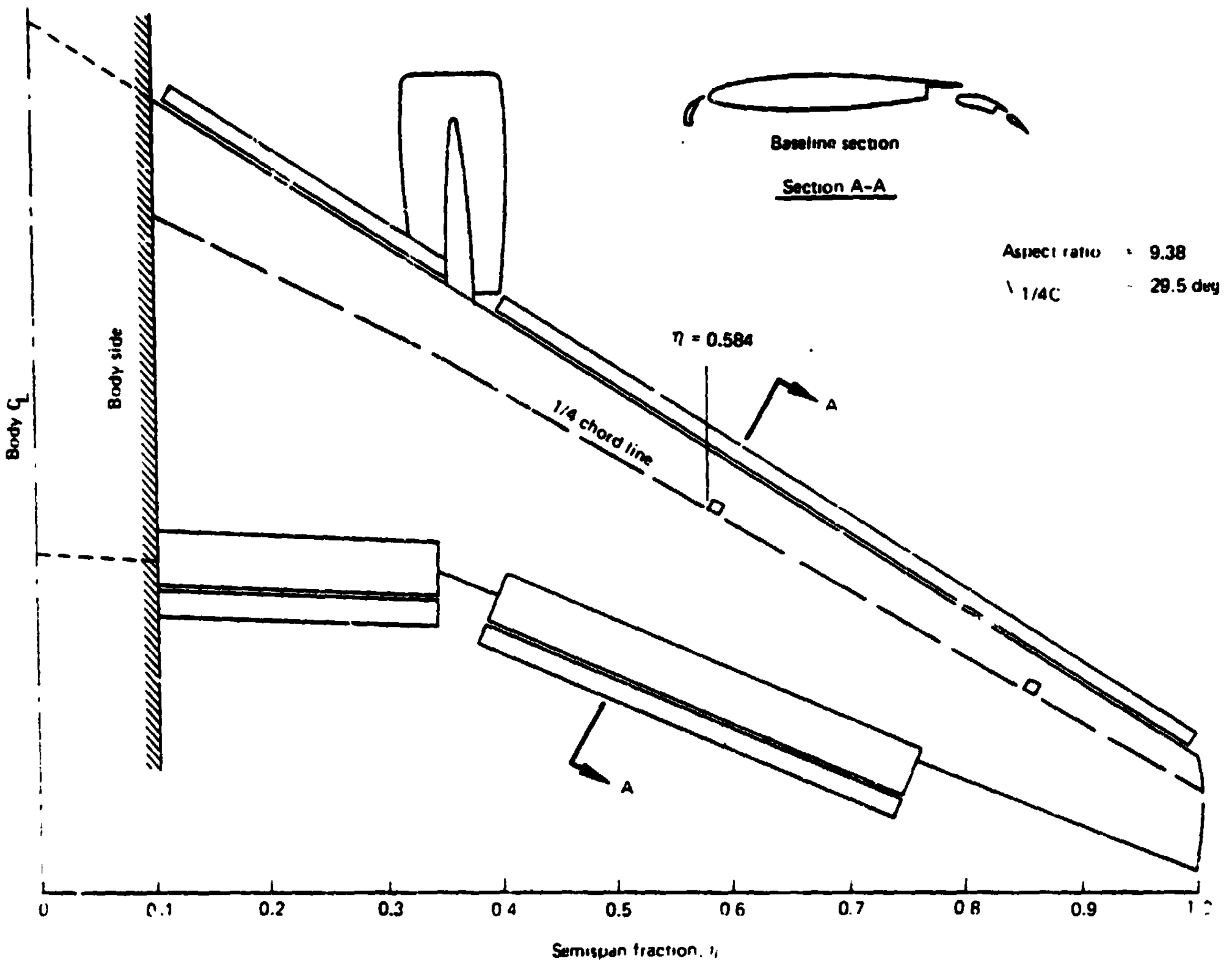
Baseline section
Section A-A
Aspect ratio = 9.38
Λ 1/4C = 29.5 deg
η = 0.584
A
1/4 chord line
Body side
Body ℄
A
0
0.1
0.2
0.3
0.4
0.5
0.6
0.7
0.8
0.9
1.0
Semispan fraction, η

Figure A1. Location of the Baseline Airfoil on the Wind Tunnel Model Wing Planform

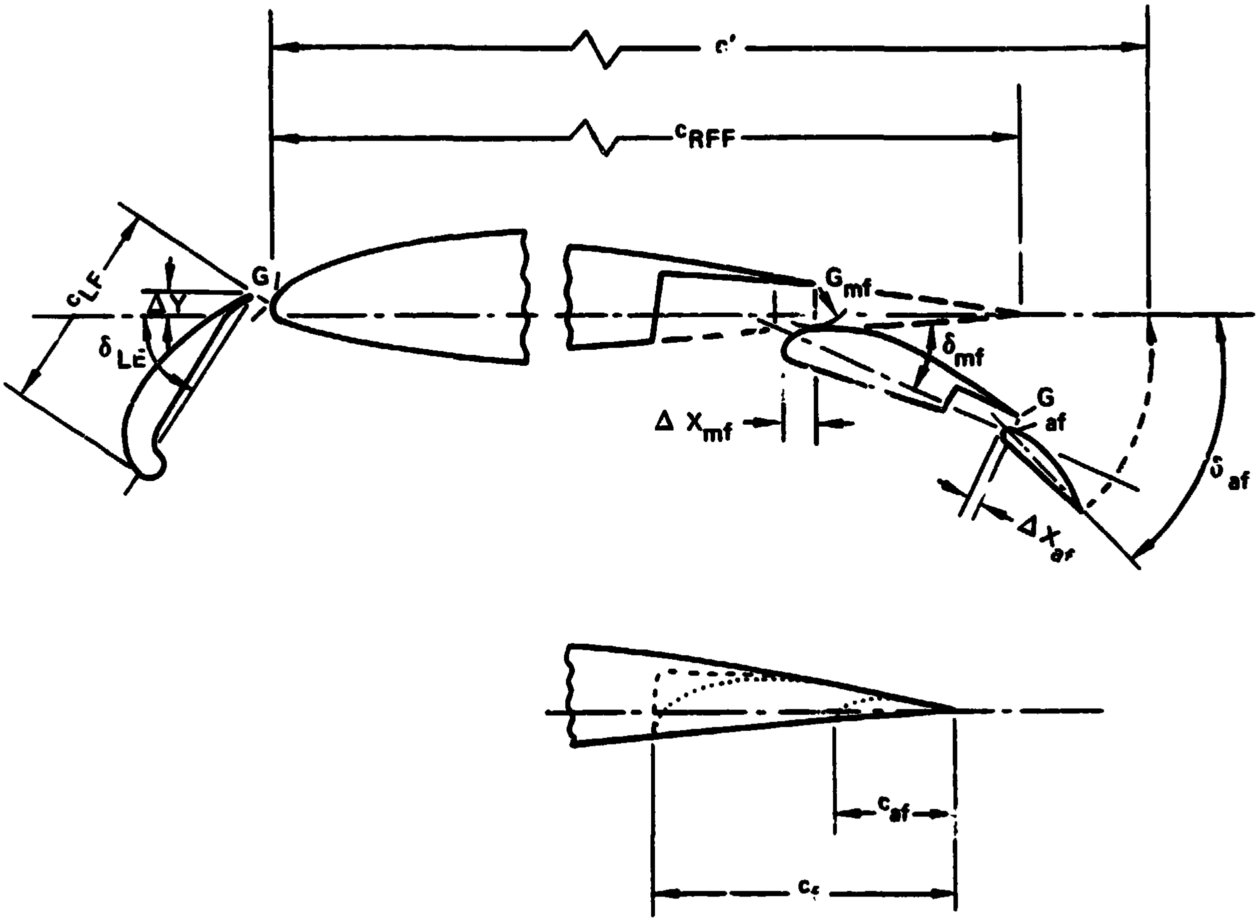
c'
c_RFF
c_LF
ΔY
δ_LE
G
G_mf
δ_mf
Δ X_mf
G_af
Δ X_af
δ_af
c_af
c_f

Figure A2. Leading and Trailing Edge Flaps

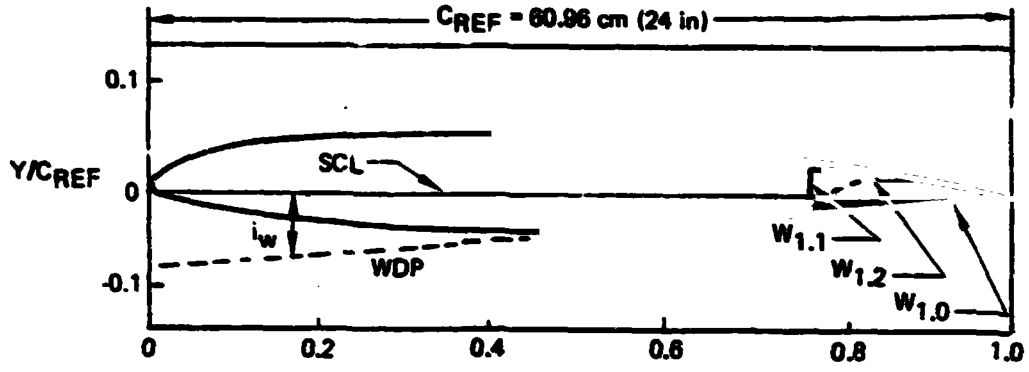

X/C_{REF}	Upper Y/C_{REF}	Lower Y/C_{REF}
0	0	0
0.0006	0.0037	-0.0018
0.0010	0.0050	-0.0027
0.0025	0.0078	-0.0043
0.005	0.0112	-0.0058
0.015	0.0207	-0.0098
0.02	0.024[illegible]	-0.0112
0.025	[illegible]	-0.0125
0.0375	[illegible]	-0.0152
0.05	0.0384	-0.0175
0.075	0.0465	-0.0216
0.10	0.0521	-0.0254
0.125	0.0566	-0.0288
0.15	0.0599	-0.0320
0.20	0.0643	-0.0375
0.25	0.0665	-0.0417
0.30	0.0674	-0.0445
0.35	0.0673	-0.0458
0.40	0.0667	-0.0457
0.45	0.0654	-0.0443
0.50	0.0636	-0.0417
0.55	0.0613	-0.0383
0.60	0.0585	-0.0344
0.65	0.0548	-0.0303
0.70	0.0503	-0.0260
0.75	0.0450	-0.0218
0.80	0.0384	-0.0174
0.85	0.0307	-0.0132
0.90	0.0218	-0.0090
0.95	0.0116	-0.0047
1.00	0.0004	-0.0004

Basic (flaps-up) airfoil, $W_{1.0}$

		$W_{1.1}$ Square cove	$W_{1.2}$ Streamlined cove
X/C_{REF}	Upper Y/C_{REF}	Lower Y/C_{REF}	Lower Y/C_{REF}
0.70	0.0503	-0.0260	-0.0260
0.75	0.0450	-0.0218	-0.0161
0.7638	——	-0.0206	——
0.7664	——	0.0090	——
0.7686	——	0.0337	——
0.775	0.0417	——	-0.0048
0.80	0.0384	0.0309	0.0062
0.825	0.0345	0.0287	0.0154
0.85	0.0307	0.0265	0.0216
0.87	0.0271	0.0248	0.0238
0.8884	0.0240	0.0232	0.0232

TE flaps-down airfoil coves

Note: Cruise performance of this airfoil was not used for the trade studies of section 4.2.

Reference figure : A1

Midspan	Section	i_w
	A-A	0.09 rad (4.95 deg)

Scale factor = C_{REF} (model) / $C_{FULL\ SCALE}$

15%

Figure A3. Definition of Baseline Main Airfoil Element

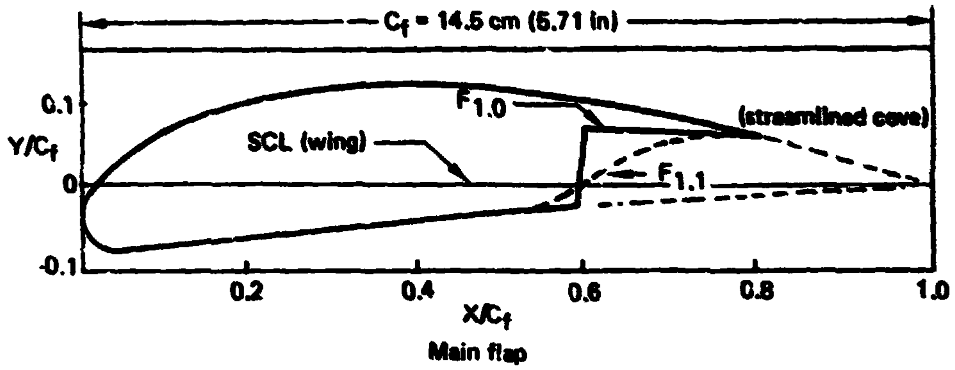
C_f = 14.5 cm (5.71 in)
0.1
Y/C_f
0
-0.1
$F_{1.0}$
(streamlined cove)
SCL (wing)
$F_{1.1}$
0.2
0.4
0.6
0.8
1.0
X/C_f
Main flap

X/C_f	Upper Y/C_f	Lower Y/C_f	Lower Y/C_f Streamlined cove
0	-0.0460	-0.0460	
0.0025	-0.0310	-0.0598	
0.005	-0.0243	-0.0655	
0.0075	-0.0190	-0.0698	
0.0125	-0.0099	-0.0763	
0.025	0.0053	-0.0827	
0.05	0.0274	-0.0826	
0.075	0.0438	-0.0807	
0.10	0.0569	-0.0785	
0.125	0.0678	-0.0764	
0.15	0.0768	-0.0743	
0.175	0.0844	-0.0722	
0.20	0.0906	-0.0700	
0.25	0.1002	-0.0658	
0.30	0.1061	-0.0615	
0.35	0.1093	-0.0572	
0.40	0.1099	-0.0530	
0.45	0.1078	-0.0487	
0.50	0.1030	-0.0444	
0.55	0.0955	-0.0416	-0.0354
0.575	———	———	-0.0234
0.5851	———	-0.0371	———
0.5893	———	0.0111	———
0.5935	———	0.0593	———
0.60	0.0860	0.0587	-0.0088
0.65	0.0758	0.0544	0.0227
0.70	0.0656	0.0499	0.0377
0.75	0.0552	0.0456	0.0446
0.8106	0.0421	0.0403	0.0403

$$\frac{C_f}{C_{REF}} = 23.8\%$$

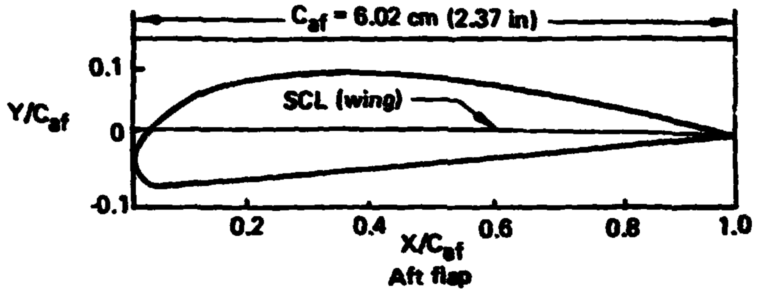
C_{af} = 6.02 cm (2.37 in)
0.1
Y/C_{af}
0
-0.1
SCL (wing)
0.2
0.4
0.6
0.8
1.0
X/C_{af}
Aft flap

X/C_{af}	Upper Y/C_{af}	Lower Y/C_{af}
0	-0.0500	-0.0500
0.005	-0.0223	-0.0700
0.0125	-0.0062	-0.0790
0.0225	0.0060	-0.0817
0.05	0.0340	-0.0798
0.10	0.0646	-0.0755
0.15	0.0843	-0.0712
0.20	0.0969	-0.0670
0.30	0.1104	-0.0584
0.40	0.1107	-0.0499
0.50	0.1033	-0.0414
0.60	0.0911	-0.0328
0.70	0.0727	-0.0243
0.80	0.0500	-0.0158
0.90	0.0272	-0.0072
0.95	0.0157	-0.0030
1.00	0.0042	0.0013

$$\frac{C_{af}}{C_f} = 41.5\%$$

Flaps	C'/C_{REF}	δ_{mf}	G_{mf}/C_{REF}	$\Delta X_{mf}/C_{REF}$	δ_{af}	G_{af}/C_{REF}	$\Delta X_{af}/C_{REF}$
20/43	1.150	0.4 rad (22.7 deg)	3.2%	3.0%	0.82 rad (47.0 deg)	1.0%	1.6%

Figure A4. Definition of Main and Aft Flap Elements

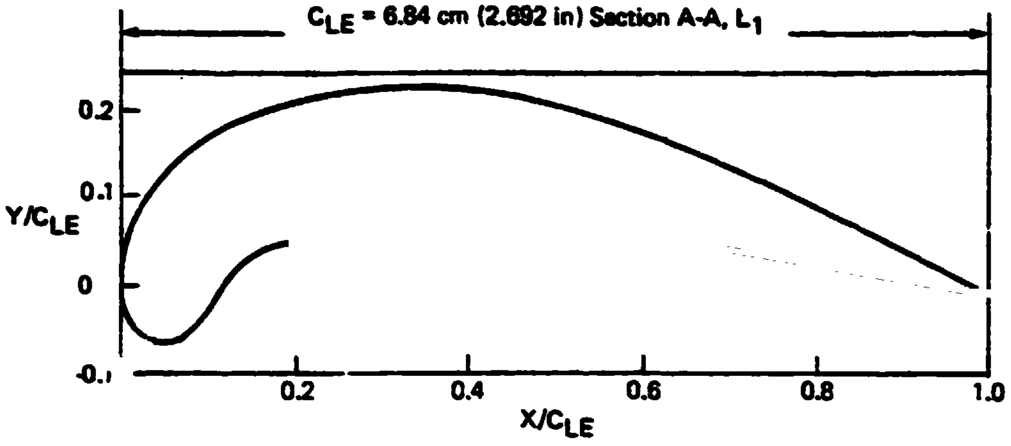

X/C_{LE}	Upper Y/C_{LE}	Lower Y/C_{LE}
0	0	0
0.0007	0.0154	-0.0102
0.0050	0.0441	-0.0361
0.01	0.0594	
0.02	0.0839	-0.0561
0.0325	0.1062	-0.0652
0.05	0.1286	-0.0690
0.078		-0.0585
0.10	0.1703	-0.0308
0.1245		0.0085
0.15	0.1953	0.0347
0.20	0.2115	0.0509
0.25	0.2226	↑
0.30	0.2293	
0.35	0.2318	
0.40	0.2298	
0.45	0.2235	
0.50	0.2136	
0.55	0.1998	
0.60	0.1825	↓
0.65	0.1625	0.0509
0.70	0.1410	0.0479
0.75	0.1178	0.0411
0.80	0.0960	0.0321
0.85	0.0730	0.0231
0.90	0.0494	0.0142
0.95	0.0253	0.0052
1.00	0	-0.0037

L_1 variable position		Baseline position
δ_{LE}	= 0.87 rad (49.8 deg) to 1.13 rad (64.8 deg)	1.01 rad (57.8 deg)
G/C_{REF}	= 1.00% to 2.50%	1.44%
$\Delta Y/C_{REF}$	= 0.50% to 1.50%	1.00%

Figure A-5. Definition of Baseline Leading Edge Flap

APPENDIX B:
CALCULATION OF LIFT AND PITCHING MOMENT WHEN SEPARATION IS PRESENT

A465 Program Description, Analysis Mode

The A465 computer program is an advanced panel method capable of solving general boundary value problems in incompressible, inviscid, two-dimensional flow. In its analysis mode, this program is used to solve the following inviscid problems:

a. Simple potential flow about arbitrary airfoil systems

b. The separated wake displacement surface boundary value problem on arbitrary airfoil systems. (The boundary conditions and theory are discussed in detail in reference B1.)

The purpose of this solution is to find the shape of the separated wake displacement surface that conforms to the outer velocity boundary conditions that must exist on a seperated wake, both in the presence of the airfoil and trailing the airfoil system. Having a separated wake displacement surface of the proper shape and in the proper position relative to other elements, the inviscid effect of the wake displacement on the airfoil pressure distributions may be determined by simply computing potential flow about airfoil surfaces plus their separated wake displacement surfaces.

VISC Program Description

The VISC program is capable of computing the properties of laminar and turbulent boundary layers, the position and effect of transition, and laminar and turbulent separations. Theoretical components of this program are summarized as follows:

Component	Theory
Laminar boundary layer	Poulhausen
Laminar separation	Poulhausen-Henderson
Laminar bubble	Henderson (empirical)
Transition	Granville
Turbulent boundary layer	Momentum integral, power law velocity profile, Garner's equation for form parameter, Ludwig-Tillman equation for shear-stress at wall (ref. B1)
Turbulent separation	$H > 3.0$

The VISC program provides the viscous half of the computations and is designed to couple with the A465 program to provide boundary layer displacement thickness and separation points for the inviscid solution.

VISC-A465 Coupling Technique

The method for coupling these two programs in an iterative loop to produce well-behaved convergence to a solution was a matter of some concern in the early phases of the analysis of the baseline high-lift airfoil.

The simplest method would be to compute the pressure distribution based upon the section geometry alone (e.g., no wake, no boundary layers modeled), compute the boundary layer thickness and separation points from this pressure distribution, and model the separations as discussed previously to determine lift and pitching moment. The problem is that the pressure distribution used to compute the separation points (analysis of the bare geometry) is significantly different from the final pressure distribution (which has separations and boundary layers modeled). A boundary layer analysis of the final pressure distribution will not produce the same boundary layer thickness as the initial pressure distribution, and more importantly, may not produce the same separation point.

Obviously, some technique is needed for repeating the boundary layer analysis and separation modeling sequence that will settle on a stable point. The technique used for single-element airfoil section is:

a. Compute, using A465, the potential flow pressure distribution of the airfoil geometry at the angle of attack of interest.

b. Compute, using VISC, the displacement thickness and separation point based upon the pressure distribution from step a.

c. Displace the airfoil surface by the displacement thickness up to the separation point, and add the starting wake shape aft of the separation point (done automatically in VISC).

d. Employ A465 to define the separated wake shape and to compute a new pressure distribution.

e. Compute the displacement thickness and separation point based upon the revised pressure distribution from step d.

f. Cycle steps c to e until the separation point has converged.

Because of the strong leading-edge, trailing-edge coupling between the elements, a modified technique must be applied when analyzing multielement airfoil systems. The basic problem is that the leading-edge pressure of a trailing element controls, to a large extent, the trailing-edge pressure of the next element forward. The boundary layer of the forward element is very sensitive to the pressure gradient near its trailing edge, so that an error in the trailing-edge pressure caused by an error in the trailing element leading-edge pressure will cause inaccurate prediction of separation on the forward element. If handled incorrectly, errors in separation point position will increase for each succeeding forward element and will cause divergence in the overall solution. For this reason, the single-element technique is applied to the trailing-edge element first; having relaxed the separation point on it, the boundary layer and separation are modeled on the next element, and the wakes and separations on both elements are then relaxed. This process is continued forward until all separations and boundary layers are relaxed simultaneously. In the cases run to date, this procedure has produced well-converged solutions. These techniques tend to produce steady forward movement of the separation point and so are probably overdamped. However, this type of convergence has led to a high success rate in obtaining relaxed solutions, though requiring a longer solution execution time.

Reference

B1. Schlichting, H.: Boundary Layer Theory, McGraw-Hill Book Co., Inc., pp. 238-251, 391-406, 566-579.

APPENDIX C:
INVERSE BOUNDARY LAYER TECHNIQUE FOR PRESSURE DISTRIBUTION SYNTHESIS AND OPTIMIZATION, PROGRAM A427

Definition of Airfoil Pressure Distribution

At low Mach numbers, the performance of an airfoil is either defined by or limited by the boundary layer and the requirement of a reasonable (or buildable) thickness form. To proceed with a rational design process, one must have a boundary layer technique that, given boundary layer parameters, will compute a pressure distribution and, hopefully, is constrained to produce only pressure distributions that are realistic.

With such a computational tool in hand, the designer might take advantage of the airfoil design process shown in figure C1. The most notable aspect of this process is that it proceeds from performance requirements to initial contour entirely in the inverse mode, first to compute a desirable pressure distribution, and then to compute an initial airfoil contour. The last block, the detailed analysis and refinement stage, is the last remnant of trial and error and, for the small changes involved in refinement, this is probably desirable (or at least inevitable).

Inverse Boundary Layer Equations

An inverse boundary layer technique is a solution to the boundary layer equations where boundary layer parameters are specified and a pressure distribution is computed. The boundary layer momentum equation, Garner's equation for form parameter variation, and the Ludwig-Tillman equation for the wall shear stress are used. These equations are arranged to solve for a velocity distribution, given a variation in the form parameter H [= f(s/c)]. The solution technique is shown below.

Solving Garner's equation for the velocity derivative produces

$$\frac{d(u/u_\infty)}{d(s/c)} = -\frac{dH/d(s/c)}{(u/u_\infty)\bullet e^{4.(H-1.4)}} - \frac{0.0315(H-1.4)u/u_\infty}{(R_\theta)^{1/6}\,\theta/c} \tag{1}$$

For the momentum equation, solve for $d(\theta/c)/d(s/c)$

$$\frac{d(\theta/c)}{d(s/c)} = \frac{\tau_0}{\rho u^2} - (H+2)\,\frac{\theta/c}{u/u_\infty}\,\frac{d(u/u_\infty)}{d(s/c)} \tag{2}$$

The wall shear stress coefficient, $\tau_0/\rho u^2$, given by Ludwig-Tillman, is

$$\frac{\tau_0}{\rho u^2} = 0.123\,(R_\theta)^{-0.268} \bullet 10^{-0.678H} \tag{3}$$

DING PAGE BLANK NOT FILMED

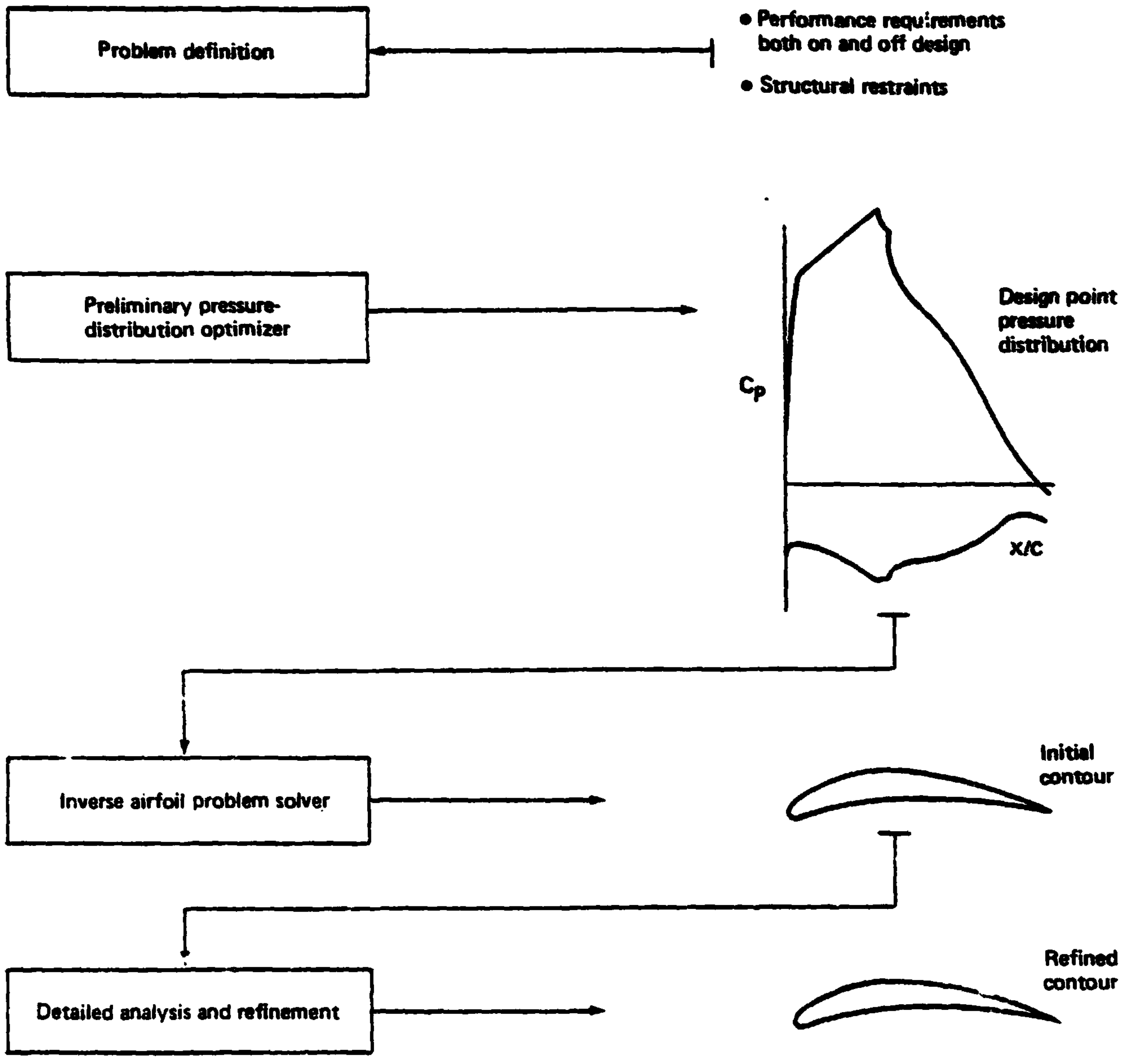
Problem definition
• Performance requirements both on and off design
• Structural restraints
Preliminary pressure-distribution optimizer
C_p
Design point pressure distribution
X/C
Inverse airfoil problem solver
Initial contour
Detailed analysis and refinement
Refined contour

Figure C1. Airfoil Design Process

The momentum thickness ratio, θ/c, and velocity ratio are given by integrating equations (1) and (2) numerically with a known H(x/c) (and thus known dH/dx/c).

$$\theta/c = \frac{d(\theta/c)}{d(s/c)} \bullet \Delta s/c \tag{4}$$

$$u/u_\infty = \frac{d(u/u_\infty)}{d(s/c)} \bullet \Delta s/c \tag{5}$$

$\Delta S/C$ is the integration step in arc length.

Equations (1) through (5) should be relaxed at each step for average values of u/u_∞ and θ/c.

Pressure Distribution Synthesis

With this inverse turbulent boundary layer technique and an appropriate pressure distribution architecture, one may quickly design a pressure distribution on one surface of an airfoil. To explain the way the pressure distribution is synthesized, consider the simpler of the two architectures available, the rooftop (fig. C2). This architecture is characterized by an acceleration region starting at the leading edge and terminating at an input fair point. Constant pressure is assumed from the fair point to the input beginning of turbulent recovery (recovery point). The turbulent recovery spans the remainder of the airfoil and facilitates pressure recovery from the rooftop pressure to the desired trailing-edge pressure. The rooftop pressure is not input, but is found by the inverse boundary layer equations by employing the iterative procedure explained in the following paragraph.

Iterative Procedure for Determining Minimum C_p

Given a fair point, a recovery point, a trailing-edge pressure, and an estimate of rooftop pressure ($C_{p_{min}}$), the pressure distribution is assembled up to the recovery point. This pressure distribution then is analyzed to provide the starting values of H and θ/c for the inverse turbulent boundary layer module. Having these values, the recovery pressure distribution is computed from $C_{p_{min}}$ at the recovery point to the trailing edge, using the desired variation of form parameter in the recovery region. If the computed trailing-edge pressure is not the one desired, $C_{p_{min}}$ is incremented, the pressure distribution up to the recovery point is reassembled, and the process is repeated to convergence.

Lower Surface Pressure Distribution

Since the total pressure distribution must represent a realistic airfoil and the upper surface pressure distribution is defined by boundary layer considerations alone, the lower surface pressure distribution must be defined by the thickness requirements specified by the designer. In the present program, a standard thickness form is used, the NACA OOXX which is scaled to the designer's desired maximum thickness. So with a single input, t/c_{max}, the designer obtains a lower surface pressure distribution, which will result in an airfoil that has the upper surface shape required to produce the designed upper

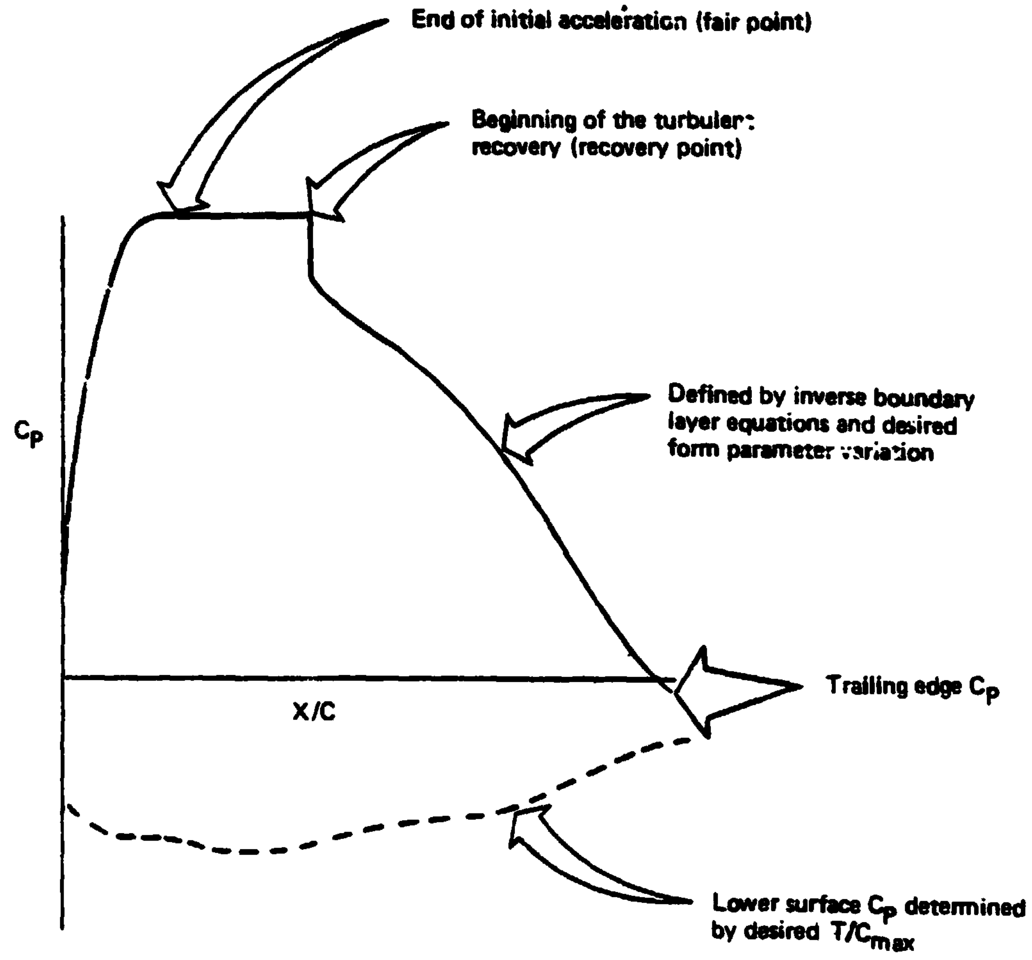
End of initial acceleration (fair point)
Beginning of the turbulent recovery (recovery point)
Defined by inverse boundary layer equations and desired form parameter variation
C_p
X/C
Trailing edge C_p
Lower surface C_p determined by desired T/C_{max}

Figure C2. The Rooftop Pressure Distribution Architecture

surface pressure distribution, and a lower surface contour, which results from a NACA OOXX thickness of the desired maximum thickness-to-chord ratio. Linear airfoil theory is used to accomplish this.

Four-Region Architecture

While the rooftop architecture is effective and simple to use for the preliminary stages of pressure distribution optimization, it allows very little flexibility for controlling the laminar and transitional portion of the boundary layer. As will be shown later, the transition point position is often of first-order importance to the airfoil design problem. To allow for more precise control of the laminar boundary layer, the four-region pressure distribution was devised.

This architecture is shown in figure C3 and is characterized by an acceleration region (I), a region of constant pressure gradient (II), a laminar stressing region (III), and finally the turbulent recovery region (IV). The fair point is input as before and, in addition, the desired value of pressure gradient is given for region II. A desired point of initiation of

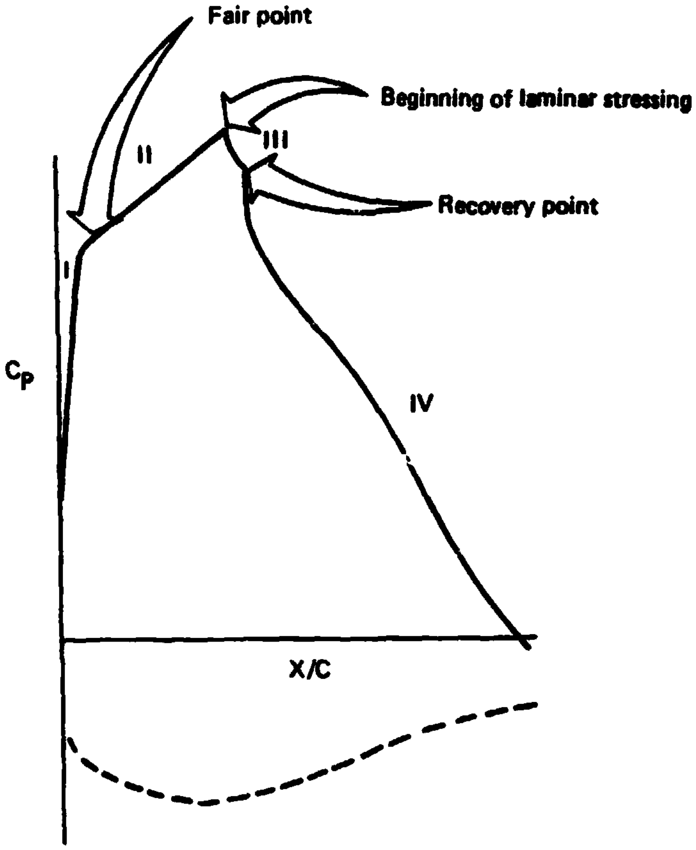

Figure 23. Four-Region Pressure Distribution Architecture

laminar stressing and a desired value of laminar form parameter are given for region III. A simple inverse laminar boundary routine is used to produce the pressure distribution required to produce the desired laminar form parameter. Region III may be used for either stressing the laminar boundary layer to achieve rapid transition without separation, or may be used to avoid transition, depending upon the value of H specified. The equations used in this region are shown below.

$$u/u_\infty = C \bullet (s/c) \, \frac{(1-H/2.55)}{0.94}$$

$$C = \left[(u/u_\infty)_0 (s/c)_0\right] \, \frac{(1-H/2.55)}{0.94} \qquad (6)$$

($)_0$ refers to the values at the begining of region III.

In the derivation of these equations, some liberty was taken in dropping terms for simplicity; however, practice has shown this relationship to be remarkably accurate. The parameter $C_{p_{min}}$ is defined as the pressure at the beginning of region III. Region IV, the turbulent recovery region, is defined by the inverse turbulent boundary layer technique as described earlier.

Optimization Using an Interactive Program

The pressure distribution design technique described has been implemented in an interactive optimization program. That is, the program user operates the computer program in a conversational mode where input is requested by typed messages and given to the program, real time, by responding with typed input at a terminal. Output is printed or plotted immediately at the terminal at the request of the user.

The options available in this optimization program are illustrated in figure C4 and are summarized in the following paragraphs.

The design is initiated by giving the program the flow conditions and details of the architecture chosen. The type of form parameter variation then is chosen (this program allows a constant form parameter or linear, quadratic, or exponential variation to be specified with very little input). An arbitrary H variation may be used if a file of the desired values of H as a function of x/c has been previously generated. With this completed, the program enters the design module and displays C_l, C_d, C_m, and a plot of

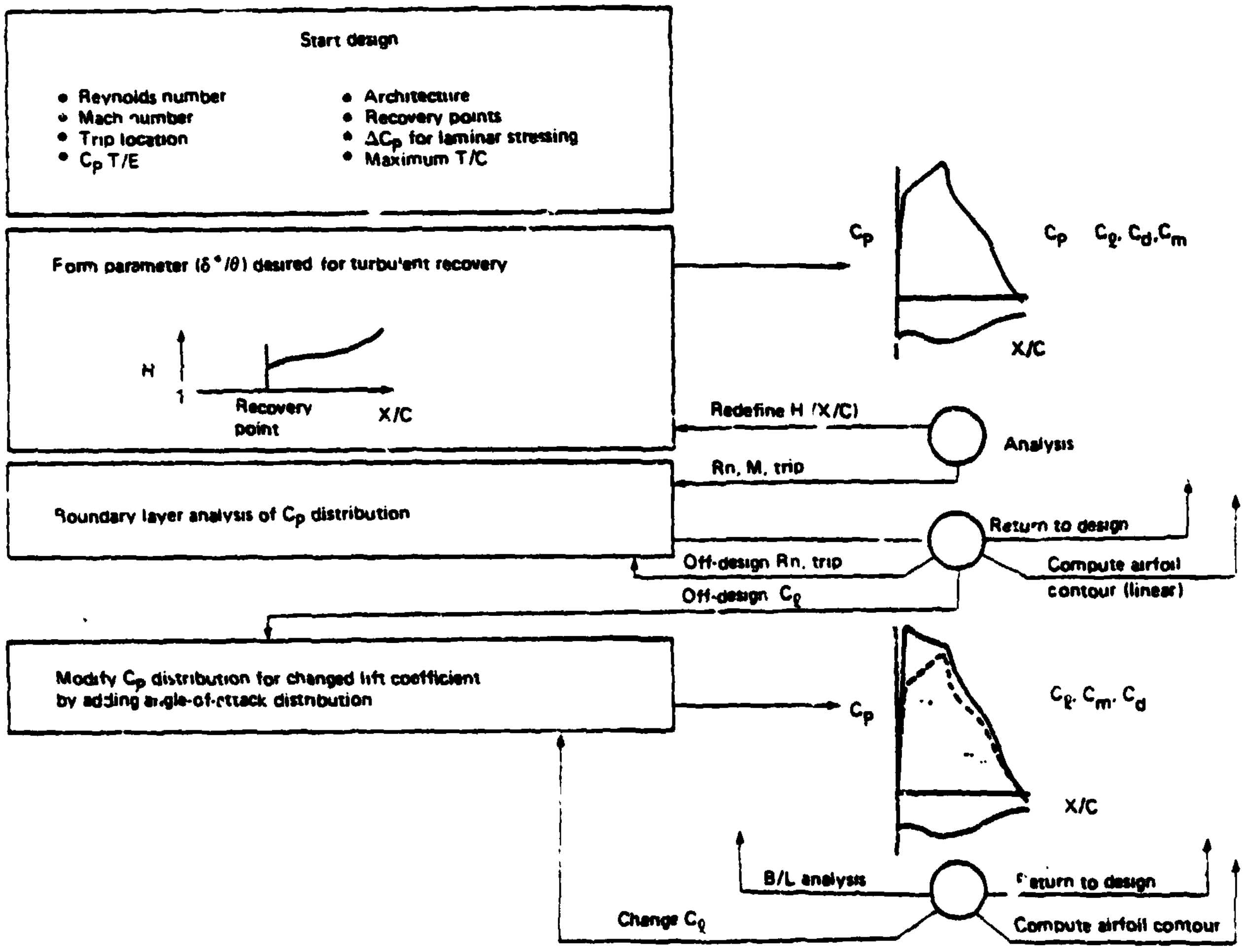
Start design
• Reynolds number
• Mach number
• Trip location
• C_p T/E
• Architecture
• Recovery points
• ΔC_p for laminar stressing
• Maximum T/C
Form parameter (δ^*/θ) desired for turbulent recovery
H
1
Recovery point
X/C
C_p
X/C
C_p C_l, C_d, C_m
Redefine H (X/C)
Analysis
Rn, M, trip
Boundary layer analysis of C_p distribution
Return to design
Off-design Rn, trip
Compute airfoil contour (linear)
Off-design C_l
Modify C_p distribution for changed lift coefficient by adding angle-of-attack distribution
C_p
C_l, C_m, C_d
X/C
B/L analysis
Return to design
Change C_l
Compute airfoil contour

Figure C4. Block Diagram of Interactive Pressure-Distribution Optimizer

the designed pressure distribution. This whole process takes about 30s. At this point, the user may redefine the H variation or any other of the design parameters; if the design point pressure distribution is satisfactory, he may analyze the pressure distribution at an off-design Reynolds number or trip location, or he may analyze the pressure distribution off-design in lift (accomplished by adding an angle-of-attack velocity distribution to the design distribution using linear theory). The results of any of these off-design analyses are printed and plotted immediately at the terminal. In the event a desirable pressure distribution is generated, a preliminary airfoil contour may be requested. This is accomplished by a simple linear inverse program due to Trukenbrodt, and the airfoils produced should be considered as starting points for more accurate design methods. They are, however, excellent benchmarks to check the resulting airfoil's fidelity to structural restraints (such as a restraint on maximum camber or compound surfaces).

To indicate the cost-effectiveness of this approach, consider that to define a pressure distribution, check it at several Reynolds numbers and off-design angles of attack, and produce a preliminary airfoil takes about 7 min on a PDP 11-70 or about 8 min on a CDC Cyber 176. More time is required when the more powerful machine is used because of its lower data transmission rate; the rates currently available are 300 baud on the 176 and 9600 baud on the 11-70.

APPENDIX D: DEFINITION OF AIRFOIL GEOMETRY

Ordinates describing the leading-edge flap, main flap, and aft flap derived from the design of subtask 4.3.1.2.d (discussed in sec. 4.1.c) are provided in table D1. This high-lift airfoil section has been designed to produce maximum lift at a Reynolds number typical of flight conditions (17×10^6).

Ordinates describing the leading-edge flap and trailing-edge flap derived from the simplified design of subtask 4.3.1.2.e (discussed in sec. 4.1.d) are provided in table D2. This high-lift airfoil section has been designed to produce the same maximum lift coefficient as the baseline airfoil section at flight Reynolds number, but with improved lift-to-drag performance and with three elements, rather than with the four-element baseline.

The cruise wing section for both designs was identical with the baseline and is defined in figure A3.

All flaps have been defined in their deflected positions.

PRECEDING PAGE BLANK NOT FILMED

Table D1. $C_{\ell_{max}}$ Design Ordinates

Leading edge flap		Main flap		Aft flap	
X/C	Y/C	X/C	Y/C	X/C	Y/C
-0.01150	0.01014	1.04473	-0.09822	1.08186	-0.19476
-0.01516	0.00497	1.03135	-0.09027	1.08064	-0.18968
-0.01832	-0.00005	1.02006	-0.08640	1.07928	-0.18467
-0.02126	-0.00510	1.00802	-0.08433	1.07656	-0.17467
-0.02413	-0.01011	0.99932	-0.08507	1.07383	-0.16466
-0.02688	-0.01498	0.99238	-0.08568	1.07070	-0.15491
-0.02973	-0.02026	0.98727	-0.08580	1.06880	-0.15025
-0.03515	-0.03082	0.98164	-0.08565	1.06702	-0.14553
-0.03954	-0.04049	0.97021	-0.08210	1.06473	-0.14027
-0.04425	-0.05279	0.95924	-0.07749	1.06249	-0.13602
-0.04734	-0.06532	0.93728	-0.06826	1.05987	-0.13144
-0.04478	-0.07592	0.91533	-0.05902	1.05726	-0.12693
-0.04078	-0.08337	0.89886	-0.05209	1.05428	-0.12200
-0.03955	-0.08768	0.88239	-0.04517	1.05210	-0.11769
-0.04121	-0.09389	0.87141	-0.04056	1.04895	-0.11327
-0.04483	-0.09742	0.86506	-0.03723	1.04464	-0.10962
-0.04901	-0.09699	0.8625	-0.0355	1.04210	-0.10796
-0.05115	-0.09689	0.8592	-0.0325	1.03933	-0.10664
-0.05283	-0.09662	0.8559	-0.0275	1.03652	-0.10594
-0.05535	-0.09574	0.855	-0.0235	1.03429	-0.10596
-0.05764	-0.09437	0.855	-0.02	1.03215	-0.10661
-0.05850	-0.09380	0.8555	-0.0165	1.03042	-0.10831
-0.05974	-0.09288	0.857	-0.0125	1.02960	-0.10981
-0.06189	-0.09088	0.86024	-0.00885	1.02900	-0.11140
-0.06297	-0.08965	0.86796	-0.00232	1.02899	-0.11260
-0.06456	-0.08747	0.87647	-0.00059	1.02927	-0.11379
-0.06590	-0.08521	0.88441	-0.00105	1.03076	-0.11609
-0.06720	-0.08257	0.89181	-0.00279	1.03343	-0.12023
-0.06922	-0.07608	0.89887	-0.00477	1.03879	-0.12852
-0.06990	-0.07011	0.90566	-0.00711	1.04417	-0.13682
-0.06975	-0.06442	0.91225	-0.00958	1.04952	-0.14510
-0.06899	-0.05885	0.92489	-0.01506	1.06025	-0.16168
-0.06776	-0.05339	0.93699	-0.02107	1.06564	-0.16998
-0.06605	-0.04806	0.94874	-0.02741	1.07100	-0.17826
-0.06393	-0.04283	0.96019	-0.03408	1.07637	-0.18655
-0.06136	-0.03769	0.97139	-0.04109	1.07906	-0.19071
-0.05839	-0.03268	0.98230	-0.04851		
-0.05485	-0.02783	0.99286	-0.05643		
-0.05074	-0.02326	1.00358	-0.06410		
-0.04625	-0.01882	1.01321	-0.07195		
-0.04153	-0.01451	1.02283	-0.07980		
-0.03666	-0.01030	1.03244	-0.08769		
-0.03168	-0.00617	1.04473	-0.09822		
-0.02666	-0.00207				
-0.02167	0.00202				
-0.01603	0.00631				
-0.01150	0.01014				

C-2

ORIGINAL PAGE IS
OF POOR QUALITY

Table D2. Simplified Design Ordinates

Simplified leading edge flap	
X/C	Y/C
0.01047	0.01851
0.00677	0.01554
0.00253	0.01189
-0.00169	0.00784
-0.00568	0.00350
-0.00921	-0.00087
-0.01266	-0.00584
-0.01590	-0.01141
-0.01836	-0.01654
-0.02044	-0.02185
-0.02211	-0.02733
-0.02340	-0.03324
-0.02411	-0.03916
-0.02407	-0.04603
-0.02380	-0.04923
-0.02339	-0.05198
-0.02263	-0.05524
-0.02184	-0.05776
-0.02069	-0.06052
-0.01874	-0.06399
-0.01684	-0.06652
-0.01440	-0.06891
-0.01152	-0.07087
-0.00843	-0.07219
-0.00495	-0.07291
-0.00134	-0.07315
0.00379	-0.07200
0.00939	-0.06743
0.00940	-0.06480
0.00950	-0.06230
0.00860	-0.06000
0.00750	-0.05900
0.00500	-0.05780
0.00250	-0.05740
0.00000	-0.05700
-0.00370	-0.05620
-0.00920	-0.05540
-0.00840	-0.04660
-0.00710	-0.03500
-0.00610	-0.02410
-0.00500	-0.01320
-0.00380	0.00000
0.00000	0.00570
0.00350	0.01000
0.00730	0.01480
0.01090	0.01800

Simplified trailing edge flap, δ_{tab} = 0.54 rad (31 deg)			
X/C	Y/C	X/C	Y/C
1.04894	-0.14575	0.88084	0.00368
1.04752	-0.14374	0.88402	0.00396
1.04476	-0.14019	0.88774	0.00400
1.04214	-0.13651	0.89251	0.00353
1.03943	-0.13281	0.89611	0.00283
1.03378	-0.12685	0.89895	0.00181
1.02619	-0.11826	0.90382	0.00048
1.01811	-0.10853	0.90761	-0.00109
1.01162	-0.09970	0.91311	-0.00375
1.00364	-0.08988	0.91838	-0.00665
0.98773	-0.08431	0.92361	-0.00972
0.97732	-0.08048	0.93382	-0.01607
0.96766	-0.07719	0.94343	-0.02231
0.95262	-0.07207	0.95363	-0.02903
0.93833	-0.06707	0.96282	-0.03514
0.92281	-0.06178	0.97242	-0.04161
0.90920	-0.05687	0.98179	-0.04811
0.89411	-0.05173	0.99099	-0.05474
0.87954	-0.04699	0.99738	-0.05943
0.87178	-0.04445	1.00169	-0.06255
0.86663	-0.04275	1.00560	-0.06521
0.86217	-0.04079	1.00778	-0.06674
0.85942	-0.03822	1.01036	-0.06840
0.85599	-0.03538	1.01309	-0.07018
0.85442	-0.03182	1.01579	-0.07212
0.85389	-0.02730	1.01846	-0.07455
0.85424	-0.02376	1.02073	-0.07743
0.85546	-0.01931	1.02231	-0.08024
0.85728	-0.01524	1.02389	-0.08330
0.85907	-0.01222	1.02546	-0.08690
0.86106	-0.00946	1.02730	-0.09203
0.86297	-0.00721	1.03221	-0.10388
0.86437	-0.00573	1.03644	-0.11380
0.86578	-0.00438	1.04064	-0.12428
0.86788	-0.00256	1.04347	-0.13087
0.87007	-0.00092	1.04534	-0.13565
0.87242	0.00057	1.04705	-0.13946
0.87501	0.00186	1.04848	-0.14256
0.87758	0.00281	1.04960	-0.14551